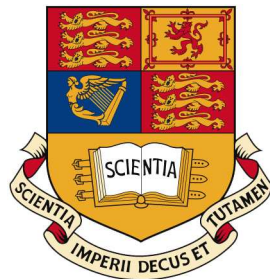# Constraining the supersymmetric parameter space with early data from the Compact Muon Solenoid experiment

Tom Whyntie

High Energy Physics Group
Department of Physics, Blackett Laboratory
Imperial College London

A thesis submitted for the degree of
Doctor of Philosophy

September 2011

Abstract

The year 2010 saw the Large Hadron Collider (LHC) collect $35.1\,\mathrm{pb}^{-1}$ of $7\,\mathrm{TeV}$ proton-proton collision data. This thesis reports on the work carried out by the candidate as part of the calculation of the first constraints placed upon the supersymmetric parameter space using measurements made with this data. In particular, the development and application of the kinematic techniques used to ensure that the search was robust to detector mismeasurements, inherent in any early phase of data-taking, are discussed.

The Constrained Minimally Supersymmetric Standard Model (CMSSM) is introduced to demonstrate how supersymmetry may extend the Standard Model of particle physics, and is used as the benchmark signal to investigate how supersymmetry may appear in $7\,\mathrm{TeV}$ proton-proton collisions. The rôle of kinematics in early searches for such signals is then discussed; given the final state topology of interest (particle jets and large missing transverse momentum), particular attention is paid to errors that are due to detector mismeasurements, and how these may be accounted for with an appropriate choice of observable.

A search strategy based upon these principles and applied to the Compact Muon Solenoid (CMS) experiment is then described, as used in the first published search for supersymmetry with LHC data reported in Phys. Lett. B 698 (2011) 196. The kinematic characterisation of events discussed above is exploited to ensure that the search is robust to mismeasurement. The thesis concludes with a summary of the search results. The observed number of events fulfilling the signal criteria is compatible with that expected from the Standard Model alone. The subsequent exclusion limits, given at the 95% Confidence Level, place significantly greater constraints upon the supersymmetric parameter space than those of previous experiments.

Contents

Contents 4

List of Figures

List of Tables

Acknowledgements

TW

"...in a simlar way, at the Large Hadron Collider we could make many things. We could make Higgs bosons, micro-black holes – even dark matter. But it could be that the world's biggest experiment finds nothing at all.

Would that be a waste of five billion pounds?

No!

You see, those predictions are based upon our understanding of the universe at the moment.

If we find nothing, it means that we have got it wrong.

If we find nothing, it means that we will have to rewrite science.

If we find nothing, it means that we will need nothing short of a scientific revolution.

*And **that** is how finding nothing can be the best possible result."*

Adapted from the author's winning speech at the FameLab competition,

9th June 2009.

Chapter 1

Introduction

The Large Hadron Collider [1], or LHC, was designed to explore a new frontier in particle physics. The countless proton-proton collisions that have taken, are taking and will continue to take place underneath the Franco-Swiss border should give physicists access to the energy scales and integrated luminosities required to complete or extend the Standard Model of particle physics, or show once and for all a different approach is required to explain the fundamental interactions of matter.

The primary goal of the Large Hadron Collider (LHC) physics programme is to provide evidence for the existence of the spin zero boson associated with the Englert-Brout-Higgs-Guralnik-Hagen-Kibble (EBHGHK) mechanism[1] that offers a solution to the problem of massive particles in the Standard Model [2, 3, 4, 5]. Evidence for other forms of TeV-scale exotica, such as extra dimensions [6, 7], micro-black holes [8, 9], or supersymmetry [10] is also sought. Yet it could be that the phenomena preventing certain Standard Model (SM) processes from violating unitarity [11, 12, 13, 14] have eluded the imaginations of even the most fearless of theorists, and that the data emerging from the tunnels under Geneva will drag them back to the proverbial drawing board. In this sense, the LHC is very much a *discovery machine.*

---

[1] The EBHGHK mechanism is perhaps more commonly referred to as the Higgs mechanism.

How might one go about making such a discovery? Simplistically, one may frame the question in terms of hypotheses. The null hypothesis corresponds to a Nature described at the electroweak scale by the Standard Model alone. The alternative hypothesis (in the language of Neyman and Pearson) then pertains to a Nature described by some other theory that makes experimentally testable predictions differing in some way from those offered by the null hypothesis.

For instance, the experimental physicist – the observer – may identify some measurable characteristic of an experimental outcome that unambiguously identifies said outcome as being due to the new physics process of interest. The search then becomes a simple counting experiment. The observation of any number of these experimental signals, or events, allows the observer to reject the null hypothesis. If no other plausible explanation for the data is forthcoming, the discovery may be claimed.

Of course, the reality is never quite this straightforward. It is often difficult to find measurable properties, or observables, that can be uniquely associated with a particular new physics process. Instead, one or more observables are used to define a set of criteria that an outcome must satisfy in order to be counted as a signal event. One may then define the signal region as the phase space of values these observables may take that meet these criteria. Events outside of this region are discarded from the analysis.

Events associated with the null hypothesis (in this case, those due to SM processes) may also occupy the signal region. This may be due to the limitations of the experimental system, in which case the contribution is (in principle) reducible. Other classes of null hypothesis event may exhibit the same characteristics as the signal; these are, by definition, *irreducible* backgrounds. Both classes of background contributions to the signal event count must be estimated, and any discovery must be framed in terms of observing a number of signal events exceeding this estimate.

Supersymmetry – the subject of the work presented here – is an extension of the Standard Model that postulates the existence of supersymmetric partner fermions for the SM bosons, and vice versa. Assuming the Lightest Supersymmetric Particle (LSP) is stable, massive, weakly interacting and produced in pairs, the common observables associated with a supersymmetric event are a large missing transverse momentum, due to the disappearance of the LSPs from the detector, accompanied by cascades of particles created as heavier sparticles decay into the LSPs of the final state. The irreducible SM backgrounds therefore typically involve processes that produce neutrinos and accompanying hadronic activity.

There is currently no direct experimental evidence for supersymmetry[2]. In fact, aside from astrophysical and cosmological inferences, there are very few clues as to what form a supersymmetric theory of Nature should take. Even in the hugely simplified models used as benchmarks by sparticle hunters, there exists a vast parameter space of sparticle masses and coupling constants that each affect how supersymmetry might manifest itself experimentally. Thus to discover supersymmetry, one must come first in a race in which the location of the finish line is essentially unknown.

To maximise one's chances of winning, it makes sense to aim for the closest potential finish line. This is done by choosing the model with the largest production cross-sections and the signal region with the greatest prospects for detection in the observer's measurement system. This is the approach of the search described here. Benchmark points are selected in the parameter space of the Constrained Minimally Supersymmetric Standard Model (CMSSM), and the signal region of choice corresponds to events featuring only particle jets in the final state – the so-called "all-hadronic" channel. An estimate of the missing transverse momentum – the key signature of supersymmetric activity – is inferred from the vectorial sum of the measured jet transverse momenta.

---

[2] The anomalous positive muon magnetic moment $g - 2$ result [15] is not considered "direct" evidence, though a aupersymmetric interpretation has been offered [16, 17].

While such a strategy should maximise one's chances of making the discovery, the aim of "coming first" brings with it another set of challenges. Any experiment will suffer from the observer's unavoidable lack of knowledge about the accuracy and precision of the measurement system used to collect data in the early stages of running. Such uncertainties have an important impact on observables, such as the missing transverse momentum, that are based on a measurement of all activity in the event.

In the case of the search strategy described above, these uncertainties introduce an additional background: events where mismeasurements of the jet momenta result in a "fake" missing transverse momentum. While the probability of making a mismeasurement of the scale required to imitate a pair of disappearing sparticles should be small for a given measurement system, the overwhelming cross-section of susceptible events (namely those due to Quantum Chromodynamics processes featuring two or more jets) means that this background must be suitably accounted for. One could, of course, proceed to estimate its contribution to the signal event count as per the "real" missing transverse momentum backgrounds. Indeed, this is the method adopted by many of the supersymmetry searches in the literature.

This thesis is concerned with an alternative approach to the problem: that it is possible to formulate, from first principles, search strategies that are robust to the mismeasurements inherent in early data. That is to say, through the careful choice and combination of observables – in this case, those pertaining to the kinematic properties of each event – mismeasurement-induced backgrounds can be systematically excluded from the signal region. The work reported here aims to describe the author's contribution to the development of such a strategy based on this thesis, and its application to the first reported search for supersymmetry at the LHC [18].

1.1   Outline of the thesis

The motivations for a supersymmetric extension to the Standard Model, in terms of the aesthetic and pragmatic issues surrounding physics beyond the electroweak scale, are outlined in Chapter 2. A non-technical description of the CMSSM, a form of supergravity, is also presented and used to illustrate how supersymmetry may appear in $7\,\mathrm{TeV}$ proton-proton collisions.

Chapter 3 develops the thesis outlined above and describes the method used to remove the mismeasurement-induced background. The key to the method's robustness lies in the realisation that the two elements of the transverse jet measurements – namely the azimuthal angle and the magnitude of the deposited energy – are prone to differing degrees of mismeasurement. The choice of observables used to define a new variable, α_T, around which the method is based, exploits this feature. To demonstrate the working of the method from first principles a simplified measurement system – where the parameters describing the degree of mismeasurement can be explicitly controlled – is used in a toy analysis with simulated CMSSM and QCD collision events.

In order to select all-hadronic proton-proton collision events for the analysis, the full capabilities of the Compact Muon Solenoid (CMS) detector are required to reconstruct, identify and measure the properties of the collision products. Chapter 4 begins with an overview of the experiment. This is followed by a description of the process by which particle jets – central to the all-hadronic analysis – are reconstructed from the calorimeter outputs, as well the methods used to determine the jet-by-jet energy corrections and jet energy scale uncertainties. The reconstruction of other physics objects is then discussed, albeit more briefly.

A summary of the full analysis is presented in Chapter 5. The all-hadronic channel selection criteria are defined in terms of the physics objects discussed in the pre-

ceeding chapter. The search strategy is then outlined in full, describing how the α_T methodology of Chapter 3 is combined with the full detector information, other control variables and data-driven background estimates to search for an excess of supersymmetric signal events. No such excess was found in the 2010 data set, and so a discussion of the exclusion limits placed on the CMSSM parameter space as a result of these measurements concludes the thesis.

1.2   Overview of the studentship

After seven months of post-graduate lectures, the author went on Long Term Attachment (LTA) to CERN in May 2008, dividing time between work on the Silicon Strip Tracker (SST) spy channel (which, so as not to distract from the main thread of the thesis, is described briefly in Appendix B) and the all-hadronic α_T supersymmetry search. Upon return to the United Kingdom in March 2010, the author's time was spent developing the kinematic studies presented in Chapter 3 and continuing work on the α_T supersymmetry analysis. The 2010 data paper [18] was accepted for publication in March 2011. The remaining time was spent writing up the work presented here.

Chapter 2

Supersymmetry: From the Standard Model to Supergravity

"The question 'What kind of explanation may be satisfactory?'
thus leads to the reply: an explanation in terms of testable
and falsifiable universal laws and initial conditions. And an
explanation of this kind will be the more satisfactory the more
testable these laws are and the better they have been tested."

Karl Popper, *The Aim of Science (1957)*

2.1 The rôle of models in physics

The Standard Model of particle physics is one of the crowning achievements of twentieth centry physics. One might therefore think that it would be worthy of a more inspiring name; compare and contrast with the elegant Quantum Electrodynamics (QED) or the evocative Big Bang theory of cosmology. However, breaking the name down into its component parts there is method to the mundanity. "Standard" is straightforward enough to justify: the success of the Standard Model in describing the interactions of matter at energy scales of $\mathcal{O}(100 \text{ GeV})$ has helped it to gain the widespread acceptance it enjoys. The second part – "Model" – is worth exploring a

little further. When physicists speak of models, they are typically referring to what the Penguin Dictionary of Mathematics [19] describes as

> " *Any system of definitions, assumptions and equations*
> *set up to discuss particular natural phenomena.*"

Whether or not one accepts this definition as completely satisfactory, the pertinent word is "discuss". Models provide the frameworks that allow qualitative and, more importantly, quantitive predictions to be made and compared with experiment.

Going a little deeper, the term "model" has taken on a slightly more technical definition in the literature of theoretical particle physics. A model in this context refers to the Lagrangian density corresponding to a given physicist's description of the fundamental components of matter and their interactions. Such models may be constructed using a set of axioms, which are presented for convenience in the following subsection.

Thus, in this sense, the "Standard Model" really is the *standard model*, i.e. the Lagrangian describing how most physicists think matter works at the electroweak scale. The construction of the Standard Model, according to the axioms of § 2.1.1, is briefly outlined in § 2.1.2 to demonstrate the concepts discussed. § 2.1.3 then describes how the Standard Model – and indeed all such models – may be tested by experiment.

With these foundations in place, one may move on to models *beyond* the Standard Model. The work presented here will only focus on one particular class of model, inspired by what some have argued to be the last remaining spacetime symmetry – *supersymmetry*. This is the subject of the remainder of the chapter.

2.1.1   Model building

Following the approach of [20] et al. the fundamental quantity of classical mechanics
– the action, S – may be expressed as the time integral of the Lagrangian L. This
is the spatial integral of the Lagrangian density $\mathcal{L}$, and so

$$S = \int L \, \mathrm{d}t = \int \mathcal{L} \, \mathrm{d}^4 x, \tag{2.1}$$

where $\mathrm{d}^4 x$ is the 4-volume element. Generally speaking, $\mathcal{L}$ is a function of the
quantised fields and their derivatives. The equations of motion for these fields may
then be determined from the principle of least action. The Lagrangian formulation
is particularly convenient as all of the terms are, by construction, Lorentz invariant.
As is standard in the literature, the term "Langrangian" will henceforth be taken
to mean "Lagrangian density" and the integrals will be ignored.

The goal of the model-building exercise is the construction of the Lagrangian cor-
responding to how matter works at a given energy scale. Following the approach
described at [21][1] this process consists of three closely-related elements or axioms:

1. Choosing the gauge symmetries obeyed by the Lagrangian;

2. Choosing the field content;

3. Performing any Spontaneous Symmetry Breaking required.

Once all of these components are in place, the final Lagrangian is then the most
general renormalisable Lagrangian that it is possible to construct[2]. It is important
to note that the choices are (or at least should be) entirely based upon what is
observed in Nature. To elaborate on each axiom in turn:

---

[1] In particular, the approach presented in "The Standard Model" lectures of Y. Grossman.
[2] A renormalisable Lagrangian is one that features only terms that do not result in infinite
divergences when the integral calculations are performed.

1. **Choosing the gauge symmetries**: Symmetries regularly appear in Nature; indeed, the observation and categorisation of symmetries are an important part of science's explanatory and reductive power. In the context of model building, the model-builder must identify the gauge symmetries to be obeyed by the Lagrangian. This means that the fields of which $\mathcal{L}$ is a function, and their space-time derivatives, must transform as follows:

$$\phi(x) \mapsto \quad (\phi(x))' \;=\; U(x) \quad \phi(x) \tag{2.2}$$

$$D_\mu\,\phi(x) \mapsto (D_\mu\,\phi(x))' \;=\; U(x)\,D_\mu\,\phi(x), \tag{2.3}$$

   where $\phi(x)$ is a generic field that transforms when operated on by the generic transformation $U(x)$. The x dependence of $U(x)$ indicates the local, or gauge, nature of the symmetry transformation[3]. $U(x)$ will, generally speaking, depend on a set of parameters that describe the symmetry, and the number and nature of these will depend upon the group structure of the symmetry. The term D_μ (as opposed to ∂_μ) is used to indicate that a *covariant derivative*, featuring a gauge field term, is required to maintain invariance under the transformation. This leads to additional field content, as discussed below.

2. **Choosing the field content**: The fields present in a given Lagrangian ultimately represent the fundamental constituents of matter thought to exist in Nature. They can be real (i.e. scalar), complex or spinor in nature, and, depending on the group structure of the symmetries they obey, may be grouped into singlets or multiplets. The terms of the Lagrangian representing the fields can be loosely classified as follows:

   - *Free terms*, including the kinematic and mass terms, that describe the free particle behaviour corresponding to the "edges" in Feynman diagrams;

---

[3] To be compared with a *global* symmetry, where the transformation does not depend on the spacetime coordinate x.

- *Interaction terms* that specify which fields couple to each other, i.e. the permitted Feynman diagram vertices;

- *Yukawa terms* that allow fields to acquire mass while maintaining the renormalisability of the theory. These arise due to Spontaneous Symmetry Breaking (SSB);

- *Renormalisation terms* that arise due to the choice of gauge.

3. **Performing any Spontaneous Symmetry Breaking required**: The gauge fields introduced to ensure the symmetry of the Lagrangian are massless; that is to say there are no terms of the form $M_A A^\mu A_\mu$ where A_μ is the gauge field in question. The *ad hoc* addition of such terms would break the gauge invariance. However, Nature appears to demand massive gauge bosons, and in the Standard Model this is achieved through Spontaneous Symmetry Breaking (SSB). In a nutshell, additional fields are introduced to the Lagrangian that have a non-zero Vacuum Expectation Value (VEV). The extra degrees of freedom introduced by these fields are then either "eaten" by the target gauge bosons (giving them an apparent mass) or manifest as additional physical particles in the model. This is the Englert-Brout-Higgs-Guralnik-Hagen-Kibble (EBHGHK) mechanism [2, 3, 4, 5]. It should be noted that, in addition to the free, interaction and Yukawa terms introduced by performing the SSB, the choice of gauge required to maintain renormalisability results in additional gauge-fixing terms and terms corresponding to unphysical particles known as Faddeev-Popov ghosts. However, these renormalisation terms are only important when performing explicit calculations with a given model, and so are not discussed here.

These steps are by no means sequential. The transformations corresponding to a given symmetry require fields to act upon, while symmetries and symmetry breaking generally result in additional field content. Indeed, the Standard Model has

taken some time to build from a plethora of experimental observations, conceptual understandings and an ever-expanding mathematical toolkit. For convenience, therefore, the construction of the Standard Model with respect to these axioms is briefly presented in the following subsection.

2.1.2 Building the "Standard Model"

Nature is observed to obey the $SU(3)_C \times SU(2)_L \times U(1)_Y$ gauge symmetries at the electroweak scale, where $SU(3)_C$ corresponds to the strong force, as described by Quantum Chromodynamics (QCD) [22, 23] and $SU(2)_L \times U(1)_Y$ corresponds to the unified weak and electromagnetic forces [24, 25, 26]. The EBHGHK mechanism breaks the $SU(2)_L \times U(1)_Y$ symmetry to the $U(1)$ of QED[4].

There are two families of matter fields: *quarks* and *leptons*. They possess an intrinsic spin of 1/2; thus they obey Fermi statistics and are represented by *spinors*. There are three generations in each family, and each generation features two *flavours* (resulting in a total of twelve flavours). The electroweak force is known from experiment to be *chiral*, that is to say fields that are defined to be "left-handed" transform differently to "right-handed" fields. It is therefore convenient to decompose the fields into left- and right-handed components, and to group these into one isospin doublet and two isospin singlets respectively: $q_L \equiv (q_L, ꭓ_L)$, q_R and $ꭓ_R$ for the quarks[5]; and $l_L \equiv (\nu_L, l_L)$, ν_R and l_R for the leptons[6]. Additionally, each field has an anti-matter partner. These are denoted with the bar notation, e.g. $\bar{q}_L$. Hence there are 48 unique matter fields that appear in the Standard Model Lagrangian.

---

[4] See, for example, §3.1 of [27] for a retrospective discussion.

[5] The q and ꭓ represent the up-type and down-type quarks respectively. An upside down q is used to avoid the use of u and d, which would suggest only the first generation.

[6] Only left-handed (right-handed) neutrinos (antineutrinos) have been observed experimentally [28]. However, evidence for neutrino oscillations [29, 30] suggests that neutrinos do have a mass, which would mean it is possible to move to a reference frame where a left-handed neutrino has a postive helicity. Thus it is noted that the ν_R singlet is included here for completeness, even though it is not technically part of the Standard Model.

The propensity of a field to transform under a given symmetry is characterised by a quantum number (charge) identified with that symmetry. In addition to the isospin quantum number, leptons and quarks also possess *hypercharge*. Upon SSB, isospin and hypercharge combine to give the more familiar electric charge of electromagnetism, of which quarks (leptons) possess a fractional (integer) value.

Quarks also have a quantum number that the leptons do not – *colour* – and as such experience the strong force. The $SU(3)_C$ nature of the strong force means each flavour of quark may assume one of three different colours, and the corresponding gauge transformations rotate the quarks in colour space. However, the quarks' colour indices are usually suppressed when written in the Lagrangian.

The covariant derivatives must transform in the same way as their corresponding matter fields in order for the model to be gauge invariant. As discussed, this is ensured by introducing new gauge fields to the Lagrangian. The covariant derivatives for the four types of matter field (quarks and leptons, left- and right-handed) may be found in Table 2.1. The gauge terms have been aligned according to the gauge symmetries for clarity. Inspecting the terms:

- $T^a_{\;ij}$ and $A^a_{\;\mu}$ (where $a = 1, 2, 3$) are the generators and gauge fields of $SU(2)_L$ respectively, where $T^a_{\;ij} = \frac{1}{2}\sigma^a_{ij}$ and σ^q are the Pauli matrices;

- $Y(f)$ is the hypercharge value for the fermion field f and B_μ is the $U(1)_Y$ gauge field;

- $T^b_{s\;mn}$ and G^b_μ (where $b = 1, \ldots, 8$) are the generators and gauge fields of $SU(3)_C$ respectively.

These gauge fields each require a field strength term in the Lagrangian that describes the kinetic behaviour of the fields. With the electroweak force, the field strength

$$D_\mu\, l_L(x)_i = \partial_\mu\, l_L(x)_i + ig\, T^a{}_{ij}\, A^a{}_\mu\, l_L(x)_j + ig'\, Y(l_L)\, B_\mu\, l_L(x)_i \tag{2.4}$$

$$D_\mu\, l_R(x) = \partial_\mu\, l_R(x) + ig'\, Y(l_R)\, B_\mu\, l_R(x) \tag{2.5}$$

$$D_\mu\, q_L(x)_{i|m} = \partial_\mu\, q_L(x)_{i|m} + ig\, T^a{}_{ij}\, A^a{}_\mu\, q_L(x)_{j|m} + ig'\, Y(q_L)\, B_\mu\, q_L(x)_{i|m} + ig_s\, T^b_{s\ mn}\, G^b_\mu\, q_L(x)_{i|n} \tag{2.6}$$

$$D_\mu\, q_R(x)_m = \partial_\mu\, q_R(x)_m + ig'\, Y(q_R)\, B_\mu\, q_R(x)_m + ig_s\, T^b_{s\ mn}\, G^b_\mu\, q_R(x)_n \tag{2.7}$$

$$D_\mu\, \Phi(x)_i = \partial_\mu\, \Phi(x)_i + ig\, T^a{}_{ij}\, A^a{}_\mu\, \Phi(x)_j + ig'\, Y(\Phi)\, B_\mu\, \Phi(x)_i \tag{2.8}$$

Table 2.1: Covariant derivatives of the left-handed lepton fields $l_L(x)_i$ (Eq. 2.4), the right-handed lepton fields $l_R = \nu_R, l_R$ (Eq. 2.5), the left-handed quark fields $q_L(x)_{i|m}$ (Eq. 2.6), the right-handed quarks $l_R = q(x)_m, b(x)_m$ (Eq. 2.7), and the EBHGHK doublet before SSB (Eq. 2.8). Note that the position of the field in the weak isospin doublet is denoted by the i, j indices, and the colour indices are denoted by m, n.

terms in the Lagrangian are as follows:

$$\mathcal{L}_{\text{EWK}} = -\frac{1}{4} A^{a\,\mu\nu} A^{a}_{\;\;\mu\nu} - \frac{1}{4} B^{\,\mu\nu} B_{\mu\nu} + \sum_q \mathcal{L}_q + \sum_l \mathcal{L}_l \qquad (2.9)$$

where

$$A^{a\,\mu\nu} = \partial^{\,\mu} A^{a\,\nu} - \partial^{\,\nu} A^{a\,\mu} - g\,\epsilon_{abc}\, A^{b\,\mu} A^{c\,\nu} \qquad (2.10)$$

$$B^{\,\mu\nu} = \partial^{\,\mu} B^{\,\nu} - \partial^{\,\nu} B^{\,\mu} \qquad (2.11)$$

$$\mathcal{L}_q = i\,\bar{\text{q}}_{L\,i}\,\gamma^{\mu}\, D_{\mu}\,\text{q}_{L\,i} + i\,\bar{\text{q}}_R\,\gamma^{\mu}\, D_{\mu}\,\text{q}_R + i\,\bar{\text{b}}_R\,\gamma^{\mu}\, D_{\mu}\,\text{b}_R \qquad (2.12)$$

$$\mathcal{L}_l = i\,\bar{\text{l}}_{L\,i}\,\gamma^{\mu}\, D_{\mu}\,\text{l}_{L\,i} + i\,\bar{\nu}_R\,\gamma^{\mu}\, D_{\mu}\,\nu_R + i\,\bar{\text{l}}_R\,\gamma^{\mu}\, D_{\mu}\,\text{l}_R, \qquad (2.13)$$

noting that the covariant derivative terms may be found in Table 2.1, and that the $A^a_{\;\;\mu}$ and B_{μ} gauge fields do not correspond to physical particles[7]. The electroweak kinetic terms do not give rise to massive gauge boson terms as things stand, and inserting mass terms by hand spoils the gauge invariance. Thus, the EBHGHK field is introduced to spontaneously break the $SU(2)_L \times U(1)_Y$ symmetry. This is a complex scalar doublet that has four degrees of freedom that may be parameterised as follows:

$$\Phi(x) = \frac{1}{2}\, e^{iT^a \alpha^a(x)} \begin{pmatrix} 0 \\ v + h(x) \end{pmatrix}, \qquad (2.14)$$

where T^a are the generators of $SU(2)_L$, $\alpha^a(x)$ are the three Goldstone Boson fields that are "eaten" by the $W^{\pm}$ and Z bosons upon switching to the unitary gauge, $v = \mu/\sqrt{\lambda}$ is the non-zero VEV of the EBHGHK potential

$$V(\Phi) = -\mu^2 \Phi^* \Phi + \lambda\,|\Phi^* \Phi|^2, \qquad (2.15)$$

and $h(x)$ is the scalar field corresponding to the (as-yet unobserved) EBHGHK boson. The covariant derivative for the EBHGHK doublet is given in Eq. 2.8 in Table 2.1, and adding the resulting kinetic terms (as well as the potential terms) to the electroweak part of the Lagrangian gives

$$\mathcal{L}'_{\text{EWK}} = \mathcal{L}_{\text{EWK}} + \mathcal{L}_{\Phi} \qquad (2.16)$$

$$= \mathcal{L}_{\text{EWK}} + (D_{\mu}\,\Phi)^{\dagger}\,(D^{\,\mu}\,\Phi) - \mu^2 \Phi^* \Phi + \lambda\,|\Phi^* \Phi|^2 \qquad (2.17)$$

---

[7] Again, the neutrino term in Equation 2.13 is included for completeness.

Taking the terms from the covariant derivative – which, as shown in Equation 2.8, feature A and B fields – and defining the mass eigenstates of the electroweak gauge bosons as

$$W_\mu^\pm = \frac{A^1_{\ \mu} \mp iA^2_{\ \mu}}{\sqrt{2}}, \quad Z_\mu^0 = \frac{gA^3_{\ \mu} - ig'B_\mu}{\sqrt{g^2 + g'^2}}, \quad \text{and} \quad A_\mu = \frac{g'A^3_{\ \mu} - igB_\mu}{\sqrt{g^2 + g'^2}}, \quad (2.18)$$

the electroweak Lagrangian becomes

$$
\begin{aligned}
\mathcal{L}'_{\text{EWK}} \ = \ & \mathcal{L}_{\text{EWK}} + \mathcal{L}_{\Phi\,\text{kin.}} + \mathcal{L}_{\text{int.}} + V(\Phi) \\
& + \ \tfrac{1}{2}g\,v\,W_\mu^\pm W^{\pm\mu} \\
& + \ \tfrac{1}{2}\sqrt{g^2 + g'^2}\,v\,Z^0_{\ \mu} Z^{0\mu},
\end{aligned}
\quad (2.19)
$$

and it may be seen how the kinetic term $|D_\mu\Phi(x)|^2$ gives rise to the gauge boson mass terms, $M_W = \tfrac{1}{2}gv$, $M_Z = \tfrac{1}{2}\sqrt{g^2 + g'^2}v$ (as well as the EBHGHK kinetic and interation terms). It should also be noted that the change of basis of Equation 2.18 ensures that the photon field A_μ is massless, i.e. $M_A = 0$.

Thus the introduction of the EBHGHK field permits the appearance of Dirac mass terms[8] for the fermions, which are otherwise forbidden by the chiral nature of the fields (the left-handed doublets cannot couple to the right-handed singlets). The terms responsible are the *Yukawa terms* of the Lagrangian, of the general form $-Y_f\,\bar{f}_L^i\Phi_i\,f_R$, where Y_f is the Yukawa coupling for that fermionic field and i represents the $SU(2)_L$ isospin index. The resultant Dirac fermion mass term (with left- and right-handed terms combined) is then

$$m_f\,\bar{f}\,f \equiv Y_f\,v\,\bar{f}\,f = Y_f\,\frac{\mu}{\sqrt{\lambda}}\left(\bar{f}_L f_R + \bar{f}_R f_L\right). \quad (2.20)$$

It is noted that there are also inter-generational Yukawa terms for the quarks, and that these give rise to the mixing of the weak eigenstates described by the Cabibbo-Kobayashi-Maskawa (CKM) matrix [32, 33]. A full treatment is not given here;

---

[8] As opposed to a Majorana mass term; a Majorana particle is its own antiparticle [31] (with thanks to E. Recami for the translation of the paper title).

rather, it is sufficient to note that this matrix introduces four additional free parameters to the Standard Model (traditionally expressed as three mixing angles and a complex phase). Likewise, it is noted that the Standard Model makes no attempt to incorporate neutrino masses, in conflict with the experimental observation of neutrino oscillations [29, 30].

2.1.3   Testing the Standard Model

The Standard Model has been constructed, albeit somewhat hastily for the sake of brevity. In doing so, a number of free parameters have been introduced[9]. These are:

- the three gauge couplings: g, g' and g_s;

- the two EBHGHK potential couplings: μ and λ;

- the nine charged fermion masses: M_u, M_d, M_c, M_s, M_t, M_b, M_e, M_μ and M_τ;

- the four CKM matrix parameters (three mixing angles and a complex phase).

These free parameters are variables of the model, estimates of which must be extracted from experiment. The fact that there are nineteen or so, however, may be regarded as a flaw in the Standard Model. For many theorists, this is eighteen parameters too many for a truly elegant description of Nature.

What is the use, then, of defining and measuring the parameters listed above? As the quotation at the start of this Chapter suggests, the strength of a given model or theory lies in its predictive power – its *testability*. If a model is constructed such that

---

[9] There is also the parameter associated with $F^a_{\mu\nu} \tilde{F}^{a\mu\nu}$ QCD coupling term, θ_{QCD}. Such a coupling is permitted by gauge invariance; however, a non-zero value of θ_{QCD} would result in strong force contributions to CP-violating quantities such as the electric dipole moment of the neutron. Thus this free parameter is thought, from experiment, to be zero. This is known in the literature as the "strong CP" problem [34, 35, 36].

there is some way of checking that the otherwise independent parameters are consistent, and that this consistency can be confirmed by experimental measurements, this presents a powerful case for the defence of the model.

Perhaps the best example of such a test for the Standard Model is the relation between M_W, M_Z and $\cos\theta_W \equiv g/\sqrt{g^2 + g'^2}$, where θ_W is the mixing angle between the neutral gauge bosons. This relation is described by ρ, where

$$\rho \equiv \frac{M_W^2}{M_Z^2 \cos^2\theta_W} \tag{2.21}$$

At tree-level, $\rho = 1$ in the Standard Model, and indeed experimental measurements confirm this[10]. (The ρ-parameter relation is, in fact, such an important test that many new physics models – including supersymmetry – incorporate it from the outset with the inclusion of a global *custodial SU(2)* symmetry that guarantees $\rho = 1$ [38].)

Why emphasise this distinction between parameter measurement and model testing? As will become apparent from the remainder of the chapter, such a discussion is important in terms of identifying what is to be achieved with searches for physics beyond the Standard Model. Supersymmetric models require the introduction of new symmetries, new matter and gauge fields, more instances of SSB, and many, many more free parameters. Thus it is instructive to stress that, in terms of interpreting Nature, any discussion of supersymmetry is very much in the "model building" phase, as opposed to "model testing". This is in-keeping with the notion that the LHC is a discovery machine. Before embarking on a description of supersymmetric model building, however, the various motivations for believing that supersymmetry offers a promising avenue for extending the Standard Model are presented.

---

[10] In fact, the LEP electroweak precision tests (see, for example, [37]) confirm the need for higher-order corrections at the percent level.

2.2   Supersymmetry

The successes of the Standard Model at the electroweak scale are impressive. However, the model is not complete. Many theories have been proposed that attempt to go beyond the Standard Model, with varying degrees of success. The work presented here will focus on a class of theories that may be linked through the invocation of a new symmetry of Nature - *supersymmetry*. While there is, as discussed in Chapter 1, no experimental evidence for supersymmetry, it is one of the more popular candidate theories. The following subsections address the reasoning behind supersymmetry's popularity, addressing the theoretical (or aesthetic) motivations in § 2.2.1, the pragmatic motivations in § 2.2.2, and some of the incidental motivations in § 2.2.3.

2.2.1   The last spacetime symmetry

Of all the arguments in favour of a supersymmetric extension to the Standard Model, perhaps the most compelling is that supersymmetry is the "last spacetime symmetry". To process this rather grandiose statement, one should note that, in this context, "spacetime" is synonymous with "external". One may classify the symmetries applied to fields/particles as either "internal" or "external". The former refers to a symmetry of some otherwise hidden property of the particle. For example, hypercharge, isospin, colour – indeed, all of the symmetries discussed in § 2.1 – are internal symmetries. As mentioned previously, each symmetry has an associated operator. The form of this operator depends upon the mathematical properties of the symmetry group.

External symmetries, on the other hand, refer to properties of the particle with respect to spacetime. Invariance under translations, rotations and Lorentz boosts are all examples of external symmetries, and these too have corresponding operators that act on the fields. In fact, the *Coleman-Mandula* theorem [39] implies that

these are the *only* permitted external symmetries, with further symmetries rendering Nature incapable of the interactions required to make life interesting.

There is, however, a loophole (so to speak). Coleman and Madula did not consider half-integer spin values in their theorem. As it happens, the theorem can be expanded to incorporate transformations that change a particle's spin by half-integer values; this is known as the *Haag–Lapuszański–Sohnius* extension. Furthermore, it can be shown that this *really is* the final external symmetry allowed for a non-trivial theory of matter [40]. Thus the claim of the subsection heading is, to an extent, justified.

The famous implications of this new external symmetry are as follows. One defines an operator that transforms a given fermionic field to a bosonic field, and vice versa:

$$Q\,f(x) = \quad b(x) \tag{2.22}$$

$$Q\,b\,(x) = \quad f(x) \tag{2.23}$$

Such an operator Q must possess half-integer spin itself; it is therefore represented by a spinor. Every Standard Model particle is therefore postulated to have a *superpartner* with a spin that differs by $1/2$ – the *sparticles*. Before proceeding, it is worth bearing in mind the following health warnings:

- In addition to the concept of internal and external symmetries, one must also consider whether a symmetry is global or local. In the simplistic picture painted with Equations 2.22 and 2.23, Q is a global transformation. To *localise* supersymmetry (i.e. make the transformations spacetime-dependent), one is forced to incorporate gravity[11]. While some would argue that this is actually a good thing (see § 2.2.3), it does lead to complications regarding the renormalisability of the resulting models.

---

[11] A spacetime dependence of the supersymmetry operators requires terms in the covariant derivatives that have spin 1 and spin $1/2$ components, resulting in a field with a total spin of $3/2$. This is postulated to be the *gravitino*, which may be identified as the superpartner of the spin 2 *graviton* [41, 42, 43].

- Likewise, Equations 2.22 and 2.23 would require the supersymmetric partner particles – the *sparticles* – to have the same mass as their Standard Model partner. Observation tells us that this is not the case, and so if supersymmetry is realised in Nature it must be *broken*. The implications of this will be broached in § 2.3.2.

Nevertheless, the concept that every field has a superpartner not only helps with fixing the Standard Model – as discussed in the following subsection – but ultimately provides a mechanism for linking matter (half integer spin) with forces (integer spin). Such a notion – however grounding the practicalities of actually imposing supersymmetry turn out to be – is hard for even the most unromantic physicist to completely ignore.

2.2.2 Fixing the Standard Model

It is all very well to have a beautiful theory. However, aesthetics must be left to the mathematicians; physicists should ultimately take a pragmatic approach when choosing between differing descriptions of Nature. Why, then, should physicists entertain the notion of supersymmetry?

The answer lies with the missing piece of the Standard Model. The complex scalar field introduced to spontaneously break the $SU(2)_L \times U(1)_Y$ symmetry leaves an uneaten scalar field that appears as the EBHGHK boson. Aside from the fact that this particle has not yet been observed experimentally, there is a theoretical issue associated with the way that the model includes a scalar field that couples to the other massive fields.

When calculating the effective mass of a given field, higher-order contributions appear due to the loop diagrams permitted by the coupling terms in the Lagrangian.

As mentioned in § 2.1.2, the EBHGHK field couples via the Yukawa terms to every massive field. The resulting loop diagrams from generic fermionic and bosonic fields are shown in Figures 2.1 a) and b) respectively.

a)   *b)*
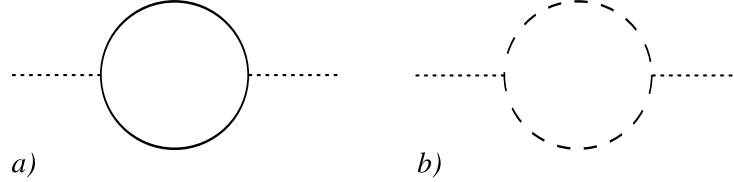
Figure 2.1: Single loop contributions to the effective mass of a scalar field (dotted line) from a) a fermionic field (solid line) and b) a bosonic field (dashed line).

The contribution to the mass-squared of the scalar field, M_s^2, from a generic fermionic field loop – Figure 2.1 a) – is given by

$$\delta M_f^2 \sim -\frac{Y_f}{8\pi^2}\Lambda^2 \tag{2.24}$$

where Y_f is the Yukawa coupling of the fermionic field to the scalar field, and Λ is known as the "cut-off energy scale", below which the Standard Model may be thought of as an *effective theory* that is representative of some underlying physics. The minus sign that arises from fermionic nature of the loop should be noted. The corrected mass (squared) of the scalar field is then

$$M_s^2 \sim M_s'^2 + \delta M_f^2 = M_s'^2 - \frac{Y_f}{8\,\pi^2}\Lambda^2 \tag{2.25}$$

where M_s' is the *bare mass* of the scalar field. Using $\Lambda \sim M_P \sim 10^{19}\,\mathrm{GeV}$ (where M_P is the Planck mass) and $Y_f \sim 1$ (for the top quark), it becomes apparent that M_s' must be "fine-tuned" to the order of one part in 10^{30}. While technically possible, such an adjustment leaves many theorists deeply uncomfortable. The issue of quadratic divergences in the scalar field mass calculation is what is widely referred to as the *hierarchy problem*.

How does supersymmetry help? The corresponding mass (squared) contribution due to bosonic loops of the type shown in Figure 2.1 is

$$\delta M_b^2 \sim +\frac{Y_b}{16\pi^2}\,\Lambda^2, \tag{2.26}$$

where it is noted that the bosonic contribution is *positive*. As discussed in § 2.2.1, if every fermionic field that coupled to the EBHGHK field had a bosonic superpartner field with $Y_f \sim Y_b$ the contributions to M_s^2 would systematically cancel out to leave M_s' needing only a "sensible" level of tuning, i.e.

$$M_s^2 \sim M_s'^2 + \delta M_f^2 + \delta M_b^2 + \delta M_b^2 = M_s'^2 + \frac{1}{16\,\pi^2}\,[-2Y_f + Y_b + Y_b]\,\Lambda^2 \tag{2.27}$$

where it is noted in passing that, loosely speaking, there are two bosonic fields to every partner fermionic field to ensure that the number of degrees of freedom match (see § 2.3.1). This is a necessarily vague exposition of the argument; for a more in-depth discussion the reader is referred to Chapter 1 of [44]. Nevertheless, it is possible to appreciate that if one accepts the existence of a fundamental scalar field, a model that offers a systematic cancellation of the resulting quadratic divergences through the introduction of a new symmetry is very attractive from a theoretical perspective. Before discussing how supersymmetric models might actually be built, however, it is worth briefly mentioning a number of auxiliary motivations for considering Nature to be supersymmetric.

2.2.3   Incidental motivations for supersymmetry

Historically, supersymmetry emerged as a solution to the hierarchy problem some time after its inception in the 1970s, having been initially rejected due to the lack of sparticles with masses matching the particles known at the time. A number of other beneficial features have been reported in the literature as supersymmetry has been subjected to further scrutiny. In no particular order, these are discussed in what follows:

- **Grand unification**: As shall be seen in the next section, imposing supersymmetry on the Standard Model involves the introduction of a multitude of new parameters – much to the chagrin of those seeking a simpler Theory of Everything. As if to appease such complaints, it turns out that attempts to absorb $SU(3)_C \times SU(2)_L \times U(1)_Y$ into one $SU(5)$ symmetry, as first suggested in [45], improve when supersymmetry is taken into account. It is observed that, in the case of the Standard Model, the running of the force coupling constants [46] is such that the three forces unite at roughly $\Lambda \sim 10^{15}\,\text{GeV}$. However, this unification is not particularly precise; additionally, one is forced to bear the burden of the hierarchy problem due to the de facto cut-off scale Λ. A supersymmetric unification [47] not only solves the hierarchy problem, but provides the additional radiative corrections to the Renormalisation Group Equations (that determine the running of the force coupling constants) for a more exact unification at $\Lambda \sim 10^{16}\,\text{GeV}$ [45].

- **Gravity**: Continuing the theme of unifying the fundamental forces, it has been noted that a glaring omission from the Standard Model is gravity. While the problems associated with incorporating spin 2 gravitons into a renormalisable model remain, the localisation of supersymmetry requires the introduction of a spin $3/2$ sparticle – the *gravitino* – and its spin 2 partner that may be identified as the graviton [41, 42, 43]. Given that that all of the symmetries of the Standard Model are local, that gravity is a natural consequence of localising supersymmetry makes for a seductive argument in favour of supersymmetry.

- **Cold Dark Matter**: The final incidental motivation to be mentioned here is the result of an almost ideologically pleasing convergence of the goals of particle physics and cosmology. The Λ-CDM model of cosmology, as defined by the Wilson Microwave Anisotropy Probe (WMAP) Collaboration [48, 49], describes the evolution of the Universe a few seconds after the "Big Bang" with

just six parameters. According to the latest experimental observations [48, 49][12], the matter density is

$$\Omega_M = (0.274 \pm 0.012)\,, \tag{2.28}$$

where the quoted values from [48, 49] are $\Omega_M\, h^2 = (0.136 \pm 0.004)$ and $h = (0.705 \pm 0.013)$ with errors combined in quadrature[13]. This is to be contrasted with the limit on the the baryonic matter density,

$$\Omega_B = (0.0457 \pm 0.0021)\,, \tag{2.29}$$

where the quoted value from [48, 49] is $\Omega_B\, h^2 = (0.0227 \pm 0.0006)$. There is a lot of non-baryonic matter to be accounted for. This is where supersymmetry leaps to the rescue. Assuming R-parity is conserved (see § 2.3.1), the Lightest Supersymmetric Particle (LSP) must be stable. If this LSP is massive and electrically neutral, it becomes a promising candidate for the Cold Dark Matter (CDM) of the Λ-CDM model of cosmology. Furthermore, this relationship can be inverted to place constraints on the supersymmetric parameter space based on astrophysical observations.

Such motivations have held sway with theorists for some time now; indeed, one could dedicate a whole chapter to each of the topics raised above. For now, though, the discussion turns to the construction of supersymmetric models.

---

[12] See § [50] (O. Lakov and A. R. Liddle) for a summary of the definition, interpretation and latest values of the various cosmological parameters that feature in the literature. The estimates quoted here are those that also incorporate data from Baryonic Acoustic Oscillations (BAOs) and Type Ia supernovae measurements (as opposed to only the WMAP data).

[13] The uncertainties in [48, 49] are quoted at the 68% CL, but care must be taken when extrapolating from them due to non-Gaussian likelihoods and assumed priors.

2.3 The construction of supergravity models

Having outlined the motivations for a supersymmetric extension to the Standard Model, one may now proceed to describe the construction of supersymmetric models. This may loosely be thought of in terms of: 1) imposing a (minimal) supersymmetry on the Standard Model, as discussed in § 2.3.1, and 2) spontaneously breaking the supersymmetry to ensure that the new sparticles have different masses to their Standard Model counterparts, as discussed in § 2.3.2. A full mathematical treatment of these steps is beyond the scope of this work. The discussion, based largely on [51, 44], will therefore remain largely non-technical. The model building framework set out in § 2.1.1 is used to emphasise the pertinent points. Of most interest to the experimental physicist is how supersymmetry might appear in LHC collisions. A discussion of issues such as sparticle production processes, sparticle mass spectra and decay chains therefore concludes the chapter (§ 2.3.3).

2.3.1 The Minimally Supersymmetric Standard Model

The simplest way of imposing a supersymmetry upon the Standard Model is, as the discussion in § 2.2.1 suggests, to add a supersymmetric partner field for every Standard Model field differing in spin by 1/2. This doubling of the field content results in what is known as the Minimally Supersymmetric Standard Model (MSSM). However, the simplistic picture painted by § 2.2.2 needs refining. A spin 1/2 fermionic field, represented by a spinor ψ, has four degrees of freedom, while the spin 0 complex scalar field $\tilde{\phi}$ only has two. Thus it is necessary to introduce an additional complex scalar field F to make sure that the degrees of freedom match up in regular space and "superspace". These fields are grouped into what is known as a *supermultiplet*:

$$\mathbf{\Psi} \supset \left(\tilde{\phi}, \, \psi, \, F \right). \tag{2.30}$$

The fermionic fields of the Standard Model are chiral, so one may further arrange the supermultiplets into *chiral supermultiplets*. This is done for one generation in Table 2.2a, listing the relevant quantum numbers where appropriate. The spin 1 gauge fields are catered for with a *vector supermultiplet* consisting of the vector field A_μ (3 bosonic dof), a spin 1/2 Majorana spinor field $\tilde{\lambda}$ (4 fermionic dof) and a real auxiliary pseudoscalar field D (1 bosonic dof),

$$\mathbf{A} \supset \left(A_\mu, \, \tilde{\lambda}, \, D \right). \tag{2.31}$$

The vector supermultiplet fields of the MSSM are presented in Table 2.2b. The bosonic superpartners of fermionic fields are named by preappending "s-" to the original fermionic field; likewise, "-ino" is appended to the bosonic field's name for its fermionic superpartner field. It is also noted that the gauge eigenstates are, generally speaking, different to the mass eigenstates. Where possible this has been indicated in Tables 2.2a and 2.2b; where the issue is complicated by SSB the mass eigenstates are listed separately.

An important deviation from the Standard Model (aside from the superpartner fields) to highlight is the inclusion of a second EBHGHK doublet Φ_2. This is required to ensure that the EBHGHKino contributions to the left-handed fermionic gauge anomaly cancel out, as they do in the Standard Model.

Following the example of the EBHGHK potential of Eq. 2.15, it is convenient to define the *super potential* W. An analytic function of the chiral supermultiplets featured in Table 2.2a, W may be used to generate various terms of the Lagrangian. The following terms can describe all of the matter interactions and the Yukawa terms:

$$W = \bar{q} \, \mathbf{y}_{\bar{q}} \, Q \, H_\uparrow - \bar{d} \, \mathbf{y}_{\bar{d}} \, Q \, H_\downarrow - \bar{l} \, \mathbf{y}_{\bar{l}} \, L \, H_\downarrow + \mu \, H_\uparrow \, H_\downarrow, \tag{2.32}$$

where $\mathbf{y}_{\bar{q}}$, $\mathbf{y}_{\bar{d}}$ and $\mathbf{y}_{\bar{l}}$ are 3×3 matrices of (dimensionless) Yukawa coupling parameters in generation space and μ is the supersymmetric version of the EBHGHK

Supermultiplet	Spin 0				Spin 1/2				$SU(3)$?	T^3	Y	Q
	Name	Gauge	Mass	P_R	Name	Gauge	Mass	P_R				
Q	Squarks	$(\tilde{q}_L, \tilde{d}_L)$	$(\tilde{q}_1, \tilde{d}_1)$	-1	Quarks	(q_L, b_L)	(q_1, b_1)	$+1$	Yes	$(+\frac{1}{2}, -\frac{1}{2})$	$+\frac{1}{6}$	$(+\frac{2}{3}, -\frac{1}{3})$
$\bar{q}$		$\tilde{q}_R^*$	$\tilde{q}_2^*$	-1		$q_R^\dagger$	$q_2^\dagger$	$+1$	Yes	0	$+\frac{2}{3}$	$+\frac{2}{3}$
$\bar{d}$		$\tilde{d}_R^*$	$\tilde{d}_2^*$	-1		$b_R^\dagger$	$b_2^\dagger$	$+1$	Yes	0	$-\frac{1}{3}$	$-\frac{1}{3}$
L	Sleptons	$(\tilde{\nu}_L, \tilde{l}_L)$	$(\tilde{\nu}_1, \tilde{l}_1)$	-1	Leptons	(ν_L, l_L)	(ν_1, l_1)	$+1$	No	$(+\frac{1}{2}, -\frac{1}{2})$	$-\frac{1}{2}$	$(0, -1)$
$\bar{\nu}$		$\tilde{\nu}_R^*$	$\tilde{\nu}_2^*$	-1		$\nu_R^\dagger$	$\nu_2^\dagger$	$+1$	No	0	0	0
$\bar{l}$		$\tilde{l}_R^*$	$\tilde{l}_2^*$	-1		$l_R^\dagger$	$l_2^\dagger$	$+1$	No	0	-1	-1
$H_\uparrow$	EBHGHK	$(H_\uparrow^+, H_\uparrow^0)$		$+1$	EBHGHKinos	$(\tilde{H}_\uparrow^+, \tilde{H}_\uparrow^0)$	$-$	-1	No	$(+\frac{1}{2}, -\frac{1}{2})$	$+\frac{1}{2}$	$(+1, 0)$
$H_\downarrow$		$(H_\downarrow^+, H_\downarrow^0)$		$+1$		$(\tilde{H}_\downarrow^+, \tilde{H}_\downarrow^0)$	$-$	-1	No	$(+\frac{1}{2}, -\frac{1}{2})$	$-\frac{1}{2}$	$(0, -1)$

(a) The chiral supermultiplets of the MSSM. There are three generations of (s)quarks and (s)leptons: q $= u$, c, t and b $= d$, s, b; $\nu = \nu_e$, ν_μ, ν_τ and l $= e$, μ, τ. The mass eigenstates of the EBHGHK bosons are more complicated due to SSB, and so are not listed in the table. They are h^0, H^0, A^0 and $H^\pm$ (the three remaining degrees of freedom are eaten by the electroweak gauge boson masses).

Supermultiplet	Name	Spin 1/2			Name	Spin 1		
		Gauge	Mass	P_R		Gauge	Mass	P_R
G	Gluino	$\tilde{g}$	$\tilde{g}$	-1	Gluon	g	g	$+1$
W	Wino	$\tilde{W}^1$	$\tilde{\chi}_1^+, \tilde{\chi}_2^+$	-1	W	W^1	W^+	$+1$
		$\tilde{W}^2$	$\tilde{\chi}_1^-, \tilde{\chi}_2^-$	-1		W^2	W^-	$+1$
		$\tilde{W}^3$	$\tilde{\chi}_1^0, \tilde{\chi}_2^0$	-1		W^3	Z^0	$+1$
B	Bino	$\tilde{B}^0$	$\tilde{\chi}_3^0, \tilde{\chi}_4^0$	-1	Z, A	B^0	A^0	$+1$

(b) The vector supermultiplets of the MSSM. Note that the eight mass eigenstates of the electroweak bosoninos contain the four weak EBHGHKino eigenstates from Table 2.2a, $\tilde{H}_\uparrow^+$, $\tilde{H}_\downarrow^-$, $\tilde{H}_\uparrow^0$, $\tilde{H}_\downarrow^0$, such that the degrees of freedom correspond. These mass eigenstates are known as the *charginos* and *neutralinos*. Note also that these take the place of the zino and photino that one would expect in an unbroken supersymmetry.

Table 2.2: A summary of the MSSM field content.

mass in the Standard Model. It should be noted that the colour, isospin and family indices have been suppressed for the sake of clarity.

Finally, it is worth noting that it is possible to write down additional terms in the superpotential that are gauge invariant and analytic that could be included as part of the MSSM superpotential, such as

$$W_{\Delta L=1} \;=\; \frac{1}{2}\,\lambda^{rst}\,L_r\,L_s\,\bar{l}_t + \lambda'^{\,rst}\,L_r\,Q_s\,\bar{d}_t + \mu''^r\,L_r\,H_\uparrow \tag{2.33}$$

$$W_{\Delta B=1} \;=\; \frac{1}{2}\,\lambda''^{\,rst}\,\bar{q}_r\,\bar{d}_s\,\bar{d}_t, \tag{2.34}$$

where the generation indices r, s, $t = 1$, 2, 3 have been restored. These terms are problematic in the sense that Eq. 2.33 violates lepton number L, and Eq. 2.34 violates baryon number B; such interactions have not been observed experimentally. It is therefore helpful to define the ever so gently *ad hoc* symmetry "*R*-parity conservation" [52, 53], with the multiplicative quantum number

$$P_R = (-1)^{\,3\,(B-L)+2S}, \tag{2.35}$$

where S is the spin of the (s)particle. By requiring that all MSSM interaction terms respect $P_R = +1$, terms such as those in Eq. 2.33 and 2.34 may be discarded. *R*-parity conservation has the phenomenological benefits of ensuring sparticles are produced in pairs and always decay to what is, by definition, the Lightest Supersymmetric Particle (LSP) – the Cold Dark Matter (CDM) candidate mentioned in § 2.2.3.

The MSSM defined according to this procedure has an additional 105 parameters appearing in the Lagrangian. This is not presented here, not only for the sake of brevity, but also because many of the MSSM sparticles listed in Tables 2.2a and 2.2b are not those that would be produced at LHC energies. In order to understand how supersymmetry behaves at the electroweak scale – and so engineer the mass differences that *must* exist if supersymmetry is a useful description of Nature – supersymmetry must be broken. This is the subject of the next subsection.

2.3.2   Gravity-mediated supersymmetry breaking

Supersymmetry breaking is a wide-ranging and necessarily complex topic. The complexity revolves around the issue of breaking what is, in the MSSM at least, a global symmetry that changes the spin of a given field. Rather than give this issue the full mathematical treatment it deserves, the summary presented here will unashamedly focus on one particular supersymmetry breaking mechanism used by one particularly popular model – Planck-scale mediated supersymmetry, formulated as either the Constrained Minimally Supersymmetric Standard Model (CMSSM) or the (related) Minimal Supergravity (MSUGRA)[14].

The reasoning behind this is that supergravity localises the supersymmetric transformations from the outset, putting them on an equal footing with the other gauge symmetries of the Standard Model. The spin 3/2 gravitino required by this localisation[15] provides a useful way of thinking about the additional VEV that one would expect from an additional instance of SSB. In the case of the CMSSM, the VEV is traded for the gravitino mass $M_{3/2}$, such that

$$M_{3/2} \sim \frac{\langle F \rangle}{M_P}, \tag{2.36}$$

where $\langle F \rangle$ is the VEV associated with one of the chiral supermultiplet's auxiliary complex scalar fields, F (see Equation 2.30) and $M_P \equiv \sqrt{\hbar c / G_N} \sim 10^{19}\,\mathrm{GeV}$ is the Planck Mass. The SSB occurs in the gravity-scale sector via non-renormalisable terms such as

$$
\begin{aligned}
\mathcal{L}_{\mathrm{NR}} &= -\frac{1}{M_P} F \left(\frac{1}{2} f_a \, \tilde{\lambda}^a \, \tilde{\lambda}^a + \frac{1}{6} y'^{\,uvw} \, \tilde{\phi}_u \, \tilde{\phi}_v \, \tilde{\phi}_w + \frac{1}{2} \mu'^{\,uv} \, \tilde{\phi}_u \, \tilde{\phi}_v \right) + \mathrm{c.c.} \\
&\quad - \frac{1}{M_P^2} F F^* k_v^u \, \tilde{\phi}_u \, \tilde{\phi}^{*\,v}.
\end{aligned}
\tag{2.37}
$$

---

[14] An example of an alternative mechanism is Gauge-Mediated Supersymmetry Breaking (GMSB) [54, 55, 56]; see [57] for a review.

[15] See § 6.1 of [44] for a more detailed discussion.

These non-renormalisable terms are suppressed by the $1/M_P$ factor such that the model becomes renormalisable at the electroweak scale. (This is what is meant by an *effective theory*.)

The form of these terms has, of course, been chosen such that when the supersymmetry is broken and the F terms in Eq. 2.37 are replaced by the gravitino VEV with $\langle F \rangle \sim 10^{10}$ GeV, terms consistent with a renormalisable "soft" supersymmetry breaking scheme remain:

$$
\begin{aligned}
\mathcal{L}_{\text{soft}} \;=\; &-\left(\frac{1}{2} M_a \, \tilde{\lambda}^a \, \tilde{\lambda}^a + \frac{1}{6} \, y^{uvw} \, \tilde{\phi}_u \, \tilde{\phi}_v \, \tilde{\phi}_w + \frac{1}{2} \, \mu^{uv} \, \tilde{\phi}_u \, \tilde{\phi}_v \right) + \text{c.c.} \\
&- (M^2)^u_v \, \tilde{\phi}_u \, \tilde{\phi}^{*\,v}.
\end{aligned} \tag{2.38}
$$

noting (in order) the gaugino mass terms, the trilinear scalar coupling terms, the bilinear scalar coupling terms, and the scalar mass terms [58]. As with the Standard Model, the process of symmetry breaking introduces additional free parameters to the model. To considerably simplify this situation, the CMSSM makes the following assertions:

- There is a common coupling for the three gauginos, i.e. $f_a \equiv f$. A common gaugino mass term is then defined as

$$
f_a \, \frac{\langle F \rangle}{M_P} \to f \, \frac{\langle F \rangle}{M_P} \equiv M_{1/2} = M_a; \tag{2.39}
$$

- The M_P-scale scalar mass terms are all set to the same value and the mass matrices are diagonal, such that $k^u_v \equiv k \, \delta^u_v$. This means that, before running down to the electroweak scale, the masses of squarks, sleptons and EBHGHK scalars are all M_0:

$$
k^u_v \, \frac{|\langle F \rangle|^2}{M_P} \to k \, \delta^u_v \, \frac{|\langle F \rangle|^2}{M_P} \equiv M_0^2 \, \delta^u_v = (M^2)^u_v; \tag{2.40}
$$

- The remaining couplings are then defined to be proportional to the corresponding superpotential parameters: $y'^{uvw} \equiv \alpha\, y^{uvw}$ and $\mu'^{uv} \equiv \beta\, \mu^{uv}$ where α and β are dimensionless constants, such that

$$y'^{uvw} \frac{\langle F \rangle}{M_P} \rightarrow \alpha\, y^{uvw} \frac{\langle F \rangle}{M_P} = A_0\, y^{uvw}, \quad \mu'^{uv} \frac{\langle F \rangle}{M_P} \rightarrow \beta\, \mu^{uv} \frac{\langle F \rangle}{M_P} = B_0\, \mu^{uv}.$$
(2.41)

The mapping from the non-renormalisable supersymmetry-breaking Lagrangian terms of the CMSSM to those of the MSSM is achieved with the introduction of three parameters M_0, $M_{1/2}$, and A_0. (The B_0 term of Equation 2.41 is set, somewhat arbitrarily, to $B_0 = A_0 - M_0$.) The story does not end there, however; the terms of 2.38 are defined at the unification scale and must be "run down" to the electroweak scale using the Renormalisation Group Equations (RGEs).

This is fortunate for the breaking of the $SU(2)_L \times U(1)_Y$ symmetry in the MSSM, which is complicated by the inclusion of a second EBHGHK doublet. A common scalar mass (Eq. 2.40) would otherwise result in one of the two EBHGHK VEVs being zero, leading to massless up- or down-type quarks and leptons. It is necessary, therefore, to define the parameter[16] β where

$$\tan \beta \equiv \frac{v_\uparrow}{v_\downarrow} = \frac{\langle H_\uparrow^0 \rangle}{\langle H_\downarrow^0 \rangle}.$$
(2.42)

The required difference between $v_\uparrow$ and $v_\downarrow$ is due to radiative corrections from the heavy quarks; thus SSB in the MSSM is often referred to as *radiative electroweak symmetry breaking* [59, 60]. Once a value for $\tan \beta$ is chosen, the magnitude of μ in the superpotential (Equation 2.32) is fixed by Standard Model parameters, since

$$\frac{1}{2} M_Z^2 = \frac{1}{8} \left(g^2 + g'^2 \right) v^2 = \frac{1}{4} \left(g^2 + g'^2 \right) \left(v_\downarrow^2 + v_\uparrow^2 \right)$$
(2.43)

$$= \frac{M_{H_\uparrow^0}^2 - M_{H_\downarrow^0}^2 \tan \beta}{\tan^2 \beta - 1} - |\mu|^2,$$
(2.44)

---

[16] β may be thought of as a mixing angle between the eigenstates of the charged EBHGHK fields and charged electroweak gauge fields.

where $M_{H_\downarrow^0}$ and $M_{H_\uparrow^0}$ are the mass terms of the EBHGHK potential at the electroweak scale[17]. Thus the CMSSM requires five parameters in addition to the nineteen of the Standard Model:

$$M_0, \ M_{1/2}, \ A_0, \ \tan\beta, \ \text{and sign} \ |\mu|. \tag{2.45}$$

This simplification scheme significantly reduces the parameter space to be explored in a way that allows experimental predictions to be made. How these predictions are probed by the experimentalist is the subject of the next subsection.

2.3.3 Signatures of supergravity

The Constrained Minimally Supersymmetric Standard Model (CMSSM) has offered a mechanism for the breaking of a postulated supersymmetry at an energy scale in the region of the Planck mass. As inputs to the RGEs, the GUT-scale coupling and mass terms of a given model will set the masses, decay modes, branching fractions, and production cross-sections at the electroweak scale – i.e. the properties that determine the experimental signature. Setting these to a few common values not only adheres to the conceptually pleasing philosophy of unification, but also vastly reduces the possible parameter space that has to be probed by a given experiment.

Even then, however, the observer hoping to establish what might be observable in a particular detector faces an unmanageable number of possibilities; scanning a five dimensional parameter space is unfeasible. Thus it is standard practice to consider a number of "benchmark" scenarios where fixed points in the parameter space are chosen [61]. A selection of the Low Mass (LM) signal points used by the CMS collaboration's supersymmetry searches are listed in 2.3 for convenience [18, 62].

As noted previously, the parameters of Eq. 2.45 do not correspond to the masses and couplings of the sparticles at the electroweak scale. To obtain these, the model

---

[17] The reader is referred to § 6.1 of [44] for a discussion of the radiative breaking of the $SU(2)_L \times U(1)_Y$ symmetry in the CMSSM.

Point	$M_0/$GeV	$M_{1/2}/$GeV	$A_0/$GeV	$\tan\beta$	sign $|\mu|$
LM0	200	160	-400	10	$+$
LM1	60	250	0	10	$+$
LM2	185	350	0	35	$+$
LM3	330	240	0	20	$+$
LM4	210	285	0	10	$+$
LM5	230	360	0	10	$+$

Table 2.3: Parameter values for a selection of the benchmark CMSSM points [18, 62].

builder must use the Renormalisation Group Equations (RGEs) of the MSUGRA model [60]. These equations, generally expressed as a function of $t \equiv \ln(Q/Q_0)$, describe how the masses and couplings evolve as Q, the renormalisation scale[18], is lowered from the GUT-scale to the electroweak scale. Fortunately, tools exist that automatically calculate the sparticle mass spectra and couplings for a given set of input parameters using the RGEs; SOFTSUSY [63] is such a tool. Figure 2.2 shows the sparticle mass spectra for benchmark points LM0 and LM1.

(a) LM0.   (b) LM1.
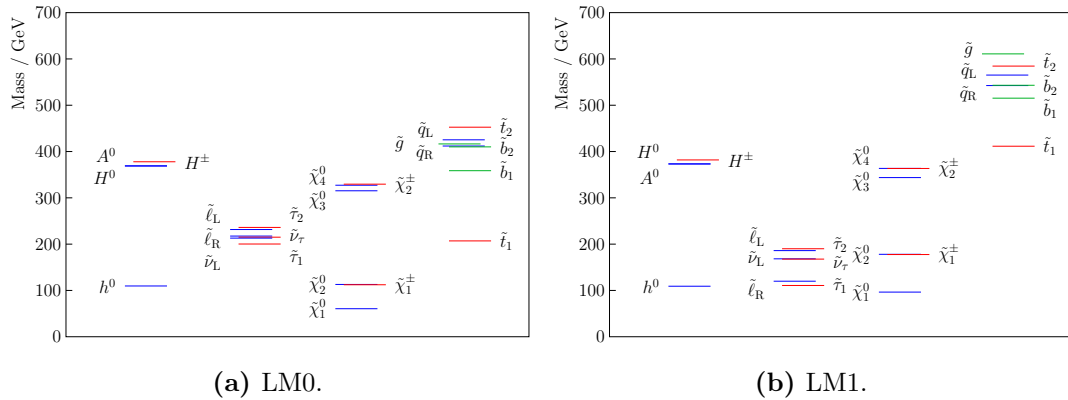
Figure 2.2: Sparticle mass spectra for two of the CMSSM benchmark points.

Once the mass spectrum and couplings have been calculated for a given model, there are three major issues for the model builder to consider:

- **Sparticle production cross-sections**: One of the many strategies deployed in order to obtain evidence of supersymmetry in Nature is to produce sparticles

---

[18] A convenient summary of the CMSSM RGEs may be found in Appendix E of [44].

in high energy particle collisions. At the LHC, protons are collided at a centre of mass energy of 7 TeV. If a given $q\bar{q}$, qg or gg hard-scatter interaction is energetic enough sparticles may be produced. If R-parity holds, sparticles must be produced in pairs; thus $E_{\mathrm{CoM}} > 2\,M_{\mathrm{LSP}}$. The masses and couplings may be used to predict production cross sections for a given centre of mass energy.

- **The Lightest Supersymmetric Particle (LSP)**: If R-parity holds, any sparticle produced in an initial collision must decay into a stable Lightest Supersymmetric Particle (LSP); thus an even number of at least two LSPs should be present in the final state of a supersymmetric collision. Assuming the LSP interacts only via the weak force or gravity, they will generally carry energy away from the collision in a manner unobservable to standard detector instrumentation. The missing energy signature is therefore an important tool in the search for supersymmetry.

- **Sparticle decays**: The decay chain from the initially produced sparticle to the LSP will depend largely on the sparticle mass spectrum, in terms of what is kinematically allowed. The specifics of these chains are somewhat involved but they will ultimately determine the event topology (i.e. the Standard Model particles accompanying the LSPs in the final state) and the kinematic characteristics of the event.

Given all of these factors, the question of how supersymmetric particles may appear in LHC collisions is well specified – at least for the CMSSM model. It should be made clear, however, that supersymmetry as it stands very much remains in the model-building phase; the Lagrangian is still under construction. The sparticle hunter must adopt a trial-and-error approach to experimentally testing whether a given supersymmetric model represents Nature. The parameters of the CMSSM

must be set to values that allow the production of sparticles in $7\,\mathrm{TeV}$ proton-proton collisions. The search strategy must then find a way of identifying these events and distinguishing them from events that are due to processes described by the "old" physics. If experimental measurements are inconsistent with the signal predicted by a given set of parameter values, one must conclude that either the actual parameters are unobtainable by experiment – making the model effectively untestable – or that the model itself is wrong. This is a conceptually different problem to measuring the actual parameter values, or testing the consistency of a model; this can be attempted only upon finding *any* evidence in favour of a supersymmetric description of Nature.

Chapter 3

Event Kinematics and Robustness

"It is one thing to show a man that he is in error, and another to put

him in possession of truth."

John Locke, *An Essay concerning Human Understanding (1690)*

Having discussed the theoretical and phenomenological aspects of supersymmetry, the discussion returns to how it may be discovered experimentally. As mentioned in the introduction, the simplest signal topology contains only jets in the final state. The removal of events featuring charged leptons reduces the number of backgrounds with real missing transverse momentum, since many of these are due to processes involving W production and decay (including top quark events). To complicate matters, as was also noted in the introduction, the all-hadronic channel is subject to an additional class of background event. Purely QCD-like events share a similar topology, although the lack of one or more isolated invisible particles in the final state should mean that the measured missing transverse momentum is negligible[1].

---

[1] Jets featuring a b-quark may result in the production of a neutrino and hence real missing transverse momentum. However, the associated lepton production and probable alignment of the neutrino momentum with the parent jet help mitigate for this outcome. The interested reader is referred to [64], where the all-hadronic search described here was performed utilising the b-tagging capabilities of the CMS experiment.

Unfortunately, the measurement of the particle energies, and so the inferred missing transverse momentum, depends on the performance of the individual detector subsystems. While large errors should be rare in a well-designed detector, the overwhelming cross-section of QCD events means that the contribution from these events to the signal region is potentially significant. A full discussion of the instrumental sources of missing transverse momentum is postponed until Chapter 4, where the CMS detector subsystems are described in more detail. This chapter describes the method used to suppress mismeasurement-induced backgrounds through the exploitation of event kinematics in a highly idealised, calorimeter-like measurement system.

Firstly, the principles underpinning the method – the decomposition of the momentum measurement into an azimuthal angle and a (transverse) energy measurement, and the construction of observables that exploit this decomposition – are described. Then a toy analysis, using a simplified measurement system where the errors in each of these components can be carefully controlled to illustrate these principles, is performed. The *a priori* robustness of the method is then demonstrated.

3.1 Event kinematics

3.1.1 Decoding the calorimeter output

The collimated jets of particles produced by the hadronisation of partons emergent from the initial collision are typically measured by recording the energy they deposit in the sensitive regions of the calorimeters[2]. In a perfect measurement system, a particle incident upon a sensitive region stops and deposits all of its energy, E_i, into the cell. The measured energy E_i is associated with a position in space determined

---

[2] Additional information about the charged particle component of a jet can be obtained from the tracking systems; this is neglected for now.

by the location and geometry of the detector cell i that measured it. This position is the centre of the cell surface and the associated uncertainty is a function of the shape of the cell. In order to obtain an estimate of the momentum of a particle[3] thought to correspond to a given energy deposit, the observer must make the following assumptions:

- Each cell corresponds to a single particle with 4-momentum P_i^{μ};

- The particles are massless, i.e. $|P^{\mu}| = E$ and $P^{\mu}P_{\mu} = 0$;

- The particles emerge from the origin, and so $(\hat{\mathbf{P}} \pm \sigma_{\hat{\mathbf{P}}}) \equiv (\hat{\mathbf{R}} \pm \sigma_{\hat{\mathbf{R}}})$, i.e. the direction of a given particle is determined by the position $\mathbf{R}$ and spatial extension $\boldsymbol{\sigma_R}$ of the corresponding detector cell. The expressions for the 3-momenta components and their uncertainties are presented in Appendix A.

These assumptions introduce discrepancies between what is measured and what actually happened. For example, the momentum of massive particles is systematically overestimated, since $\mathbf{P}^2 = E^2 - M^2$. The combined momentum of two or more particles incident on the same cell will also be systematically overestimated. This is because in the two particle case, the assumptions made result in $|\mathbf{P}_{\mathrm{cell}}| = E_a + E_b$, whereas the "true" momentum is

$$|\mathbf{P}_{ab}| \equiv |\mathbf{P}_a + \mathbf{P}_b| = \sqrt{(E_a + E_b)^2 - M_{ab}^2}, \tag{3.1}$$

where M_{ab} is invariant mass of the two-particle system, given by

$$M_{ab}^2 = M_a^2 + M_b^2 + 2e_a e_b \left(\cosh \Delta y_{ab} - \beta_{Ta}\beta_{Tb} \cos \Delta\phi_{ab}\right), \tag{3.2}$$

where e_a is the transverse energy of particle a, Δy_{ab} is the difference in rapidity between particles a and b, $\beta_{Ta} \equiv p_a/E_a$ is the transverse boost of particle a, and

---

[3] A calorimeter cannot make a direct measurement of the momentum of a particle. An estimate of, say, the transverse momentum would be possible with a tracker and a magnetic field. A Čerenkov detector would provide a measurement of $\beta = v/c$.

$\Delta\phi_{ab}$ is the difference in azimuthal angle between particles a and b[4]. Of course, the contribution of these assumption-based errors to the uncertainty on the overall measurement may be deemed neglible given the resolution of the calorimeter. In any case, the reasoning behind such decisions and the assumptions upon which they are made should be made explicit[5].

Having decided upon how the estimates of the collision product momenta may be extracted from the energy deposits, the observer can now combine these measurements in order to calculate whole-event variables such as the total energy, ΣE, or the total momentum, $\Sigma \mathbf{P}$. The typical *recombination scheme* is 4-vector addition of the 4-momenta associated with each cell:

$$E_{ij} = E_i + E_j \tag{3.3}$$

$$p_{x\,ij} = p_{xi} + p_{xj} \tag{3.4}$$

$$p_{y\,ij} = p_{yi} + p_{yj} \tag{3.5}$$

$$q_{ij} = q_i + q_j, \tag{3.6}$$

where q is the longitudinal momentum component. This is known as the "E scheme" in the literature[6]. It is implicit in the definition of this scheme that the uncertainties are added in quadrature.

3.1.2 Missing transverse momentum

One may now turn to the issue of invisible particles, which is particularly relevant when considering R-parity conserving supersymmetry models. Firstly, one should note that the property of "invisibility" is not an intrinsic property of a particle itself; rather, it depends upon how the particle is defined to interact with the sensitive

---

[4] See Appendix A for further definitions, or [65] for an excellent treatment of these variables.
[5] For example, errors are introduced if the particles emerge from a point other than the origin.
[6] See §2.4 of [66] for a discussion of this and other recombination schemes.

regions of the measurement system. Thus the first step to take in accounting for the invisible particles is to redefine the measurement system interactions as follows:

- When a "visible" particle is incident upon the detector, it stops and deposits all of its energy. Expressing this mathematically, the corresponding probability density functions for the energy transferred $E_{\text{trans.}}$ from a visible particle of incident energy $E_{\text{inc.}}$ are

$$f\left(E_{\text{trans.}} \mid E_{\text{inc.}}\right) \text{d}\, E_{\text{trans.}} = \delta\left(E_{\text{trans.}} - E_{\text{inc.}}\right) \text{d}\, E_{\text{trans.}}. \tag{3.7}$$

- When an "invisible" particle is incident upon the detector, it passes through with no interaction. The corresponding *pdf* for any $E_{\text{inc.}}$ a delta function centred at zero, i.e.

$$\tilde{f}\left(E_{\text{trans.}} \mid E_{\text{inc.}}\right) \text{d}\, E_{\text{trans.}} = \delta\left(E_{\text{trans.}}\right) \text{d}\, E_{\text{trans.}}. \tag{3.8}$$

For now, "invisible" particles are taken to be all flavours of standard model neutrino and all of the (hypothetical) neutral sparticles. It is noted that this model does not take into account realistic detector effects like the different responses of charged and neutral particles in different calorimeter materials or muon punch-through.

One can now define the observed missing energy $\not{E}_{\text{obs.}} \equiv \sqrt{s} - \Sigma E$ and observed missing momentum $\not{\mathbf{P}}_{\text{obs.}} \equiv \mathbf{P}_{\text{init.}} - \Sigma \mathbf{P}$, where $\sqrt{s}$ is the centre-of-mass energy in the laboratory frame and $\mathbf{P}_{\text{init.}}$ is the sum of the 3-momenta of the initial state particles (generally assumed to be $\mathbf{0}\,\text{GeV}$[7]). It is noted that:

- Any energy lost due to invisible particles reduces the energy that can potentially be measured in a given collision (assuming $\sqrt{s}$ is fixed). Thus events involving the production of invisible particles will have a smaller overall energy scale. This effect is more pronounced if the invisible particles are massive;

---

[7] Natural units are used throughout the work presented here.

- Missing energy and momentum can only be defined in terms of what the observer knows about the initial conditions of the collision and *everything else* that is measured by the measurement system. In other words, the "missing" quantities are a function of the *entire measurement system.* This is why such measurements are among some of the most difficult to perform in high energy physics: the observer must have a thorough understanding of the entire apparatus, the output it produces and the way in which this output is interpreted in order to draw meaningful conclusions about objects that, by definition, she cannot measure directly;

- If two or more particles go undetected (for whatever reason), the observer has irretrievably lost information about what has taken place in the event. To see this, consider an event with $[\not{P}^\mu] = (\not{E}_{\text{real}}, \not{\boldsymbol{P}}_{\text{real}})$. It is impossible for the observer to determine whether this is due to one invisible particle of mass $M = \not{P}^\mu \not{P}_\mu$, or whether an "effective mass" was generated by two (or more) invisible particles (see Equation 3.2 for the two particle case).

These difficulties have led experimental physicists working with hadron collisions to adopt strategies that do not necessarily depend on the total missing energy and momentum. One such approach invokes the assumption that, even in hadronic collisions, momentum should be conserved in the transverse $(x - y)$ plane as defined relative to the beam (z) axis. One may therefore consider the component of a given collision product's momentum perpendicular to the beamline as a useful observable. This is defined to be $[\mathbf{p}] = (p_x, p_y)$, with the magnitude given by

$$p \equiv |\mathbf{p}| \equiv |\mathbf{P}| \sin \theta = \sqrt{p_x^2 + p_y^2}, \tag{3.9}$$

where θ is the polar production angle relative to the beam axis[8].

---

[8]Note that the convention of using lower-case roman letters for transverse quantities has been adopted, as in [67]. The exception is $q \equiv p_z$, which is a purely longitudinal quantity.

The *missing transverse momentum* of the event is then defined as

$$\not{p} \equiv -\Sigma p \equiv -\sum_i^N \mathbf{p}_i, \tag{3.10}$$

where the $\mathbf{p}_i$ are the transverse momenta of each of the N objects measured in the collision event. Perhaps the most famous use of the missing transverse momentum was in the discovery of W boson at the CERN Super Proton Synchrotron (SPS) $p\bar{p}$ collider, reported in [68]. Events that contained a large transverse energy electron, a large missing transverse energy, and no other significant detector activity were selected from the collision data on the basis that this would be the expected experimental signature of a W^- (W^+) which subsequently decayed into an electron (a positron) and an antineutrino (a neutrino).

As discussed, measurements of the missing longitudinal momentum are unreliable, and so a direct estimation of M_W was not possible. However, it was noted that if $\not{p}$ was taken to be the transverse momentum of the (anti)neutrino $\mathbf{p}_\nu$, then the *transverse mass* $m \left(\equiv M_T \right)$ of the $e^\pm \nu$ system,

$$m^2 \quad \equiv \quad \left(\sum_i e_i \right)^2 - \left(\sum_i \mathbf{p}_i \right)^2 \tag{3.11}$$

$$\Rightarrow m_{e\nu}^2 \quad = \quad (e_e + e_\nu)^2 - (\mathbf{p}_e + \mathbf{p}_\nu)^2 \tag{3.12}$$

$$\approx \quad 2\, p_e \, p_\nu \, (1 - \cos \Delta\phi_{e\,\nu}) \tag{3.13}$$

(where $\Delta\phi_{e\,\nu}$ is the azimuthal angle between the electron and the neutrino and the approximation holds if both particles are assumed to be massless), could be used to place an upper bound on M_W since, as shown in [69], $0 \geq m_{e\,\nu} \geq M_W$. An estimate of M_W was thus obtained from the endpoint of the m_W distribution.

In this particular search for supersymmetry an accompanying charged lepton is explicitly forbidden in order to suppress this class of SM background. As discussed, of greater concern to the all-hadronic topology are events that produce a large measured missing transverse momentum due to imperfections in the measurement system. These are the subject of the following subsection.

3.1.3 Accounting for detector mismeasurements

The detector used to measure the energy of a given particle, and so estimate the magnitude of its momentum, has been modelled as a perfect calorimeter thus far; that is to say all of the particle's energy is transferred to the detector material and is accurately recorded by the measurement system. This is very much an idealisation; the actual energy transferred to the calorimeter material, and then recorded by the detector output, is strongly dependent on the calorimeter design and generally requires sophisticated modelling with simulations like `GEANT4` [70].

A more realistic model of a calorimeter cell models the energy response as a Gaussian distribution which, for a given incident energy $E_{\text{inc.}}$, has a width σ_E given by

$$\frac{\sigma_E}{E_{\text{inc.}}} = \frac{\kappa}{\sqrt{E_{\text{inc.}}}} \oplus \frac{\nu}{E_{\text{inc.}}} \oplus \zeta, \tag{3.14}$$

where $\oplus$ denotes addition in quadrature, κ is a *stochastic* term that accounts for the showering and sampling processes that take place in the calorimeter material, ν is a *noise* term that models the effect of electronics noise on the detector output, and ζ is a constant term. Ignoring any tails in the distribution of the calorimeter response, the energy resolution of the calorimeter cells can then be modelled by randomly selecting the transferred energy $E_{\text{trans.}}$ from the distribution

$$f\left(E_{\text{trans.}} \mid E_{\text{inc.}}\right) \mathrm{d}\, E_{\text{trans.}} = A \exp\left(-\frac{(E_{\text{trans.}} - E_{\text{inc.}})^2}{2\,\sigma_E^2}\right) \mathrm{d}\, E_{\text{trans.}}, \tag{3.15}$$

where A is some normalisation constant[9]. Estimates of the actual values of κ, ν and ζ for a given calorimeter may be extracted from test beam data with individual calorimeter cells, but some uncertainty will always remain until the fully constructed detetector can be tested *in situ*. Typical values for κ are $0.05\,\text{GeV}^{1/2}$ for electromagnetic calorimeters and $1.5\,\text{GeV}^{1/2}$ for hadronic calorimeters, though these are very

---

[9] The non-gaussian nature of jet energy measurements is discussed further in Chapter 4.

dependent on the materials used and configuration of the materials. CMS reports $0.02\,\mathrm{GeV}^{1/2}$ and $0.7\,\mathrm{GeV}^{1/2}$ respectively in the barrel regions [71].

The problem is that an energy fluctuation of the type described by Equation 3.15 changes the magnitude of the transverse momentum vector $\mathbf{p}_i$ used in the calculation of $\not{p}$. The difference is referred to as "fake" missing transverse momentum and it is this that is responsible for the contributions to the signal region from QCD-like events in this particular search.

To suppress this background, the ability to determine whether or not the observed $\not{p}$ was due to one or more invisible particles or a mismeasurement would be useful. Events that were flagged as being of the latter type could then be discarded from the analysis. In fact, such clues can be extracted from an examination of the event kinematics; to see how one may consider the two-body, or dijet, system.

As is often the case in physics, the simplicity of the two-body system aids the analysis and interpretation of the more general scenario. For example, with the dijet system it is trivial to define the following quantities:

$$\Delta e \;=\; e_1 - e_2 \tag{3.16}$$

$$\Delta \phi \;=\; |\phi_1 - \phi_2|, \quad \Delta\phi \in [0,\,\pi) \tag{3.17}$$

$$\Delta \eta \;=\; |\eta_1 - \eta_2|, \tag{3.18}$$

where the two (massless) particles are ordered by transverse energy, which is defined as the energy of the particle in the frame where its longitudinal momentum is zero, i.e.

$$e\,(\equiv E_T) \equiv \sqrt{E^2 - q^2} = \sqrt{M^2 + |\mathbf{p}|^2} = E\operatorname{sech} y = E\operatorname{sech} \eta \tag{3.19}$$

where y is the particle rapidity (see Eq. A.4, Appendix A), and the last equality only holds for massless particles. The transverse energy of a cell may be thought of as a way of "weighting" the energy deposited in the cell by the cell's longitudinal

position. $\Delta\phi$ and $\Delta\eta$ tell the observer about the spatial separation of the particles as recorded by the detector. Δe informs the observer about how the total transverse energy Σe is distributed between the two particles.

Why might this information be useful? Consider a dijet event for which transverse momentum is largely conserved in the transverse plane (i.e. there are no invisible collision products removing a significant fraction of the transverse energy). For such "back-to-back" events, $\not{p} = \mathbf{0}$: the cluster momenta cancel each other out. The missing transverse momentum may be expressed in terms of Σe, Δe and $\Delta\phi$ as follows:

$$|\not{p}| = \Sigma e \left[\cos^2\left(\tfrac{\Delta\phi}{2}\right) + \left(\tfrac{\Delta e}{\Sigma e}\right)^2 \sin^2\left(\tfrac{\Delta\phi}{2}\right) \right]^{\frac{1}{2}}. \tag{3.20}$$

As the phrase "back-to-back" suggests, $\not{p} = 0$ if $\Delta e = 0$ and $\Delta\phi = \pi$. Otherwise $\not{p} > 0$, which is the canonical indication that an additional, invisible particle has disappeared. Yet the breakdown into Δe and $\Delta\phi$ allows the observer to identify which aspect of the measurement has lead to a non-zero missing transverse momentum. For example, a dijet event with $\Delta\phi \sim \pi$ and a large Δe is suggestive of a back-to-back event where one or both of the collision product energies have been mismeasured; and while $\not{p}$ may still be large, the event is unlikely to be interesting from a supersymmetry perspective. Conversely, an event with $\Delta\phi < \pi$ is likely to have featured one or more invisible collision products in the final state.

The interesting point to note is that these two observables have separated the $\not{p}$ information into two elements – the *angular* information and the *transverse energy* information[10]. Having decomposed the event's $\not{p}$ into these two elements, if the observer *knows a priori* that one is more reliable than the other – for example, if the energy resolution is either poor or unknown, but the angular resolution is good or well-understood – she can choose a search strategy that reflects this.

---

[10] An equivalent way of thinking about the situation is that $\not{p}$ compresses the angular and transverse energy information into a single variable.

This approach was inspired by a survey of the long history of collider-based dijet studies. For example, in [7], Randall and Tucker-Smith defined the observable

$$\alpha = \frac{E_{T\,j2}}{M} \equiv \frac{e_2}{M},\tag{3.21}$$

where $E_{T\,j2} \equiv e_2$ is the transverse energy of the second jet (ordered by e) and M is the invariant mass of the dijet system. This was found to be a useful tool for distinguishing between signal and background as the α distribution was found to have an "edge" at around $\alpha = 0.5$ for QCD-like backgrounds, but a tail that leaked over this edge from real missing energy signals. The α variable inspired the study carried out in [72] and reported to the wider community in [73], which actually used the discriminating variable

$$\alpha_T = \frac{E_{T\,j2}}{M_T} \equiv \frac{e_2}{m},\tag{3.22}$$

where m ($\equiv M_T$) is the *transverse mass* defined in Equation 3.11 (as opposed to the invariant mass M). This study found the edge displayed at $\alpha_T = 0.5$ to be even more pronounced for QCD-like backgrounds. The location of the edge is simple to explain; for a conserved ($\not{p} = 0$) dijet event,

$$e_2 = e_1 = \frac{1}{2}\,\Sigma e \quad \text{and} \quad m = \Sigma e.\tag{3.23}$$

The powerful rejection of QCD-like backgrounds made α_T a suitable observable for early supersymmetry searches. However, as far as the author is aware, no explanation was given in any of the above studies as to *why* either α or α_T rejected conserved backgrounds so effectively. Only in [74] was it noted that

$$e_2 = \frac{1}{2}\,(\Sigma h - \Delta h)\tag{3.24}$$

$$\Rightarrow \alpha_T = \frac{1}{2}\frac{(\Sigma h - \Delta h)}{\sqrt{\Sigma h^2 - \not{h}^2}}\tag{3.25}$$

$$= \frac{1}{2}\frac{1 - \frac{\Delta h}{\Sigma h}}{\sqrt{1 - \left(\frac{\not{h}}{\Sigma h}\right)^2}},\tag{3.26}$$

where the h notation is used to indicate that the jet transverse energies have been used in the calculations. By using the transverse energy of the second jet in the numerator, α_T is implicitly using the imbalance in the measured transverse energy to compensate for any fake missing transverse momentum that might appear in the denominator. If the fake missing transverse momentum is due to a mismeasurement of the energy of the clusters, both Δh and $\not{h}$ will be large and α_T is pulled below the 0.5 edge.

If, however, a real invisible particle is responsible for a large $\not{h}$ value (i.e. $\Delta\phi$ is small), the denominator becomes smaller which pushes the α_T value above 0.5 edge. In this sense, α_T is *self-correcting* for mismeasurements of energy in the detector system, and this is made possible by the explicit separation of the angular and the energy measurement components in the discriminating observable, α_T.

The kinematic constraints imposed by requiring a dijet topology from the final state do not leave a lot of available phase space. This reduces the potential signal yield, which impacts on the observer's discovery prospects. The next logical step was to adapt the Δh, $\Delta\phi$ and α_T variables in such a way that the strategy may be applied to the multijet topology. Many of the initial attempts to do this focussed on constructing a dijet topology from the N particles reconstructed in the event. The kinematic properties of this pseudo-dijet system could then be used to calculate α_T as before. Such approaches make sense in the case of a $2 \to 2$ QCD process where one of the outgoing partons radiates a gluon to make a third object that could be recombined with its parent parton jet to recreate the original dijet system.

Unfortunately, this approach only solved the problem for the $M_{\text{cl.}} = 3$ case, where $M_{\text{cl.}}$ is the number of jets (clustered energy deposits – see § 3.2.2). A more fundamental flaw was that the recombination scheme typically used in forming the pseudo-jets – the E scheme of Equations 3.3 - 3.6 – necessarily results in a loss of

useful information, i.e. the individual angular and energy measurements associated with each particle. Not only is this disadvantageous in terms of retaining the information associated with the separated measurement elements, it also means that each of the different object combinations produces a different value for the transverse mass[11]. In order to keep the transverse mass $m\,(\equiv M_T)$ the same regardless of the combination chosen, the following recombination scheme must be used:

$$e_{ij} = e_i + e_j \tag{3.27}$$

$$p_{x\,ij} = p_{xi} + p_{xj} \tag{3.28}$$

$$p_{y\,ij} = p_{yi} + p_{yj} \tag{3.29}$$

$$q_{ij} = 0, \tag{3.30}$$

since the transverse mass of $M_{\text{cl.}}$ objects may be expressed as

$$m^2 = \left[\sum_{i=1}^{M_{\text{cl.}}} e_i\right]^2 - \left[\sum_{i=1}^{M_{\text{cl.}}} \mathbf{p}_i\right]^2. \tag{3.31}$$

This Transverse Object Merging (TOM) recombination scheme is the equivalent of adding together the lengths of the cluster $\mathbf{p}$ vectors in the transverse plane (which for massless objects is the same as the transverse energy e) and then pointing them in the direction of the vectorial sum of the $\mathbf{p}$ vectors. Crucially, the *energy measurement* information (i.e. the magnitude of the transverse energy) is not lost in the vectorial recombination of the objects. This information – including information about any mismeasurement of the energies – is retained in the transverse mass of the individual pseudo-jet, m_i.

The question remains of how to choose which combination of jets should form the pseudo-jets of the pseudo-dijet system. The numerator of α_T is suggestive of a strategy for choosing the most appropriate jet combination. It is noted that in the

---

[11] It was actually this observation that inspired the author to consider recombining the transverse energies of the clusters. To understand why different combinations produce different values of m, note that information is lost when the transverse energies are added together (Equation 3.11).

ideal QCD dijet case, where $\alpha_T = 0.5$, $\Delta h = 0$ and the jets are balanced in e. One may therefore consider *all* possible combinations of $M_{\text{cl.}} \to 2$ pseudo-jets A and B and select the one that minimises the imbalance, such that the quantity

$$\Delta h = \sum_{i \in A} |e_i| - \sum_{j \in B} |e_j| \tag{3.32}$$

is minimised[12]. Figure 3.1 shows, for example, how this transverse energy clustering mechanism picks out the most dijet-like combination for the perfectly measured three jet case where the possible combinations are $\{1, 23\}$, $\{2, 13\}$ and $\{3, 12\}$. Note that while for three jet systems, $\{1, 23\}$ (where the jets are ordered by E_T) will always pick out the smallest Δh, there is no such rule for $n \geq 4$. For example, there is no way to tell without performing the calculation whether $\{14, 23\}$ or $\{1, 234\}$ will yield the smaller Δh value. As such, all combinations must be considered in the general $M_{\text{cl.}}$-jet case. It is also noted that Δh will increase as the angles between the component jets of the pseudo-jet increase, and that Δh need not be zero for an $M_{\text{cl.}} > 2$ jet system, as even small opening angles between jets that are merged will produce a larger (and so imbalanced, compared to the other pseudo-jet) e_{ij}.
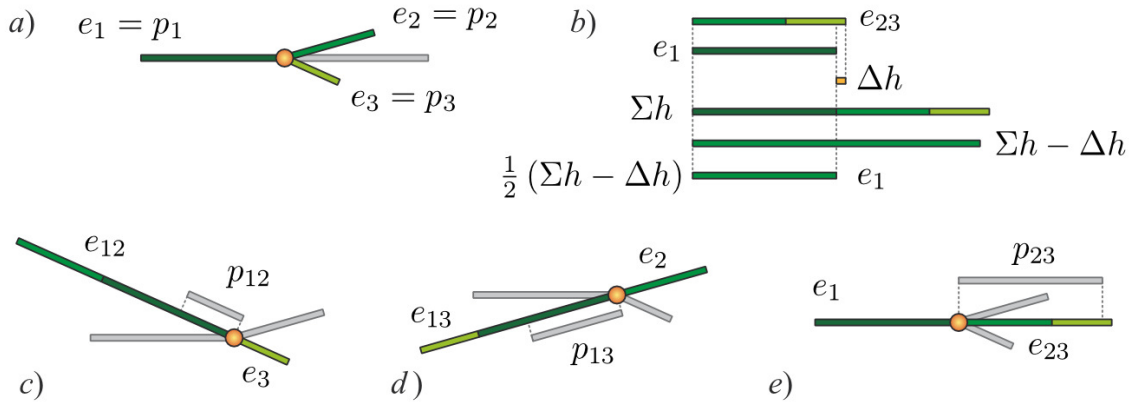
Figure 3.1: The Δh jet clustering method illustrated. a) A QCD-like three jet event as viewed in the transverse (x-y) plane. Note the original (balancing) jet indicated in grey; b) Calculation of the numerator of α_T using the minimum Δh, obtained from the most dijet-like combination $\{1, 23\}$; c) The $\{3, 12\}$ combination using the transverse energy merging scheme; d) The same for $\{2, 12\}$; e) The same for $\{1, 23\}$, the most dijet-like combination.

---

[12] With thanks to B. Allanach for the suggested multijet Δh notation [75].

A simpler way to think about Δh is as follows: if one were to try and place the transverse energies of the $M_{\mathrm{cl.}}$ clusters onto the two pans of a weighing scale, with each pan representing a pseudo-jet, Δh would be the difference in e of the most balanced combination. It is important here to once again emphasise the fact that this method of choosing the pseudo-jet components differs fundamentally from methods that use more traditional clustering algorithms, or tools like the transverse thrust axis of the $M_{\mathrm{cl.}}$ jets, in that it is based purely on transverse energy measurements and that *no angular information* is used whatsoever.

Substituting Equation 3.32 into Equation 3.22 extends the definition of α_T to the multijet system, and so it now becomes possible to use the α_T method on events with more than two objects in the final state. To demonstrate the workings of the method, the following section presents a toy analysis with a CMSSM signal and a QCD multijet background.

3.2 Demonstrating robustness with a toy analysis

3.2.1 Signals and backgrounds

The end of Chapter 2 saw the completion of the model-building process for a number of the Constrained Minimally Supersymmetric Standard Model (CMSSM) benchmark points; by choosing a point in a given parameter space, the Renormalisation Group Equations (RGEs) fix the masses, couplings and decay branching fractions at the electroweak scale. One may now consider how the sparticles might appear in high-energy proton-proton collisions, if at all. The approach here is to use computer simulations of the phenomena of interest to establish which sparticle production processes may occur, estimate the corresponding production cross-section, and predict what the resulting collision events might look like in the measurement system of choice so that they may be compared with the old physics backgrounds.

The 2010 LHC physics runs of relevance to the search described here took place at an energy of $3.5\,\mathrm{TeV}$ per proton beam; all physics simulations therefore use these initial beam conditions. The CTEQ6L1 Parton Density Function (PDF) [76] set is used to obtain the initial momenta of the incoming partons. The dominant sparticle production processes are listed in Table 3.1; ten thousand events were simulated for

Point	$M_{\tilde{g}}$	$\bar{M}_{\tilde{q}}$	$\tilde{g}\,\tilde{g}$	$\tilde{g}\,\tilde{q}$	$\tilde{q}\,\tilde{q}^{*}$	$\tilde{q}\,\tilde{q}$	Total
LM0	416.4	416.5	6.3	19.7	14.8	6.5	51.5
			(3.1)	(14.8)	(9.6)	(5.3)	(32.8)
			{3.1}	{15.3}	{9.7}	{5.8}	{33.8}
LM1	610.9	552.5	0.4	2.3	1.0	1.5	5.1
			(0.2)	(1.6)	(0.6)	(1.3)	(3.7)
			{0.2}	{1.6}	(0.6)	{1.4}	{3.8}

Table 3.1: Gluino masses, average squark masses (1ˢᵗ and 2ⁿᵈ gen.) and estimated production cross-sections of the benchmark points calculated at LO (NLO) with PROSPINO2, {LO} with Pythia 8.150. Masses are quoted in GeV, cross-sections in pb with $< 1\%$ error.

each benchmark point using the `Pythia 8.150` event generator [77][13] with the `4C` tuning [78, 79]. The quoted Leading Order (LO) and Next-to-Leading Order (NLO) cross-sections were calculated using `PROSPINO2` [80] and cross-referenced with the output from `Pythia 8`. No generator-level phase space cuts were imposed.

Simulated samples of multijet QCD events were produced in order to analyse the potential mismeasurement-induced background. While the problem of accurately modelling multijet QCD processes in $7\,\mathrm{TeV}$ proton collisions is one that is arguably far from solved[14], such simulations may still be useful in the *a priori* understanding of how a given detector may respond to multijet events, especially when the mismeasurements are likely to be the larger source of error.

In an attempt to mitigate for these potential shortcomings, two event generators are employed to simulate the hard process at the matrix element level; these are `Pythia v8.150` [77] and `MadGraph v5.131` [81]. The former is focussed on processes featuring two partons in the final state, while `MadGraph` has been tested with up to five outgoing particles. Additional final state particles may arise due to processes such as Initial and Final State Radiation (ISR and FSR), so defining what constitutes an "n-jet" event is far from trivial in terms of labelling individual processes. The generator processes are therefore used only as a guide and results are combined where sensible. `Pythia 8` is used to perform the showering, hadronisation and secondary particle decay on the output of both generators.

The `Pythia 8` samples were generated with $3.5\,\mathrm{TeV}$ per proton beam, the `CTEQ6L1` PDF set and the `4C` tuning. The `HardQCD` $2 \rightarrow 2$ `Pythia` processes were used, with gluons and quarks up to and including the b quark in the initial and final states. Four samples with differing cuts on the hard process transverse momentum $\hat{p}_T$ were generated; the corresponding cross-section estimates are listed in Table 3.2.

---

[13] `Pythia 6` is described in [77]; further information regarding `Pythia 8` may be found at http://www.thep.lu.se/~torbjorn/Pythia.html

[14] Indeed, measurements from the LHC are needed to inform the matrix element calculations that go into multijet event generators.

Phase space cuts $\Sigma p_{\text{part.}}$ / GeV			$\sigma(2 \to 2)$ / pb			$\sigma(2 \to 3)$ / pb	$\sigma(2 \to 4)$ / pb
			Pythia 8	MadGraph 5	% diff.	MadGraph 5	MadGraph 5
[100	,	250]	8.17×10^6	7.49×10^6	-8.3	1.11×10^7	4.21×10^6
[250	,	500]	1.25×10^5	1.17×10^5	-6.4	2.93×10^5	3.27×10^5
[500	,	1000]	3.74×10^3	3.49×10^3	-6.7	9.85×10^3	1.32×10^4
[1000	,	∞]	6.55×10^1	6.05×10^1	-7.6	1.79×10^2	2.33×10^2

Table 3.2: Estimated cross-sections of the Pythia 8 and MadGraph 5 QCD samples, with a comparison of the $2 \to 2$ values produced by each generator.

The MadGraph 5 samples were also generated with $3.5\,\text{TeV}$ proton beams and the CTEQ6L1 PDF set. The pp > jj (where p and j are gluons or quarks up to and including the b quark) processes were simulated. MadGraph 5 allows the user to place phase space cuts on the sum of the outgoing parton transverse momentum $\Sigma p_{\text{part.}}$; thus to allow comparisons in the $2 \to 2$ regime, the phase space cuts were simply doubled (since in the two-body case, $\Sigma p_{\text{part.}} = 2\,\hat{p}_T$). Table 3.2 lists the cross-sections and compares the two-body results for Pythia 8 and MadGraph 5. One may note the slightly lower values reported for the MadGraph 5 samples; this can be explained by the additional kinematic requirements placed on the outgoing partons in the MadGraph 5 samples – a minimum p of $20\,\text{GeV}$ and a maximum $|\eta|$ of 5.

MadGraph 5 can be configured to simulate processes with more than two outgoing partons, which must also be considered given the cascade-rich nature of the super-symmetric signal. The cross-sections for the pp > jjj and pp > jjjj processes in each region of phase region are also listed in Table 3.2.

The output of the hard-process from MadGraph 5 was interfaced to Pythia 8 for showering, hadronisation and secondary decays. It should be noted that the jet matching techniques described in [82] were not used in this analysis; partly for the sake of simplicity, but also because matching partons to Initial State Radiation (ISR) and Final State Radiation (FSR) is more of an issue for heavy quark processes, which is not the focus of this analysis.

`Pythia 8`, like most event generators, produces an *event record* for each event. This consists of a list of initial, intermediary and final state particles particles, as well as information relating to the hard-scatter process. While the final state particles could be used as for the purpose of characterising the kinematics of the events this is emphatically *not* the approach adopted here. A simplified calorimeter-type detector is instead used to "filter" the generator-level final state particles into energy deposits. The dimensions, hermiticity and spatial resolution are taken from those of the CMS electromagnetic calorimeter; these are listed in Table 3.3 for convenience. The energy response function of the cells is that found in Equation 3.15, though for

Parameter	Description	Value	Units	Depends on
$z_{\text{max.}}$	z extension of the barrel regions.	268.4	cm	–
$\rho_{\text{max.}}$	Radius of the detector.	129.0	cm	–
$|\eta|_{\text{trans.}}$	η of the transition angle.	1.479	–	$z_{\text{max.}}, \rho_{\text{max.}}$
$\Delta\eta_B$	Barrel η cell spacing.	0.0174	–	–
$\sigma_{\eta B}$	Uncertainty in η measured in the barrel.	0.0052	rad.	$\Delta\eta_B$
$\Delta\phi_B$	Barrel ϕ cell spacing.	0.0174	rad.	–
$\sigma_{\phi B}$	Uncertainty in ϕ measured in the barrel.	0.0052	rad.	$\Delta\phi_B$
$|\eta|_{\text{max.}}$	Maximum measurable $|\eta|$.	3.0	–	–
Δx_{EC}	Endcap grid spacing.	2.481	cm	$\rho_{\text{max.}}, z_{\text{max.}}, \Delta\eta_B$
$\sigma_{\eta EC\,\text{max.}}$	Maximum uncertainty in endcap η.	0.0253	–	Δx_{EC}
$\sigma_{\phi EC\,\text{max.}}$	Maximum uncertainty in endcap ϕ.	0.0279	rad.	Δx_{EC}
E_{max}	Maximum E measurable in a cell.	3500.0	GeV	$\sqrt{s}$
b	Length of cell output word.	16	Bits	–
$\Delta E_{\text{res.}}$	Energy measurement resolution.	0.0534	GeV	E_{max}, b
E_{min}	Minimum E measurable in a cell.	0.0534	GeV	$\Delta E_{\text{res.}}$

Table 3.3: The parameters $\mathbf{\Psi}$ used in the definition of the simple measurement system.

now $\kappa = \nu = \zeta = 0$ (i.e. it is a perfect detector). The effects of an external magnetic field are not simulated.

The Σe and $\not{p}$ distributions for the LM0 and LM1 CMSSM benchmark points, and the QCD processes, with the two-body samples plotted separately for the two different generators, are shown in Figures 3.2 and 3.3 respectively. One may note the following:

- While the signal is dominated by large Σe events, the QCD distribution is peaked in the $200\,\mathrm{GeV}$ region (and would be more so if the lower regions of phase space were simulated). However, the QCD tail still swamps the signal;

- As discussed, the tail of the signal $\not{p}$ distribution is far longer than that of the QCD samples, which peaks in the $0 - 20\,\mathrm{GeV}$ bin;

- The QCD $\not{p}$ distribution is not as narrow as one might naïvely expect for processes that are not supposed to feature invisible particles. This is largely due to the lack of detector hermiticity.
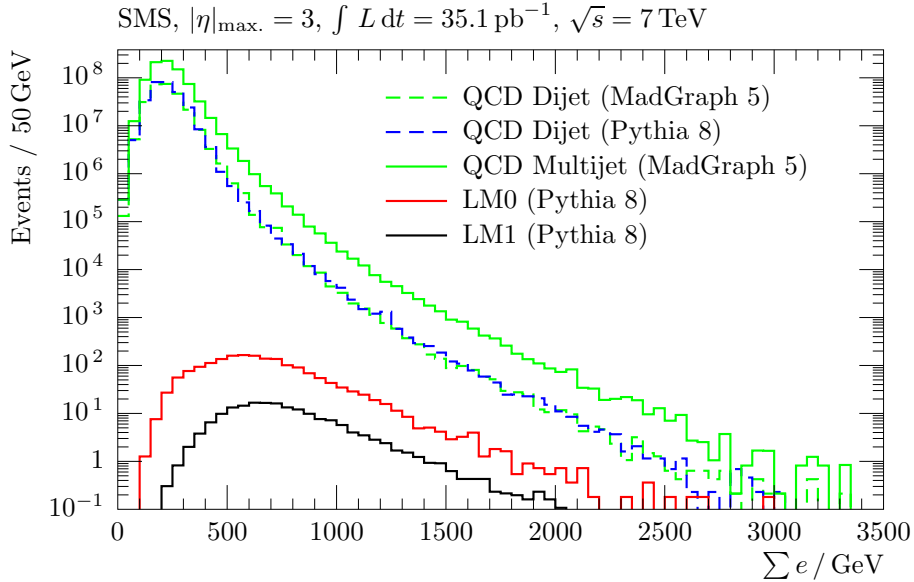
Figure 3.2: The sum of the cell transverse energies for the QCD samples used in the toy analysis, compared to the benchmark CMSSM points.

3.2.2   Implementing the search strategy

In order to apply the multi-jet α_T observable to the all-hadronic search, there is one additional step to consider. The hadronisation of the outgoing partons typically results in a collimated shower of particles that spreads over more than one detector cell. It is therefore useful to either remove the contribution from cells with only
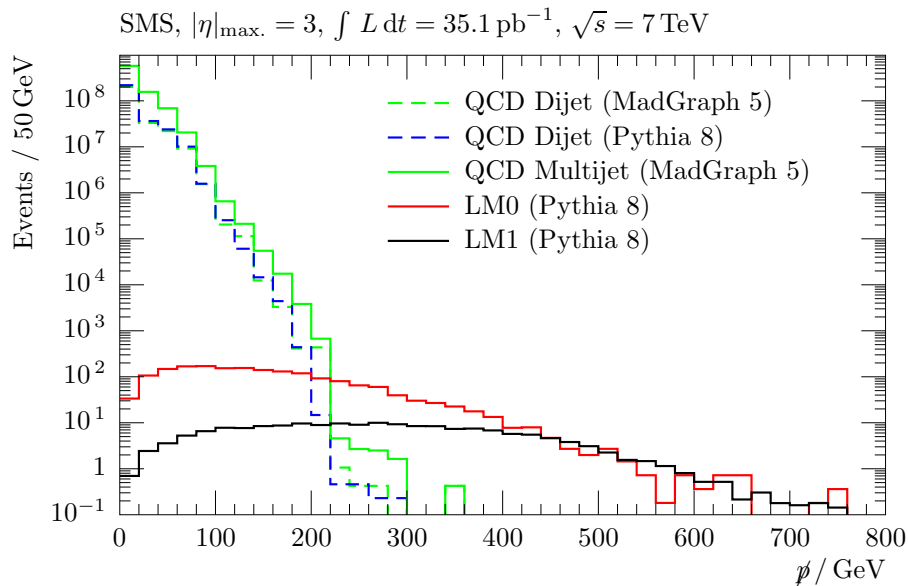
Figure 3.3: The missing transverse momentum distributions for the QCD samples used in the toy analysis, compared to the benchmark CMSSM points.

a small amount of energy deposited in them by applying a minimum threshold, or to group the energy deposits together and combine them using the E-scheme (Equations 3.3 - 3.6) them into a single "cluster" that should approximate the 4-momentum of the original parton. This helps to reduce the number of inputs to a manageable number, as well as defining the jet multiplicity of the event.

Thresholding is the exclusion of a cell's contribution if the energy or transverse energy of said cell falls below a user-defined value (the *threshold*). This is done with the aim of removing detector noise, contributions from collision products that are too small to impact in a meaningful way on the parameter extraction process, or simply cells with $\varepsilon = 0$ (i.e. those that do not register the minimum measurable energy). Of course, the observer must be confident that the impact of thresholding has a neglible impact on what she hopes to find out about the phenomena under investigation; as will be seen later, this is not always the case.

Clustering is the process by which the contributions from two or more individual cells are combined in some way. The key decisions the observer must make when

deciding upon how the clustering is employed are: which of the N_{cells} cells should be combined together, and how should their contributions be combined? The first question has been studied at great length in the "jetography" literature; an excellent summary can be found in [66]. It is instructive to briefly examine the clustering techniques that have been developed by the jet community. Very briefly, these are:

- **Cone algorithms**: These use cones defined in $\phi - \eta$ space to group particles (n.b. not necessarily cells) together. The directions of the cones are found by using an iterative algorithm – either seeded as in the Iterative Cone (IC) algorithm, or the seedless SISCone algorithm.

- **Sequential recombination algorithms**: Rather than using a pre-determined cone structure, this class of clustering algorithm relies on the calculation of some distance measure between each of the input particles. This metric is then compared with some user-assigned threshold value or values in order to determine whether to combine the particles together or discard one or both of them (in this sense, some of the clustering algorithms discussed here incorporate a degree of thresholding too). Examples include the Jade algorithm [83, 84], the exclusive [85, 86] and inclusive [87] k_T algorithms, the Cambridge [88]/Aachen [89] algorithms, and the anti-k_T algorithm [90].

As of the time of writing, the last of these is the algorithm of choice of the CMS collaboration. The distance measures employed by the anti-k_T algorithm are

$$
d_{ij} \;=\; \text{min.}\;\left(p_i^{2k},\, p_j^{2k}\right) \frac{\Delta R_{ij}^2}{R^2}, \quad \Delta R_{ij}^2 = (y_i - y_j)^2 + (\phi_i - \phi_j)^2 \tag{3.33}
$$

$$
d_{iB} \;=\; p^{2k}, \tag{3.34}
$$

where $k = -1$ for the anti-k_T algorithm ($k = 1$ for the k_T algorithm, $k_T = 0$ for the Cambridge/Aachen algorithm), R is a user-specified value roughly corresponding to a cone radius in $\phi - \eta$ space, and d_{iB} represents the corresponding distance to

the beam (as opposed to another particle under consideration). The algorithm then proceeds as follows (reproduced from [66] for convenience):

1) Work out all the d_{ij} and d_{iB} according to Equations 3.33 and 3.34;

2) Find the minimum of the d_{ij} and d_{iB};

3) If it is a d_{ij}, recombine i and j into a single new particle and return to step 1;

4) Otherwise, if it is a d_{iB}, declare i to be a [final-state] cluster, and remove it from the list of particles. Return to step 1;

5) Stop when no particles remain.

This procedure results in a set of $M_{\mathrm{cl.}}$ final-state clusters that grow out from hard "seeds" in a manner that is both infrared and collinear safe (i.e. the addition of soft particles or the arbitrary splitting of a cluster leaves the final set of clusters unchanged). Unless otherwise stated, this work will use the anti-k_T algorithm for the clustering of objects.

The second question, concerning how the clustered particles/cells should be combined, has already been addressed to an extent; the CMS Collaboration uses the 4-vector addition scheme (Equations 3.3 - 3.6). While this might seem like an obvious choice, it is worth bearing in mind two points. Firstly, alternatives have been proposed and used (see § 2.4 of [66]) that involve combining the p-weighted ϕ and η and rescaling the energy of the new object such that it is massless. Secondly, and perhaps more importantly, a simple calculation shows that the transverse energy of two particles combined according to the E scheme will be different to the sum of the individual particles' transverse energy,

$$
\begin{aligned}
e_{ij}^2 &= (E_i + E_j)^2 - (q_i + q_j)^2 & (3.35) \\
&= e_i^2 + e_j^2 + 2\,e_i\,e_j\,\cosh\Delta y & (3.36) \\
&\neq (e_i + e_j)^2\,, & (3.37)
\end{aligned}
$$

unless $\Delta y \equiv y_i - y_j = 0$. Thus when calculating quantities like e_{cluster} or Σe, the order in which the particles are combined matters, and so different strategies will produce different results. The use of $p(\equiv p_T)$, a vectorial quantity, is not affected by this issue. However, when p is used, the mass information (otherwise retained with $e^2 = p^2 + M^2$) is lost. Thus when choosing whether to use e or p as an observable, the observer must be consistent and must understand why they are using it.

Having described thresholding and clustering, they may be applied to the detector output to obtain $M_{\text{cl.}}$ clusters as follows:

- all cells with $\varepsilon = 0$ are discarded (initial thresholding);

- the cells are clustered according to the anti-k_T algorithm with $R = 0.5$;

- only clusters with $e > 50\,\text{GeV}$ count towards the cluster multiplicity, $M_{\text{cl.}}$, that defines the event topology.

The following selection criteria are then applied in order to identify events in the signal region:

- The sum of the clustered energy must be larger than $350\,\text{GeV}$, i.e. $\Sigma h \equiv \sum_{i=1}^{M_{\text{cl.}}} e_i > 350\,\text{GeV}$. e_i is the transverse energy of the ith cluster. This removes a great deal of the QCD background, as shown in Figure 3.2;

- The "leading cluster" (that with the largest e) is required to have $|\eta| < 2.5$. This is to avoid selecting events where the lack of detector hermiticity may lead to fake missing transverse momentum;

- The two leading clusters must each have $e > 100\,\text{GeV}$;

- The event must have $\alpha_T > 0.55$, where the $M_{\text{cl.}}$ clusters are used as input to the α_T calculation.

The dijet and multijet topologies are considered separately. Firstly, for the dijet case the Σh, $\not{h} \equiv -\sum_{i=1}^{M_{\rm cl.}} \mathbf{p}_i$, $\Delta\phi$ and $\Delta h = e_1 - e_2$ for signal and background events measured with the simple, idealised calorimeter ($\kappa = 0.0\,\mathrm{GeV}^{1/2}$) meeting all of the selection criteria bar the α_T cut are plotted in Figures 3.4, 3.5, 3.6 and 3.7 (statistical errors in these and subsequent plots are indicated by the shading). Σh and $\not{h}$ are comparable in shape with the Σe and $\not{p}$ plots of Figures 3.2 and 3.3, though the kinematic preselection requirements have reduced the available phase space and so reduced the sample yields.

Inspecting the dijet-specific variables, one finds that the QCD samples have the $\Delta\phi$ distribution peaked at $\sim \pi$, whereas the signal (with real missing transverse momentum) has a $\Delta\phi$ distribution that is much flatter. It is also interesting to note the similarity in the shapes of the Δh and $\not{h}$ distributions for the QCD samples, which is not mirrored in the signal distributions.

The corresponding kinematic observable plots for the multijet topology are shown in Figures 3.8 and 3.9 (bearing in mind that Δh and $\Delta\phi$ cannot be defined for more than two objects). Again, the similarity to Figures 3.2 and 3.3 is noted. Inspecting both of the α_T distributions in Figures 3.10 and 3.11, the edge at $\alpha_T = 0.5$ is clearly visible for both topologies.

The number of events passing each of the selection cuts is given in Table 3.4. A closer inspection of this cutflow table shows that, for these relatively small samples at least, all QCD background events are rejected in the dijet case and for the multijet selection from the $40,000$ event `Pythia 8` dijet QCD sample (i.e. where extra jets have radiated from the original two-parton interaction). The $120,000$ event `MadGraph 5` multijet QCD sample actually contains three events that pass the $\alpha_T > 0.55$ cut. Examining these events by hand yields some interesting insights:

- Two events with $\alpha_T = 0.61, 0.55$ were found to have $\not{h} = 210.1\,\mathrm{GeV}$, $202.6\,\mathrm{GeV}$ but an unclustered (i.e. from all of the cells) $\not{p} = 1.8\,\mathrm{GeV}$, $41.7\,\mathrm{GeV}$. This
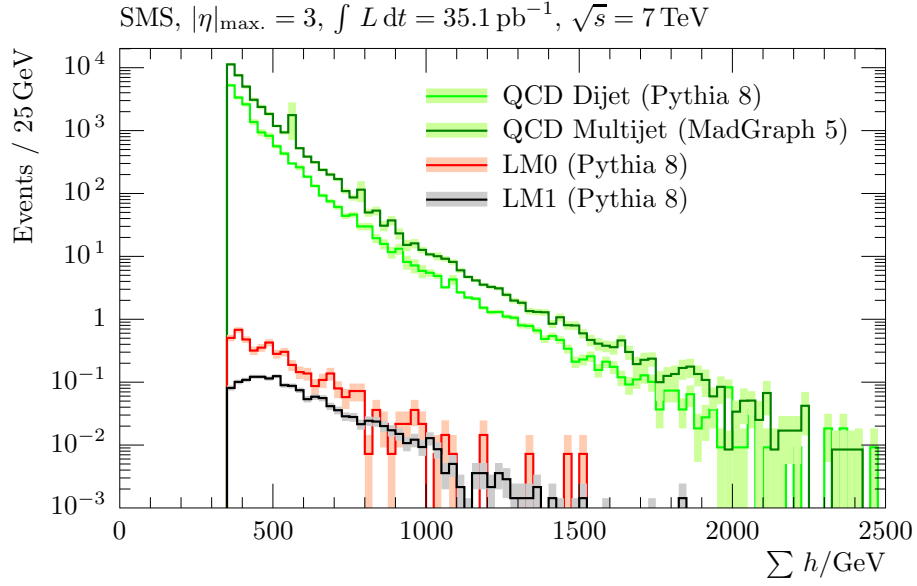
Figure 3.4: Sum of the transverse energy, Σh, of the dijet sample for the toy analysis.

Figure 3.5: $\not{p}$ from the clustered energy, $\not{h}$, of the dijet sample for the toy analysis.
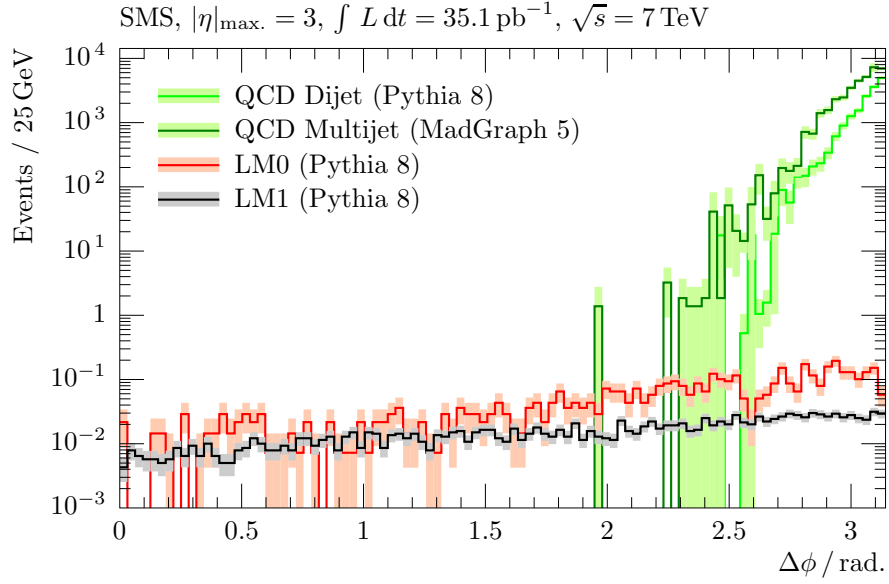
Figure 3.6: Cluster acoplanarity, $\Delta\phi$, of the dijet sample for the toy analysis.
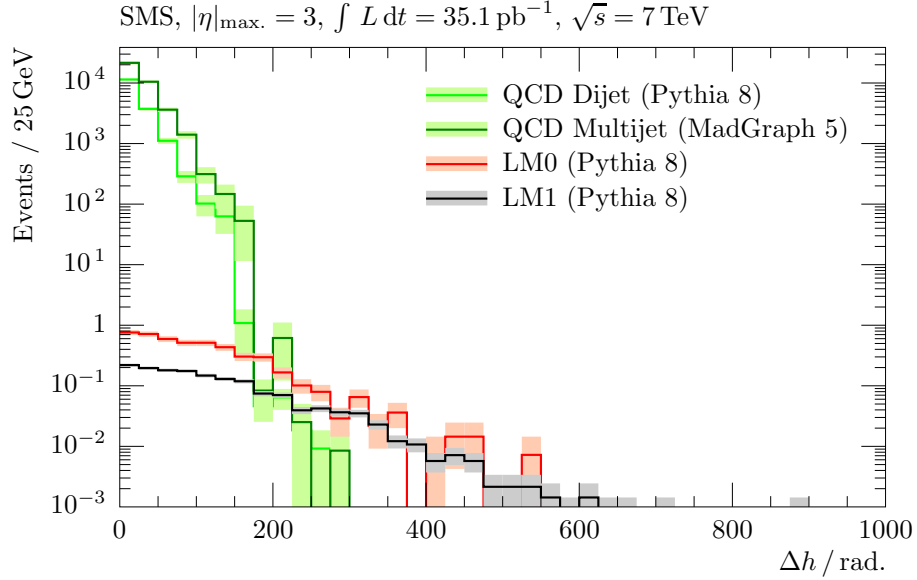
Figure 3.7: Transverse energy imbalance, Δh, of the dijet sample for the toy analysis.
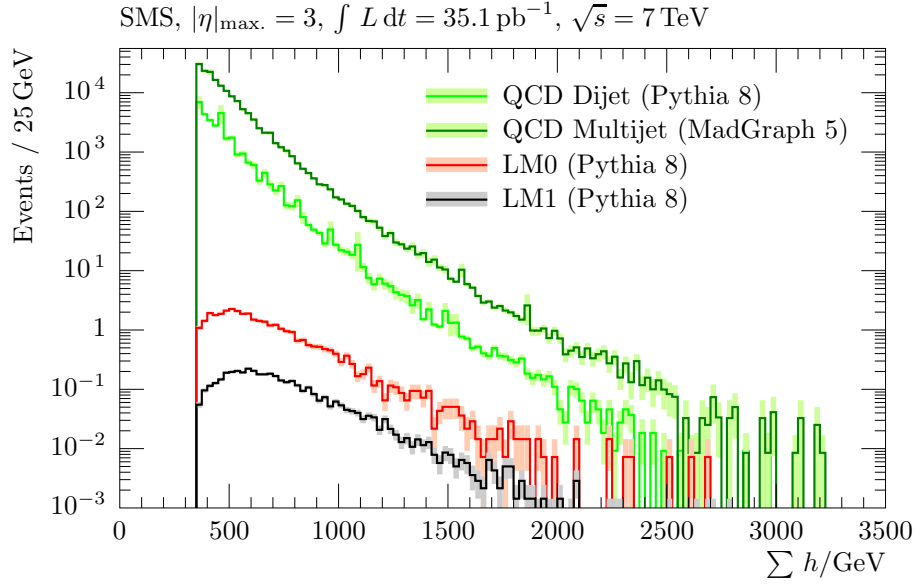
Figure 3.8: Sum of the transverse energy, Σh, of the multijet sample for the toy analysis.

Figure 3.9: $\not{p}$ from the clustered energy, $\not{h}$, of the multijet sample for the toy analysis.
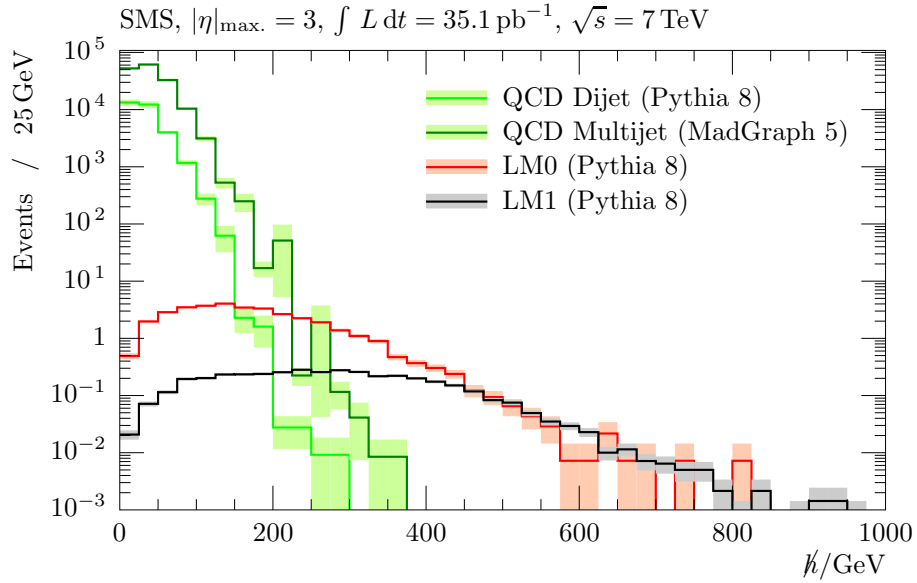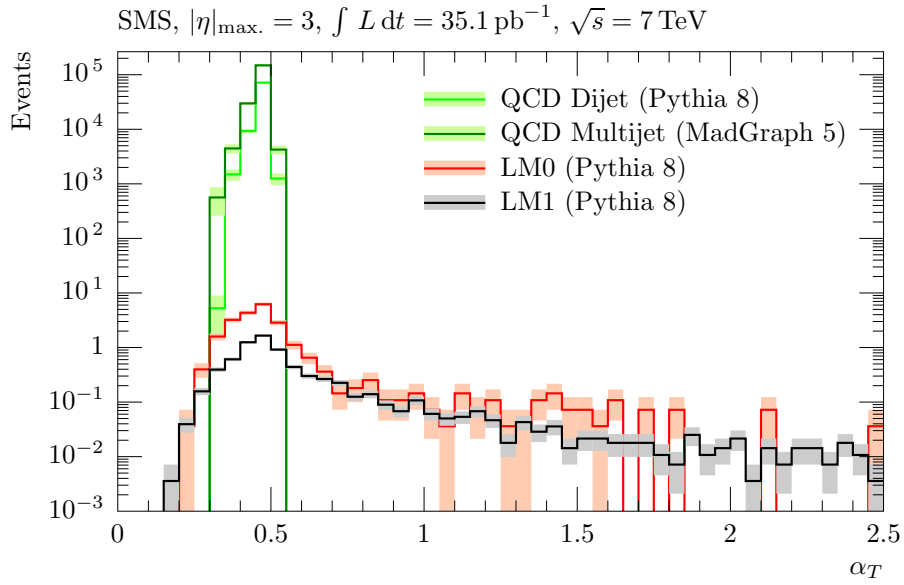
Figure 3.10: α_T distribution for the dijet ($M_{\mathrm{cl.}} = 2$) toy analysis.
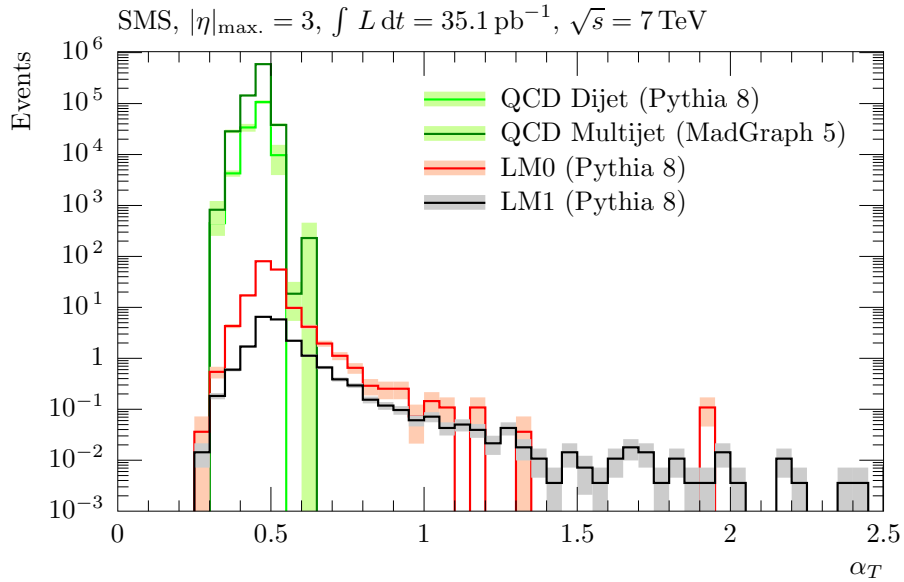
Figure 3.11: α_T distribution for the multijet ($M_{\mathrm{cl.}} \geq 3$) toy analysis.

suggests that, in this system where the energy measurement is perfect (i.e. $\kappa = 0.0$), fake $\not{p}$ is being generated by several reconstructed clusters falling under the $50\,\text{GeV}$ threshold. Thus m is artificially small, resulting in a large α_T value that the Δh cannot correct for. In the final analysis presented in Chapter 5, the following auxiliary cut is imposed to account for this effect:

$$\frac{\not{h}}{\not{p}} < 1.25; \tag{3.38}$$

- The remaining event with $\alpha_T = 0.56$ was found to contain a $p = 110\,\text{GeV}$ neutrino from a W decay, and so actually contained real missing energy. The accompanying lepton had $p = 28\,\text{GeV}$ and $\eta = -0.11$ and so in the full analysis this event would have been caught by the lepton veto (which is, as will be explained later, designed to remove contributions from precisely this type of event).

Thus it has been shown that α_T removes the vast majority of conserved QCD background in the toy analysis, and that even the handful of events passing the chosen cut value of $\alpha_T = 0.55$ may be explained by the limitations of such a simplified measurement system. The limited size of the samples means that these three events have a large weighting; the statistical errors on the cut flow numbers reflect this fact. These few events are not of immediate concern; what is more interesting is the robustness of the α_T variable to changes in the measurement system parameters and how this sensitivity influences the cut value chosen. This is the subject of the following subsection.

3.2.3   Evaluating the robustness of a given strategy

When formulating a cut-based analysis strategy, often one of the hardest elements for the observer to justify is the cut values chosen when she makes a decision about

	s		b	
Cut	LM0	LM1	`Pythia 8` dijet	`MadGraph 5` multijet
$j_1 : \lvert\eta\rvert < 2.5$	$(1.78 \pm 0.02) \times 10^3$	$(1.78 \pm 0.02) \times 10^2$	$(2.17 \pm 0.02) \times 10^8$	$(4.89 \pm 0.04) \times 10^8$
$j_2 : e > 100\,\mathrm{GeV}$	$(1.11 \pm 0.01) \times 10^3$	$(1.48 \pm 0.02) \times 10^2$	$(1.23 \pm 0.27) \times 10^6$	$(1.60 \pm 0.04) \times 10^7$
$\Sigma\, e > 350\,\mathrm{GeV}$	$(1.00 \pm 0.01) \times 10^3$	$(1.40 \pm 0.02) \times 10^2$	$(1.20 \pm 0.06) \times 10^6$	$(4.97 \pm 0.10) \times 10^6$
$M_{\mathrm{cl.}} = 2$	$(1.17 \pm 0.05) \times 10^2$	$(3.86 \pm 0.08) \times 10^1$	$(4.18 \pm 0.12) \times 10^5$	$(9.39 \pm 0.35) \times 10^5$
$\alpha_T > 0.55$	$(2.35 \pm 0.21) \times 10^1$	$(1.35 \pm 0.05) \times 10^1$	$(0.00 \pm 0.00) \times 10^0$	$(0.00 \pm 0.00) \times 10^0$
$M_{\mathrm{cl.}} \geq 3$	$(8.84 \pm 0.13) \times 10^2$	$(1.02 \pm 0.01) \times 10^2$	$(7.78 \pm 0.60) \times 10^5$	$(4.03 \pm 0.10) \times 10^6$
$\alpha_T > 0.55$	$(9.51 \pm 0.41) \times 10^1$	$(2.78 \pm 0.07) \times 10^2$	$(0.00 \pm 0.00) \times 10^0$	$(1.24 \pm 1.15) \times 10^3$

Table 3.4: Number of events passing the (pre)selection criteria of the toy analysis for the $M_{\mathrm{cl.}} = 2$ and $M_{\mathrm{cl.}} \geq 3$ final state topologies. The event yields are scaled to $35.1\mathrm{pb}^{-1}$.

what qualifies as a signal event. When obtaining an estimate of some phenomeno-logical parameter, the erroneous inclusion of a background event or the loss of a signal event will, generally speaking, result in a shift of the value measured and the associated uncertainty. While the resulting loss of accuracy is undesirable, it is seldom disastrous in terms of what is learned from performing the experiment.

This situation may be contrasted with that of the discovery experiment. If a surplus of non-signal events leads to the incorrect rejection of the null hypothesis the consequences can be embarrassing at best, and credibility-damaging at worst. On the other hand, the over-zealous rejection of actual signal events that may have otherwise led to a discovery is sub-optimal. A quantitative discussion of these factors would be useful to the observer when deciding upon which search strategy to adopt.

Defining $x \in \{0,\, 1\}$ as the variable describing whether or not the event is from the signal or background sample, and $y \in \{0,\, 1\}$ as the variable describing whether or not the event passes or fails a given cut, one may define a quantity known as the Probability of Block Error (PBE)[15]:

$$p_B = \sum_{x \in \mathcal{A}_X} \Pr(x = x_i)\, \Pr(y \neq x_i \mid x = x_i). \tag{3.39}$$

---

[15] The Probability of Block Error (PBE) is a term borrowed from information theory that happens to suit the needs of this discussion [91].

Then given a sample of n candidate events (i.e. events that are to be considered as falling within the signal region, having passed some set of preselection criteria), one may define

$$n = s + b = s_+ + s_- + b_+ + b_- \tag{3.40}$$

where s_+ (s_-) is the number of signal events s passing (failing) the cut on the variable used to determine the outcome y, and b_+ (b_-) is the number of background events b passing (failing) the same cut. The PBE is then calculated as

$$
\begin{aligned}
p_B &= \Pr(x = 0) \times \Pr(y = 1 \,|\, x = 0) + \Pr(x = 1) \times \Pr(y = 0 \,|\, x = 1) \\
&= \frac{b}{n} \times \frac{b_+}{b} + \frac{s}{n} \times \frac{s_-}{s} \\
&= \frac{b_+ + s_-}{n}.
\end{aligned}
\tag{3.41}
$$

It may then be argued that, for a given signal, background and measurement system the optimal search strategy is the one that minimises p_B. For the signal, backgrounds and observables considered so far, one may demonstrate the concept with a simple example:

- An event is considered "interesting" if $\Sigma\,e > 350\,\mathrm{GeV}$ (a cursory inspection of Figure 3.2 suggests this removes a lot of the QCD background while retaining the majority of the signal);

- An interesting event is considered a signal candidate ($y = 1$) if the missing transverse energy $\displaystyle{\not}{p}$ is greater than some cut value $\displaystyle{\not}{p}_{\mathrm{cut}}$, and a background candidate ($y_{\not p} = 0$) if $\displaystyle{\not}{p} < \displaystyle{\not}{p}_{\mathrm{cut}}$.

The number of events passing the $\Sigma\,e$ cut in each sample is listed in Table 3.5 to give an indication of the differing magnitudes between the signal and the background. p_B as a function of $\displaystyle{\not}{p}_{\mathrm{cut}}$ is plotted in Figure 3.12. The sample names either side of the "vs" in the legend refers to which signal is being compared with which background in the plot; only one signal and one background can be compared at a time. The following observations may be made after an inspection of these plots:

- Although one may remove the background contribution to p_B by simply setting the $\not{p}_{\text{cut}}$ to the maximum predicted $\not{p}$ in the QCD samples, p_B takes into account the fact that signal events may be lost due to an over-conservative cut value.

- Likewise, p_B may still be used as as a useful metric when considering the null hypothesis, i.e. when $s_+ = s_- = s = 0$, or when, as in this situation, the background contribution to the block error calculation is dominant. This may be inferred by noting that in Figure 3.12 the solid black line that represents p_B closely follows the filled area,

$$\Pr(y = 1|\, x = 0) = \frac{b_+}{b}, \tag{3.42}$$

  which is the conditional probability that an error has been made in determining whether or not a (QCD) background event lies in the signal region according to the event's measured missing transverse momentum.

- While robustness is important, when the potential signal is small compared to the background the true-negative (i.e. rejected signal events) error rate must be carefully taken into account when choosing the search strategy. The author was involved in an attempt to apply the α_T method to a GMSB-based supersymmetry search with a diphoton plus jets final state. The large fraction of true-negatives, due to a small $\not{p}/\Sigma\, e$ fraction in the signal and the photon identification inefficiencies, meant that while the measured background was suppressed, so too was the signal. Consequently, the α_T strategy was rejected and a search based on the more traditional $M_{\text{eff.}} \equiv \Sigma\, e + \not{p}$ observable was adopted.

Inspecting Figure 3.12, it would appear that if the observer was to use $\not{p}$ as the discriminating observable in the signal criteria, she should set $\not{p}_{\text{cut}}$ to $\sim 120\,\text{GeV}$. This would minimise the chance of erroneously selecting QCD-like events as signal

| | s | | b | |
Cut	LM0	LM1	`Pythia 8` dijet	`MadGraph 5` multijet
$\Sigma\,e > 350\,\mathrm{GeV}$	1.64×10^3	1.76×10^2	1.45×10^7	6.15×10^7

Table 3.5: Number of events passing the pre-selection criterion $\Sigma\,e > 350\,\mathrm{GeV}$, scaled to $35.1\mathrm{pb}^{-1}$.
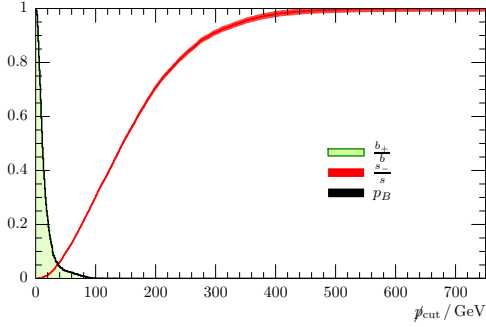
(a) LM0 vs. `Pythia 8` dijet QCD.
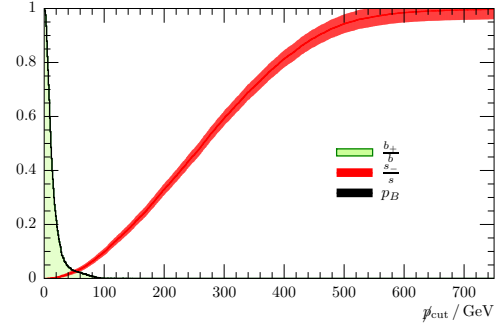
(b) LM0 vs. `MadGraph 5` multijet QCD.
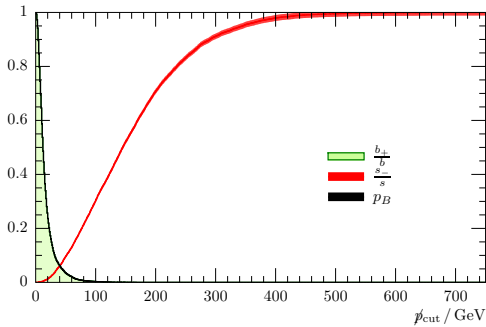
(c) LM1 vs. `Pythia 8` dijet QCD.
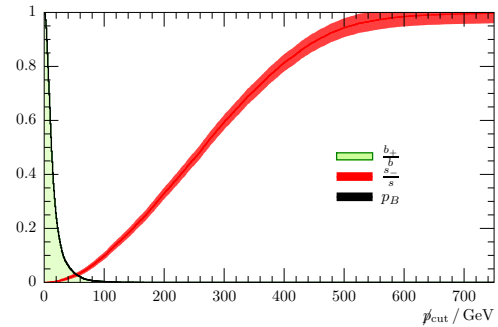
(d) LM1 vs. `MadGraph 5` multijet QCD.

Figure 3.12: Probability of block error plots for various signal vs. QCD background scenarios. The contributing conditional probabilities (see Equation 3.41) are also plotted. The vertical spread represents the statistical error.

candidates, in light of the simulations carried out which are in turn based on the observer's prior knowledge.

However, these plots and error calculations have been made using an idealised calorimeter; mismeasurements due to the energy response have not been part of the measurement system model. Figures 3.12a and 3.12b show the p_B plots corresponding to the LM0 benchmark point compared with the `Pythia 8` dijet and `MadGraph 5` multijet samples respectively for different values of the stochastic error term, κ, from 0.0 to 5.0 $\mathrm{GeV}^{1/2}$. Given that the decision to either accept ($y = 1$) or

reject ($y = 0$) an event as signal or background is made by selecting events above the chosen cut value, one would hope that the behaviour of p_B as $\not{p}_{\mathrm{cut}}$ was decreased from its maximum value (i.e. the value at which even all of the signal is rejected) would at least indicate to the observer that the choice of cut value was well-motivated and that p_B was unaffected by the uncertainty in the measurement system parameters.

However, one may note from Figure 3.13 that this is not the case. The effect of increasing κ is clear – in the "conserved" QCD background samples, the tail of the $\not{p}$ distribution extends to larger values as the errors get worse (though the energy response is only gaussian in nature). This results in a longer tail in the p_B distribution over the possible cut values. The slope of the p_B distribution (as a function of $\not{p}_{\mathrm{cut}}$) gently increases as $\not{p}_{\mathrm{cut}}$ is lowered, suggesting that the range of cut values around the actual optimal $\not{p}_{\mathrm{cut}}$ value is not well defined given what is known about the background or the measurement system. What is more, a different κ value used in the measurement system simulation results in a shift of the p_B distribution to the right. The $\not{p}_{\mathrm{cut}}$ must be raised to ensure that mismeasured events do not meet the signal criterion – to the detriment of the predicted signal yield.

It is therefore difficult for the ill-informed observer (i.e. an observer who does not know the value of κ for their calorimeter) to know *a priori* which value of $\not{p}_{\mathrm{cut}}$ would be best to use. It would be convenient if observables could be constructed that were in some way protected from such sources of inherent uncertainty in the system. This is what has been achieved with the α_T variable, as shall now be demonstrated.

Firstly, the corresponding p_B plot may be made for the clustered events passing the toy analysis preselection criteria; Figure 3.14 shows p_B as a function of $\not{h}_{\mathrm{cut}}$ for the $M_{\mathrm{cl.}} = 2$ and the $M_{\mathrm{cl.}} \geq 3$ topologies. Despite the reduction in the available phase space (and thus reduced statistics), the same features indicative of an instability of the cut value with respect to κ may be identified.

(a) LM0 vs. `Pythia 8` dijet QCD.   **(b)** LM0 vs. `MadGraph 5` multijet QCD.
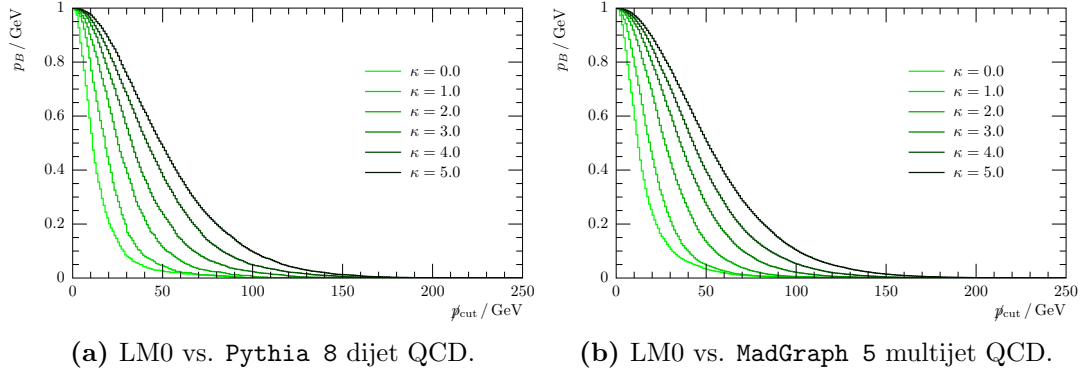
Figure 3.13: Probability of block error plots as a function of the missing transverse momentum $\not{p}$ cut value for a selection of stochastic resolution terms for two of the signal vs. QCD background scenarios.

(a) $M_{\text{cl.}} = 2$.   **(b)** $M_{\text{cl.}} \geq 3$.
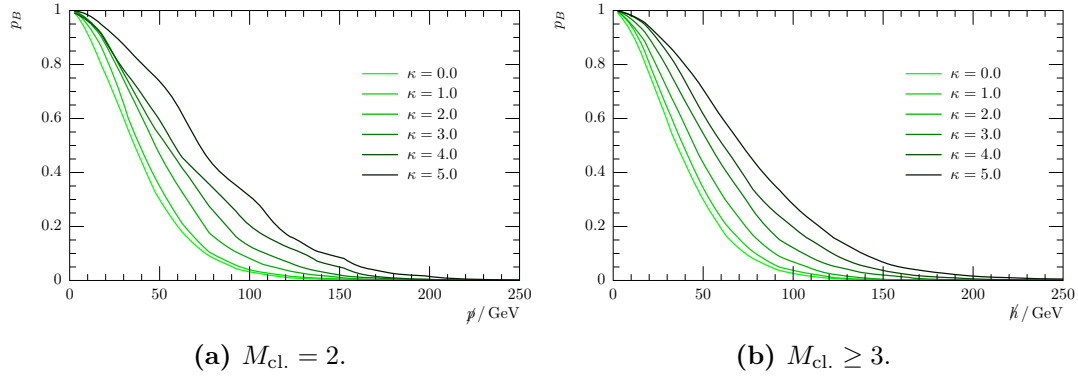
Figure 3.14: Probability of block error plots as a function of the $\not{h}$ cut value for a selection of stochastic resolution terms, LM0 vs. `MadGraph 5` QCD background. The cluster preselection criteria were applied to the events.

The equivalent p_B plots for the α_T variable are shown in Figure 3.15 for $M_{\text{cl.}} = 2$ and Figure 3.16 for $M_{\text{cl.}} \geq 3$ for the LM0 and `MadGraph 5` multijet signal and background samples. Inspecting these plots, the benefits of a strategy using such a variable for this particular search become clear:

- As the $\alpha_{T\text{ cut}}$ value is lowered from the maximum, there is a sharp increase in p_B just above the $\alpha_{T\text{ cut}} \sim 0.5$ point (the plots in Figures 3.15 and 3.16 on the right show the left-hand plots zoomed in around $\alpha_{T\text{ cut}} = 0.5$ to demonstrate this). This "natural" cut value arises naturally from the definition of α_T, but the p_B plot makes the benefit of using a variable with a sharp "edge"

in its distribution clear: the Probability of Block Error increases sharply as the cut value is lowered beyond this natural and well-motivated edge value – something that is crucial for a background-dominated search for an unknown signal where a conservative approach is necessary;

- More importantly, it may be seen from Figure 3.15 and particularly Figure 3.16 that as the value of κ increases, the p_B distribution only widens significantly for the lower values of α_T – i.e. away from the optimal value of p_B, where the p_B is stable as κ is varied. Thus it may be concluded that, due to the sharp edge in the α_T distribution, the α_T cut is robust to uncertainty in the measurement system's energy resolution, which is what was to be demonstrated. Regardless to the change in, for example, the stochastic term in the energy resolution of the calorimeter cells, α_T self-corrects such that background events do not pass the signal criterion and so erroneous outcomes are avoided.

- Finally, to show that this demonstration of robustness is not just some special property of α_T, the p_B distributions for the $\Delta\phi$ and Δh observables are shown (for the dijet events) in Figure 3.17. $\Delta\phi$, based only on angular information, remains relatively stable as κ is varied; Δh exhibits the same behaviour as $\not{p}$ (as one would expect).

(a) LM0 vs. `MadGraph` 5 QCD.   (b) LM0 vs. `MadGraph` 5 QCD (zoomed).
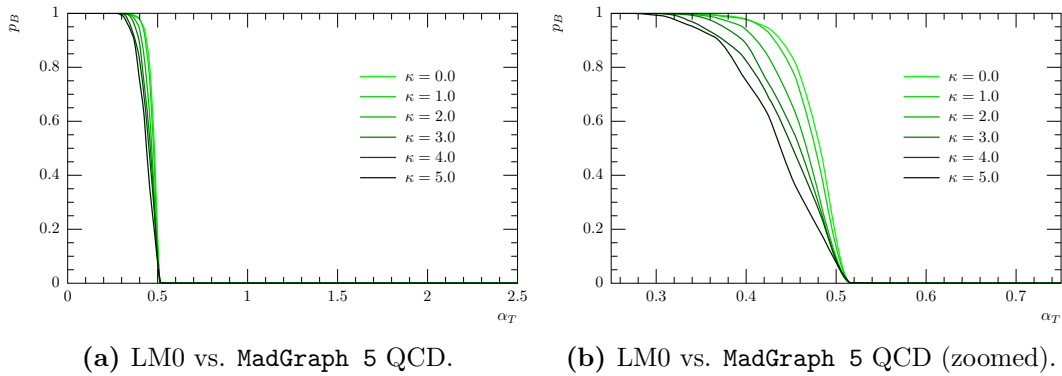
Figure 3.15: Probability of block error plots as a function of the α_T cut value ($M_{\text{cl.}} = 2$) for a selection of stochastic resolution terms.

(a) LM0 vs. `MadGraph` 5 QCD.   **(b)** LM0 vs. `MadGraph` 5 QCD (zoomed).
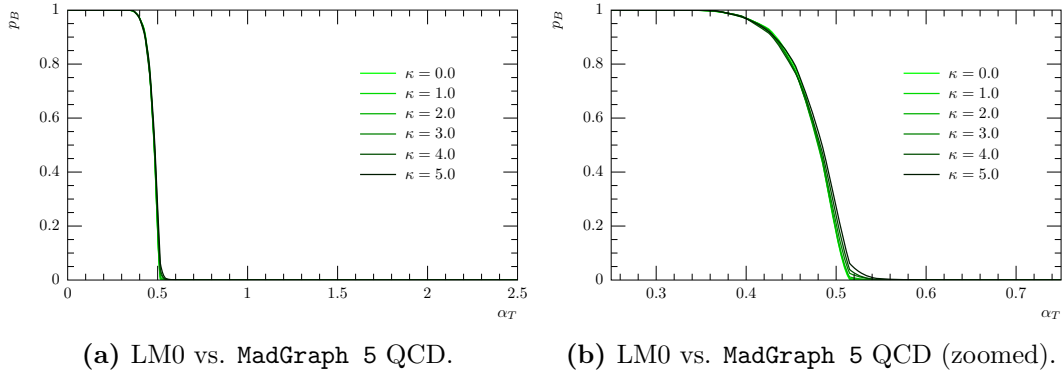
Figure 3.16: Probability of block error plots as a function of the α_T cut value ($M_{\text{cl.}} \geq 3$) for a selection of stochastic resolution terms.

(a) $\Delta\phi$ (angular).   **(b)** Δh (energy).
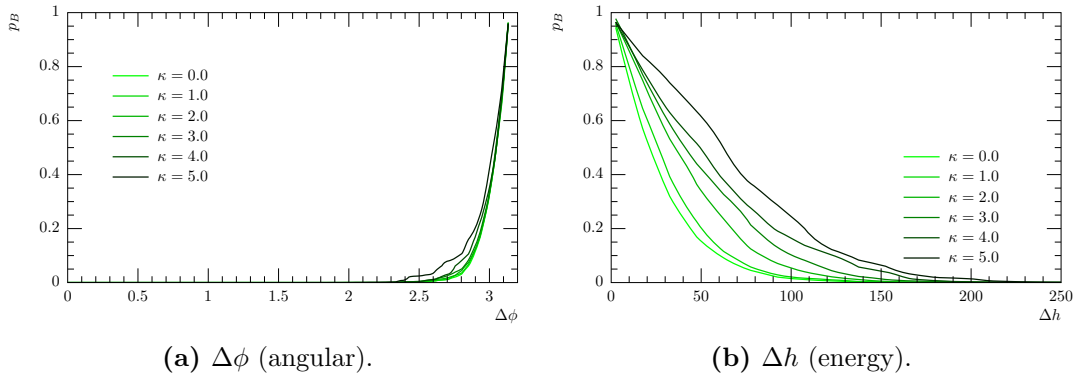
Figure 3.17: Probability of Block Error plots for $\Delta\phi$ and Δh in the dijet topology as a function of the cut values for a selection of stochastic resolution term values, LM0 vs. `MadGraph` 5 QCD background.

Having demonstrated the *a priori* robustness of α_T to uncertainty to a simple measurement system's energy measurement capabilities in this toy analysis, the discussion may now turn to implementing the strategy for the first search for supersymmetry with the CMS detector using the first $35.1\,\text{pb}^{-1}$ of LHC proton-proton collisions.

Chapter 4

Physics Object Reconstruction with the CMS Experiment

"A definition is the enclosing a wilderness of idea within a wall of words"

Samuel Butler, *Notebooks (1912)*

Having established *a priori* that α_T is a suitably robust discriminating variable when there is uncertainty in the extent of energy mismeasurement in the measurement system, it becomes necessary to discuss how the full detector information should be used to obtain events featuring jets and *only* jets in the final state. Jets – the physics objects that represent the hadronised remnants of outgoing partons – have until now been defined in terms of clustered energy deposits in an idealised calorimeter. It is now time to consider how jets are reconstructed from all of the available detector information, as well as examine the techniques employed to correct (on a jet-by-jet basis) for any detector failings, and obtain estimates of the jet energy scale and associated uncertainties. Additionally, events that are found to contain photons, electrons or muons (or some combination of these physics objects) in the final state must be removed from the analysis chain so that a pure "all-hadronic"

data set is obtained. The reconstruction and identification of these physics objects must therefore be performed for each event, using well-understood definitions and selection criteria. These are typically borrowed from other analyses from within the CMS Collaboration. The chapter therefore proceeds as follows: an overview of the CMS detector subsystems is presented in § 4.1. Then the jet reconstruction and correction methodology is recounted in § 4.2, and finally the reconstruction of other physics objects is summarised in § 4.3.

4.1   The Compact Muon Solenoid experiment
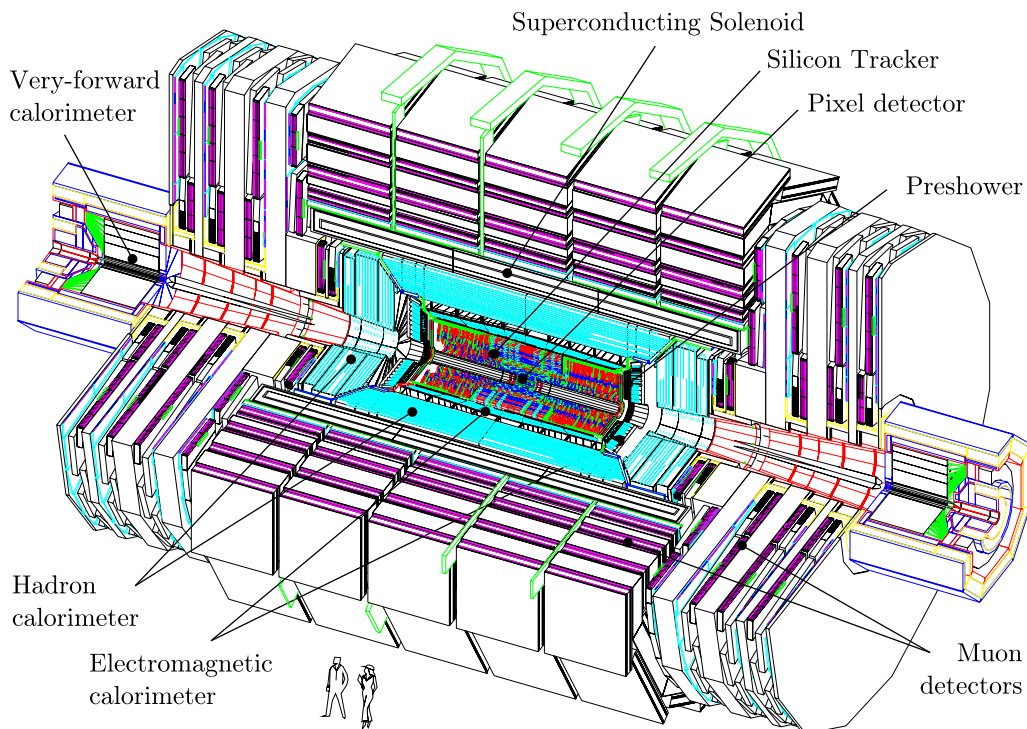
Figure 4.1: A cutaway view of the CMS experiment, showing the major detector subsystems [71].

The CMS experiment [71] is a general purpose detector situated at IP 5 of the LHC. The defining feature is the superconducting solenoid magnet that sits at the heart of the apparatus. Cooled to 4.5 K with liquid helium, it provides an axial 3.8 T magnetic field over a 13 m long, 5 m diameter cylinder, necessary to achieve the

required 10% momentum resolution for 1 TeV muons. A schematic of the apparatus is shown in Figure 4.1.

The design of the detector subsystems is heavily influenced by that of the magnet system. The tracking and calorimeter systems are mostly situated within the solenoid, while the muon systems are on the outside, integrated into the steel return yoke. These subsystems are discussed in the following subsection. One may compare and contrast with the ATLAS experiment's [92] choice of a much smaller central solenoid and complementary toroidal magnet system, particularly with respect to the complexity of the field configurations and the space afforded to the detector subsystems.

4.1.1   The detector subsystems

- **The Muon System** delivers muon information to the level 1 (hardware) trigger system and provides an initial measurement of the muon momentum. Three types of gaseous detector are used, chosen on the basis of the resolution and coverage they can provide: these are Drift Tube (DT) chambers for $|\eta| < 1.2$, Resistive Plate Chamberss (RPCs) for $1.0 < |\eta| < 1.6$ and Cathode Strip Chambers (CSCs) for $1.6 < |\eta| < 2.4$;

- **The Electromagnetic Calorimeter (ECAL)** uses $\sim 75,000$ lead tungstate (PbWO$_4$) crystals to measure the energy of electrons, photons and pions in the detector via the scintillation light they produce in the crystals. The Barrel ECAL covers the region $0.0 < |\eta| < 1.5$ with an angular resolution of $0.087 \, \text{rad.} \times 0.087$ in $\Delta\phi$ and $\Delta\eta$, and uses silicon avalanche photodiodes (APDs) to collect scintillation light. The Endcap ECALs cover the region $1.5 < |\eta| < 3.0$ with a slightly coarser resolution, and use the more radiation-tolerant Vacuum Phototriodes (VPTs). The energy resolution is designed to

be $< 0.5\%$ for e/γ objects with $E \gtrsim 70\,\mathrm{GeV}$. This should allow a diphoton mass resolution of around $1\,\%$, which could be crucial for the low-mass Higgs $H \to \gamma\gamma$ discovery channel [93].

- **The Hadron Calorimeter (HCAL)** uses layers of brass absorber and plastic scintillator tiles with embedded wavelength shifting fibres to measure the energy of hadronic emissions from the Interaction Point. It consists of four parts, the Barrel (HB), the Outer (HO), which sits outside of the solenoid coil, the Endcaps (HE) and the Forward HCAL (HF), which is $11.2\,\mathrm{m}$ from the interaction point, provides coverage for $3 < |\eta| < 5$, and uses steel absorbers and quartz fibre technology.

- **The Inner Tracking System** is designed to track the paths of charged particles in the region defined by a $2.6\,\mathrm{m}$ diameter, $5.8\,\mathrm{m}$ long cylinder centred on the interaction point, providing coverage for $|\eta| < 2.4$. In the region $r < 11\,\mathrm{cm}$, where the particle flux is greatest ($\sim 10^7\,\mathrm{cm^{-2}\,s^{-1}}$), a hybrid pixel detector is used. This has three barrel layers, two endcaps, a total area of $1\,\mathrm{m}^2$ and around 66 million pixels. It provides a resolution of $\sim 10\,\mu\mathrm{m}$ for the $r-\phi$ measurement and about $20\,\mu\mathrm{m}$ for the z measurement, required for τ and b-tagging vertex reconstruction. The Silicon Strip Tracker (SST) uses $200\,\mathrm{m}^2$ of silicon divided into 9.3 million silicon microstrips of varying pitches and lengths chosen to provide the required resolution for the anticipated particle flux in the region $20\,\mathrm{cm} < r < 110\,\mathrm{cm}$.

4.1.2   The trigger, data acquisition and computing systems

Only 100 or so collision events per second can be permanently stored on tape, and so the CMS Trigger and Data Acquisition system (TriDAS) [94, 95] has been designed and implemented to select potentially interesting events at the required rejection rate. It consists of four parts:

- The **Detector Electronics** receive and process the raw signals produced by the detector's sensitive regions. They are either sent to the Level 1 trigger hardware (see below), or are buffered for $3.2\,\mu$m (the *trigger latency*) until a Level 1 trigger signal is received.

- The **Level 1 Trigger Processors** consist of custom, programmable hardware components that make trigger decisions based on *trigger primitives* from the muon, ECAL and HCAL detectors. The Level 1 acceptance rate was designed to be $100\,$kHz.

- The **Readout Network** uses distributed hardware and software components to read data fragments from the hundreds of detector front-end units and build them into complete events, suitable for processing by the next stage in the trigger system. A typical CMS event (the output of the detector system) has a size of $1.5\,$MB.

- The **High-Level Trigger (HLT)** uses a farm of networked processors to apply further selection criteria to the events. This reduces the acceptance rate from $100\,$kHz to $100\,$Hz. Events are rejected as quickly as possible by only performing a partial reconstruction of the detector output.

The CMS SoftWare (CMSSW) software framework aims to process and select events inside the HLT, to deliver the processed results to CMS users, and to provide the tools required for the timely production of physics results from LHC data. In order to do this, a number of requirements were identified in [96], focussing on portability, flexibility and ease of use. To meet these requirements, an application framework using plug-in analysis modules, services and utilities was implemented. This is based around an Event Data Model (EDM), where the focus of any software activity is the *Event*. Different modules are configured for use depending on the reconstruction, selection, simulation, analysis, calibration and alignment functionality needed by the user.

4.2   Jet reconstruction

4.2.1   Decoding the calorimeter output

Having presented an overview of the CMS experiment, one may now turn to the
actual definition of the jets to be used as the atomic unit of the analysis. Salam
et al. describe a jet as "a collimated spray of energetic hadrons" that can be used
to estimate the properties of the original outgoing parton before it fragments and
hadronises [66]. In terms of what is measured by the detector, this analysis uses
a jet definition based entirely upon energy deposits recorded in the calorimeter
subsystems. These are known in the CMS literature as `Calojets` [97]. The CMS
detector has two major calorimeter systems for the $|\eta| < 3.0$ region of pseudo-
rapidity – the ECAL and the HCAL, as described in § 4.1.1 – and it is the energy
deposits recorded in these that are clustered together to make particle jets[1]. Two
other jet reconstruction methods are used by the CMS Collaboration: these are
Jet-Plus-Track (JPT), where tracker information is used to correct individual jet
energies [98]; and Particle Flow (PF), where the reconstruction of individual particles
is attempted before high-level physics object reconstruction is performed [99, 100].
These are not used in the analysis featured here.

Unlike the idealised detector of Chapter 3, the output from two calorimeters is
combined to ensure that as much energy as possible is accounted for from the collision
products. Firstly, thresholds are applied to the individual cells; these are listed for
the different η regions in Table 4.1. Then the cells are geometrically grouped into
"calorimeter towers". In the barrel region ($|\eta| < 1.5$), the unweighted sum of one
single HCAL cell and 5×5 ECAL crystals form a projective tower. In the endcap
region ($1.5 < |\eta| < 3.0$) this projective grouping of cells into towers becomes more

---

[1] The contributions from the forward calorimetry systems that instrument the HF region are
of less importance to this analysis; corresponding kinematic requirements are placed on the jets to
reflect this.

Region	Threshold / GeV
HCAL Barrel (HB)	0.7
HCAL Endcap (HE)	0.8
HCAL Outer (HO) – Ring 0	1.1
HCAL Outer (HO) – Ring 1,2	3.5
HCAL Forward (HF) – long fibre	0.5
HCAL Forward (HF) – short fibre	0.85
ECAL Barrel (EB) – per crystal	0.07
ECAL Endcap (EE) – per crystal	0.3
ECAL Barrel (EB) – sum	0.2
ECAL Endcap (EE) – sum	0.45

Table 4.1: Calorimeter cell energy thresholds used in jet reconstruction [97].

complicated, but follows the same principles. The forward region ($3.0 < |\eta| < 5.0$) is instrumented with a different calorimeter technology (steel absorber with quartz fibre crystals), and so these are considered separately[2].

The jet reconstruction procedure then follows that used in the toy analysis of Chapter 3, with the calorimeter towers taking the place of individual cells. Each tower is associated with a massless 4-momentum with a magnitude corresponding to the tower energy, and a direction corresponding to the tower position as seen from the Interaction Point. The anti-k_T algorithm with $R = 0.5$ is used to cluster the towers together, and the individual tower 4-momenta are recombined with the E scheme to produce the `Calojet` candidates for a given event.

As touched upon in Chapter 3, there are many potential sources of mismeasurement due to imperfections in the instrumentation. Correcting for the calorimeter's response to actual jets is discussed in the following subsection, but mismeasurements caused by spurious detector signals must also be dealt with. For example, non-jet signals in the calorimeters – from beam halo, cosmic rays, or noise from the readout

---

[2] This is also why only jets with $|\eta| < 3.0$ are considered in the final analysis; see § 5.1 for further details.

electronics – may lead to "fake" jets being reconstructed. To prevent this, a set of quality criteria that exploit the information available from the different calorimeters have been defined based on data collected from cosmic ray runs, minimum bias samples and detector readout during LHC abort gaps [101]. These are as follows:

- The fraction of jet energy contributed by ECAL energy deposits, f_{EM}: typically, jets of interest will consist of some electromagnetic activity. While $f_{\mathrm{EM}} \sim 0$ for a jet is not impossible, it is often suggestive of a signal caused by pure HCAL noise. A minimum requirement on f_{EM} is therefore imposed on `Calojets` in the fiducial region of the ECAL ($|\eta| < 2.6$).

- The minimum number of clustered ECAL and HCAL cells that contain 90% of the jet energy, N_{cells}^{90}: use of this variable guards against jets that are due to single noisy cells, typically by requiring a value of at least two for the candidate jet.

- The fraction of energy contributed by the highest energy Hybrid Photo-Diode (HPD) readout, f_{HPD}: the HCAL readout electronics were observed to contribute noise in multiple cells attached to the same readout chain. A maximum limit on f_{HPD} for a given jet candidate has been shown to satisfactorily reject fakes.

- In the forward regions ($|\eta| > 3.0$), which are not instrumented by the ECAL, the energy contributed by the short quartz fibres minus the contribution from the long quartz fibres divided by the total energy, $R_{\mathrm{HF}} = (E_{\mathrm{S}} - E_{\mathrm{L}})/(E_{\mathrm{S}} + E_{\mathrm{L}})$, is used in a similar way to f_{EM} (signals from the short fibres correspond to electromagnetic activity, since most of the energy from photons and electrons will be deposited in the region corresponding to the short fibres). Again, it is noted that jets with $|\eta| > 3.0$ are not used in this analysis.

These variables are used to define "jet identification" or `JetID` criteria which have been used by many of the `Calojet`-based analyses carried out by the CMS Collaboration. The "loose" jet identification criteria may be found in Table 4.2; further details and motivational plots may be found in [101].

Variable		Value	Notes
f_{EM}	$>$	0.01	Jets in HB, BE, HE regions.
N^{90}_{cells}	$>$	1	
f_{HPD}	$<$	0.98	
R_{HF}	$>$	-0.9	Jets in HF region.
R_{HF}	$<$	1.0	Jets in HF region with $p_{\mathrm{raw}} > 80\,\mathrm{GeV}$.

Table 4.2: "Loose" jet identification criteria, as suggested by [101].

4.2.2 Jet energy corrections and uncertainties

Once the clustered energy from the cells has been added together, assigned a direction according to the recombination scheme of choice, and has been shown to meet the required jet identification requirements, an energy correction is applied to compensate for deficiencies in the calorimeters. Noise, stochastic effects, muon punch-through and pile-up contributions can result in mismeasurements of the jet energy. To correct for these effects on a jet-by-jet basis, the Jet Energy Corrections (JEC) scheme described in [102] assigns a relative (absolute) to the jet energy that is dependent on the pseudo-rapidity (transverse momentum) of the jet[3]. The correction for a given jet is applied as a multiplicative factor $C(p_{\mathrm{raw}}, \eta)$ on each component of the raw jet 4-momentum P^{μ}_{raw},

$$P^{\mu}_{\mathrm{corr.}} = C(p_{\mathrm{raw}}, \eta)\, P^{\mu}_{\mathrm{raw}}. \tag{4.1}$$

---

[3] It is worth noting that these corrections are based on estimators derived from studies based on both simulations and data, and so a jet can, in principle, be "corrected" to what may not have been its true energy. This is why event-by-event mismeasurement strategies and variables such as α_T are also required, particularly in searches with early data.

The reconstructed jets are first calibrated with a Monte Carlo-derived truth correction before small residual corrections, based on in-situ measurements of the relative (η) and the absolute (p) jet energy scale, are applied. The data used for the JEC scheme in this analysis corresponds to the results reported in [102], which used $\sim 3 \, \mathrm{pb}^{-1}$ (`Spring10v2`)[4]. Considering each of these steps in a little more detail:

- Monte Carlo truth jet energy corrections are derived using simulated QCD events from proton-proton collisions at $\sqrt{s} = 7 \, \mathrm{TeV}$. Generator-level collision products are clustered to form `Genjets` that are matched to the reconstructed `Calojets` by requiring $\Delta R < 0.25$. For the matched jets, the quantity $p_{\mathrm{reco.}}/p_{\mathrm{gen..}}$ is recorded in bins of $p_{\mathrm{gen..}}$ and is used to calculate a correction factor as a function of $p_{\mathrm{reco.}}$ and η. Figure 4.2 plots the correction factor as a function of η for `Calojets` in three p_{raw} bins. The structure in η is a result
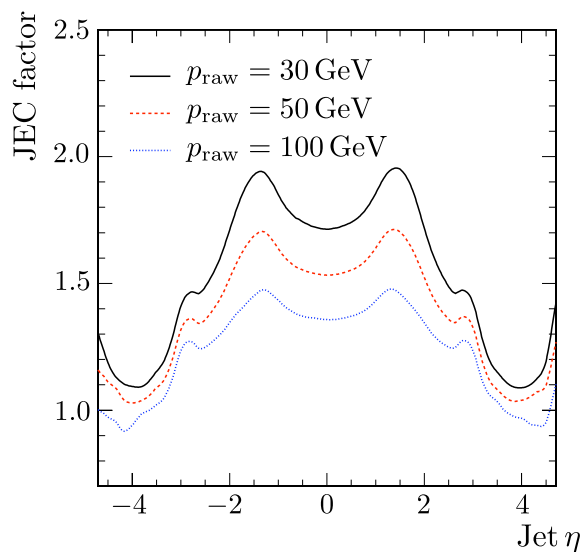
Figure 4.2: JEC factor as a function of jet pseudo-rapidity from $7 \, \mathrm{TeV}$ simulations, for anti-k_T $R = 0.5$ `Calojets`. Taken from [97].

of the differing instrumentation in the η regions. Correction factors at larger η are smaller for `Calojets` because a fixed p corresponds to a larger energy

---

[4] Jet corrections and resolution measurements corresponding to the full 2010 dataset ($36 \, \mathrm{pb}^{-1}$) were reported in [103]. Obviously, the all-hadronic analysis featured here could not use these results at the time.

at larger η. The greater the jet energy, the better the calorimeter response is, and so the required correction factor is smaller than those for JPT or PF jets.

- A residual correction is then applied based on measurements in data; the dijet p_T balance technique, first used at the SP$\bar{\text{P}}$S [104] and refined at the Tevatron [105, 106], is deployed to calculate a relative energy correction as a function of jet η. Further details may be found in [107], and the relevant results for this analysis may be found in [97].

- An absolute energy corrections, determined as a function of p_{raw}, is then applied based on $\gamma +$ jet data obtained in a $|\eta| < 1.3$ reference region of the detector. The Missing E_T Projection Fraction (MPF) method [108] is used to determine the absolute correction factors; the p_T balance method is used (with the photon taking the place of the second jet) to provide a secondary estimate of the correction factors and to help understand the systematic uncertainties. Further details may be found in [109], and the relevant results for this analysis may be found in [97].

The corrections from all of these stages are combined to produce the total JEC factors as a function of p_{raw} and η. For illustrative purposes, Figure 4.3 shows the correction factors as a function of $|\eta|$ for jets in the $p_{\text{raw}} = 50\,\text{GeV}$ and $200\,\text{GeV}$ bins, and Figure 4.4 shows the corresponding uncertainties on those correction factors. The uncertainties from JECs are taken as being between 2% and 5% for the `Calojet`-based analysis presented in Chapter 5, based on the $\sim 3\,\text{pb}^{-1}$ of data used in [102][5].

---

[5] The non-gaussian response of the calorimeters, and attempts to measure the jet resolution, was reported in [110] and [103]. These studies required $36\,\text{pb}^{-1}$ of data and so the results were not used in the featured all-hadronic α_T analysis. Of course, the α_T strategy is designed in such a way that it does not require this information.

(a) $p_{\mathrm{raw}} = 50\,\mathrm{GeV}$.   **(b)** $p_{\mathrm{raw}} = 200\,\mathrm{GeV}$.
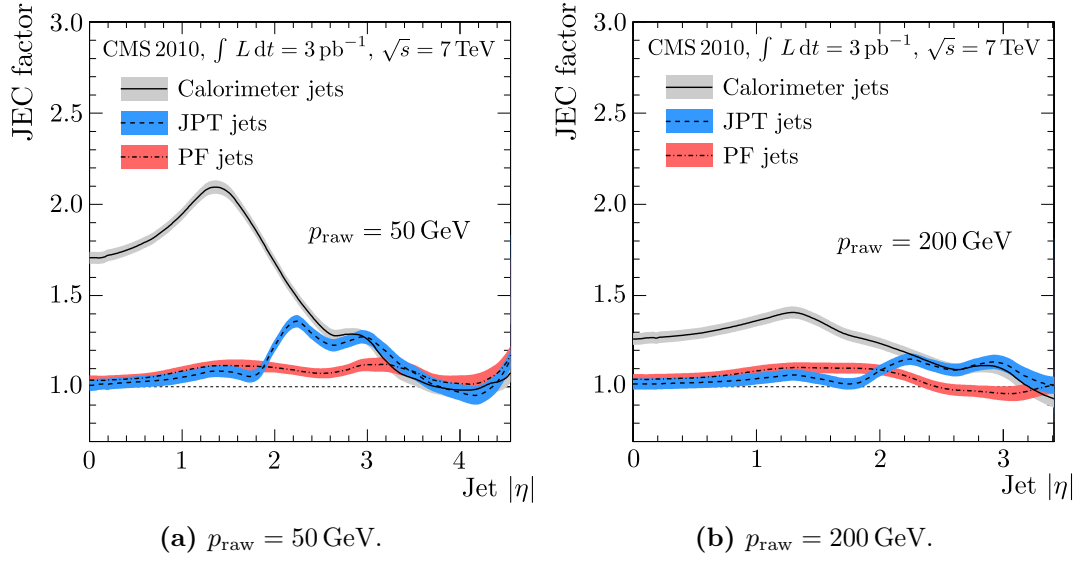
Figure 4.3: Total JEC factor as a function of jet pseudo-rapidity for anti-k_T, $R = 0.5$ jets ($3\,\mathrm{pb}^{-1}$). Taken from [102].

(a) $p_{\mathrm{raw}} = 50\,\mathrm{GeV}$.   **(b)** $p_{\mathrm{raw}} = 200\,\mathrm{GeV}$.
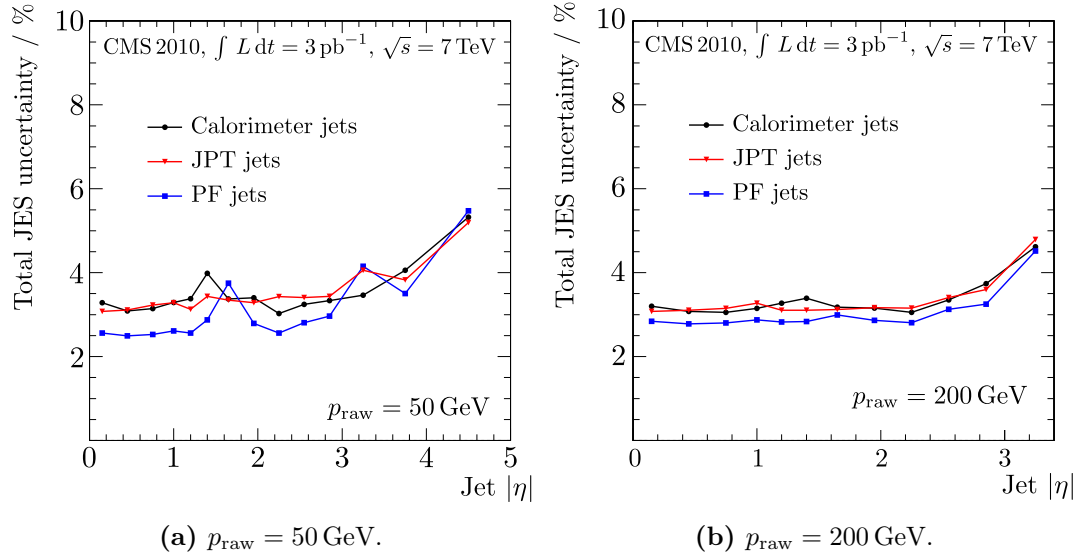
Figure 4.4: Total JES uncertainty as a function of jet pseudo-rapidity for anti-k_T, $R = 0.5$ jets ($3\,\mathrm{pb}^{-1}$). Taken from [102].

4.3   Reconstructing other physics objects

The focus of this particular analysis is on final states featuring only particle jets. Events containing isolated photons, electrons or muons are removed for two reasons. Firstly, the presence of these objects in the final state suggests that some sort of electroweak activity may have taken place. In the case of W decay, the accompanying neutrino will generate real missing transverse momentum, making such events an irreducible background in a $\not{p}$-based search. Vetoing events featuring leptons is therefore a useful way of removing this irreducible background.

Secondly, one may consider the wider picture of the search for supersymmetry. As discussed in § 2.3.3, a wide range of final state topologies is possible due to the nature of the sparticle decay chains. Thus it is useful to categorise events passing the trigger requirements in terms of their physics object content. This ensures that complementary analyses performed using the same data and based upon differing final state topologies contain orthogonal subsets of events and so may be safely conducted in parallel, allowing different regions of parameter space to be probed simultaneously[6].

It is therefore necessary to be able to reconstruct and identify these other physics objects using all available detector information. The all-hadronic α_T analysis has used procedures borrowed from other CMS physics analyses; this ensures consistency and aids communication across the collaboration, as well as preventing the reinvention of multiple physics wheels.

Generally speaking, candidate physics objects are required to pass a minimum transverse momentum cut, fall within a specified pseudo-rapidity range, be suitably iso-

---

[6] Events featuring isolated photons in the final state are considered separately for the additional reason that R-parity conserving supersymmetry models with a gravitino LSP can result in events with two photons in the final state. The Gauge-Mediated Supersymmetry Breaking (GMSB) model mentioned in Chapter 2 is an example of such a model [54, 55, 56, 57].

lated from other detector signals, and meet detector-specific identification require-
ments similar to those outlined for `CaloJets` in § 4.2. The reconstruction criteria
for photons, electrons and muons are described in the following subsections. The
tau lepton identification procedures were not considered mature enough to use in
this early search, and so tau leptons were not considered in the set of final state
topologies. It was assumed that any tau leptons produced would be considered as
jets (for hadronic decay modes) or be excluded by the lepton veto (for the leptonic
decay modes).

4.3.1   Photon reconstruction

The photon reconstruction and identification used in the work presented here is
based on that used by the (complementary) diphoton $+\,\not{p}$ search for GMSB [111,
112], which in turn built on the foundations laid in the photon commissioning work
reported in [113]. Photon reconstruction is seeded with "superclusters" of ECAL
energy deposits formed using the hybrid algorithm described in [93]; the following
quality criteria are used to select candidates that actually correspond to isolated
photons:

- ECAL isolation: the scalar sum of the transverse energies in a hollow cone of
  radius $0.06 < \Delta R < 0.4$ (hollow to avoid counting the transverse energy of
  the photon candidate itself, e_γ) is required to be less than fraction of e_γ plus
  a constant;

- HCAL isolation: a similar isolation requirement is placed upon the HCAL
  deposits in a hollow cone of radius $0.15 < \Delta R < 0.4$ (hadronic energy in the
  inner cone is accounted for with the H/E cut described below);

- Track isolation: tracks incident on the surface of the ECAL within a hollow
  cone of radius $0.04 < \Delta R < 0.4$ are required to have a scalar transverse

momenta sum of less than a specific fraction of the e_γ plus a constant. A hollow cone is used to account for photon conversions away from the Interaction Point;

- A shower-shape variable, $\sigma_{i\eta i\eta}$, is used to gain a handle on the extent of the electromagnetic shower in η ($\sigma_{i\eta i\eta}$ is the $\eta-\eta$ element of the supercluster's $\phi-\eta$ covariance matrix). Different cut values are required for photons reconstructed in the barrel (EB) and the endcap (EE);

- Finally, a limit is placed upon the ratio of energy measured by the HCAL to the energy in the supercluster.

Valriable		Value
ECAL isolation	$<$	$4.2 + 0.0060\, e_\gamma \,\mathrm{GeV}$
HCAL isolation	$<$	$2.2 + 0.0025\, e_\gamma \,\mathrm{GeV}$
Track isolation	$<$	$2.0 + 0.0010\, e_\gamma \,\mathrm{GeV}$
η width ($\sigma_{i\eta i\eta}$)	$<$	$0.013\,(\mathrm{EE}),\ 0.030\,(\mathrm{EB})$
Hadronic / EM	$<$	0.05

Table 4.3: The "tight" photon isolation and identification criteria. EB and EE refer to the values applied to photons found in the barrel and endcaps of the electromagnetic calorimeter respectively [111, 112].

The "tight" photon identification requirements described by [111] are listed in Table 4.3. Motivating plots for the chosen cut values can be found in [113]. It should also be noted that photon candidates that fall in the gap between the ECAL barrel and endcap ($1.4442 < |\eta| < 1.566$) are rejected outright due to the lack of instrumentation in this pseudo-rapidity region.

4.3.2   Electron reconstruction

The electron reconstruction and identification procedure used here is based upon that used by the vector boson-based CMS physics analyses; specifically, the work

reported in [114, 115] which in turn built upon the first 7 TeV electron commissioning studies reported in [116]. As both physics objects are largely based on electromagnetic activity in the detector subsystems, the electron reconstruction process is similar in some ways to that used for photons. The charged nature of electrons makes the information from the silicon tracker subsystems more relevant. Superclusters in the ECAL are used to seed electron candidates, and both reconstructed tracks and *bremsstrahlung* are used to distinguish these from photons and other non-electron objects.

In [114, 115] a number of electron identification schemes are defined in terms of the efficiency required by the user. These are named "WPXX", where "XX" is the desired efficiency expressed as a percentage. The variables associated with these schemes are:

- Isolation: rather than place limits on the isolation from individual detector subsystems, the WPXX schemes allow the user to instead use a "combined isolation" $I_{\text{comb.}}$ defined as

$$I_{\text{comb.}} = \left\{ \sum_{\text{Trk.}} p + \sum_{\text{ECAL}} e + \sum_{\text{HCAL}} e \right\}_{\Delta R < 0.3} / p_e, \qquad (4.2)$$

  where the respective isolation quantities are calculated from the scalar sum of the tracks/deposits in a cone of radius $\Delta R < 0.3$, and p_e is the transverse momentum of the electron;

- Requirements on the angular separations in ϕ and η of the closest reconstructed track projected onto the ECAL supercluster, $\Delta \phi_{\text{in}}$ and $\Delta \eta_{\text{in}}$, are used to suppress fake electrons by ensuring that the supercluster has a closely associated track;

- $\sigma_{i\eta i\eta}$ and H / E as defined for the photon are also used to obtain ECAL superclusters that have the appropriate shape and energy composition.

Variable		WP95		WP80	
		EB	EE	EB	EE
$\Delta\phi_{\text{in}}$	$<$	n/a	n/a	0.06	0.03
$\Delta\eta_{\text{in}}$	$<$	0.007	0.01	0.004	0.007
$\sigma_{i\eta i\eta}$	$<$	0.01	0.03	0.01	0.03
H / E	$<$	0.15	0.07	0.04	0.025

Table 4.4: Electron identification criteria for the WP95 and WP80 schemes [114, 115, 116]. EB and EE refer to the values applied to electrons found in the barrel ($|\eta| < 1.4442$) and endcaps ($1.566 < |\eta| < 2.5$) of the electromagnetic calorimeter respectively. Electrons outside of the acceptance ranges in η are rejected.

Table 4.4 shows the values of these variables used in the WP95 scheme, as well as those used in the WP80 scheme for comparison. Further discussion of the criteria, as well as plots and studies used to motivate the chosen values, can be found in [115].

4.3.3   Muon reconstruction

The muon reconstruction and identification procedure used here is based upon that used by the vector boson-based CMS physics analyses; specifically the work reported in [114, 115], which in turn built upon the first 7 TeV muon commissioning studies reported in [116] and the cosmic ray studies reported in [117].

Two approaches are used to reconstruct muons from the tracker and muon detector subsystems: *global muons* consist of tracker and muon information combined after reconstruction is performed; while *tracker muons* combine low-level detector information at an earlier stage in the reconstruction process. Additionally, the following criteria are used to reject fake and non-prompt muons from consideration:

- Global (tracker) muons must have at least one (two) good hit (hits) in the muon chambers;

- A minimum requirement is placed upon the number of hits in recorded in the tracker for the track associated with the muon;

- Non-prompt muons can be rejected with a cut on the transverse distance of the closest spproach of the muon track to the beam axis, D_{xy};

- A global fit on the tracker and muon chamber information is also performed for each muon; a limit on the χ^2 per degree of freedom serves as an additional measure of quality;

- The combined relative isolation $I_{\text{comb.}}$ (Equation 4.2) can be used to identify isolated muons.

Variable		"Loose"	"Tight"
Global muon		Yes	Yes
Tracker muon		No	Yes
Valid hits in the muon chambers	$\geq$	n/a	1
Valid hits in tracker	$>$	n/a	10
Transverse distance to beam axis, D_{xy}	$<$	n/a	$2\,\text{mm}$
χ^2 global track fit	$<$	n/a	10.0

Table 4.5: Muon identification criteria for "Loose" and "Tight" muons, based on the requirements defined in [115, 117, 118].

Table 4.5 shows the values of these variables used to define "loose" and "tight" muons[7]. Further discussion of the criteria, as well as plots and studies used to motivate the chosen values, can be found in [115].

---

[7] These are also known as `Global` and `GlobalPromptTight` (respectively) in the CMS literature.

Chapter 5

The CMS All-hadronic Search for Supersymmetry

"The aim of science is not to open the door to infinite wisdom,
but to set a limit to infinite error."

Bertolt Brecht, *The Life of Galileo (1939)*

The search strategy used in the "Search for supersymmetry in pp collisions at $7\,\text{TeV}$ in events with jets and missing energy" [18] is now described. The preselection and selection criteria used to identify potentially interesting and candidate signal events are outlined in § 5.1. This includes the steps taken to obtain an all-hadronic data set, using the physics object reconstruction and identification techniques discussed in Chapter 4. The data-driven methods used to predict the contribution of irreducible background processes to the signal region are summarised in § 5.2, and finally the results of the analysis and the constraints they place upon the supersymmetric parameter space are presented in § 5.3. The author was mainly involved in the work pertaining to the first section of the analysis presented here; the final two sections are summarised for completeness and the convenience of the reader. Full details of these parts of the analysis may be found in [18, 119, 120].

5.1   The search strategy: event selection

It is now time to define the signal region for the all-hadronic analysis, and present the results from this search. After specifying the trigger requirements in § 5.1.1, the procedure used to obtain a data set featuring only events with particle jets in the final state is described in § 5.1.2. One may then consider the preselection (what makes an event potentially interesting, § 5.1.3) and the selection (what defines a signal event candidate, § 5.1.4) criteria for the all-hadronic channel. This is done in the context of extending the toy analysis strategy of § 3.2 to the full CMS detector.

As one would expect, the additional information afforded by the different detector subsystems, and the complexities it introduces, demands a more sophisticated approach than that used in Chapter 3. Nevertheless, the cornerstone of the analysis remains the rejection of mismeasured backgrounds with the discriminating variable α_T, which was shown in Chapter 3 to be robust against detector energy mismeasurement.

5.1.1   Triggering

The CMS Level 1 Trigger and HLT systems (§ 4.1.2) provide a wide selection of triggers that offer an initial indication that something worthy of further analysis has taken place in a proton-proton collision. The requirements of this analysis are, however, very simple: events of potential interest should, according to the simulated signal samples, produce a large amount of transverse energy. Σh (or H_T) triggers are used at L1 and in the HLT algorithms to initially qualify candidate events to be considered in the offline reconstruction and analysis. Specifically, the `HLH_HT150U` trigger is used in the analysis presented here, selecting events featuring HLT jets (Iterative Cone with 0.5 radius, uncorrected transverse energy $e > 20\,\mathrm{GeV}$) with a scalar transverse energy sum $\Sigma h > 150\,\mathrm{GeV}$. In the very early stages of data

taking, triggers with lower Σh thresholds were used without a prescale factor. Where possible, the lowest unprescaled Σh trigger was used.

The fact that the HLT jets do not have corrections to their measured energy to account for detector mismeasurements is important when considering the trigger efficiency. To check that efficiency is not an issue for the analysis, the turn-on curves for several Σh thresholds with respect to the (corrected) Σh calculated from the offline jet selection (described in the next subsection) are plotted in Figure 5.1. `HLH_HT150U` is 100% efficient when $\Sigma h > 235\,\mathrm{GeV}$ in the case of 50 GeV (corrected)

(a) HLT jet threshold 50 GeV.   **(b)** HLT jet threshold 35 GeV.
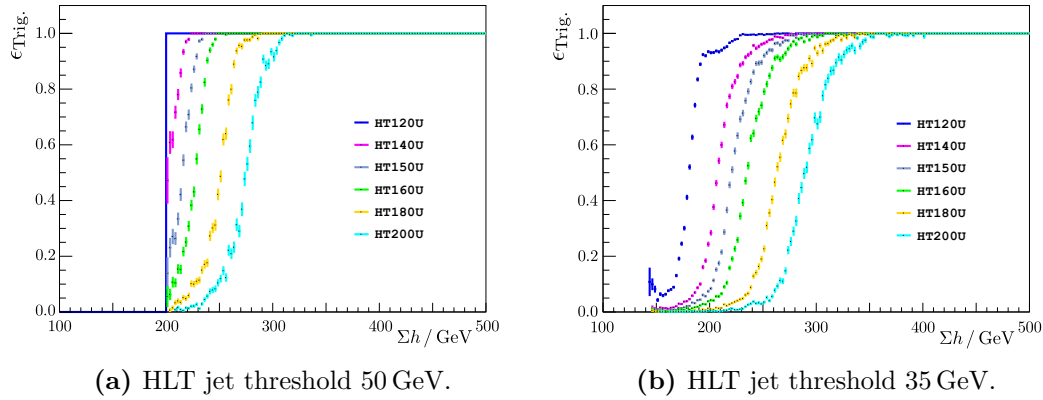
Figure 5.1: Turn-on curves for a selection of Σh HLT triggers, showing the efficiency as a function of offline reconstructed Σh. Taken from [120].

jet thresholds. For a (corrected) jet threshold of 35 GeV, the `HLH_HT150U` trigger is 94% efficient at $\Sigma h > 250\,\mathrm{GeV}$ (the lower bound of the lowest Σh control region defined in § 5.2.1), but becomes 100% efficient when $\Sigma h > 285\,\mathrm{GeV}$.

5.1.2   Defining the all-hadronic channel

As discussed in Chapter 1 and § 4.3, the all-hadronic analysis requires a final state featuring only particle jets. This requirement necessitates the use of a mechanism for unambiguously describing an event as containing N^j jets, N^e electrons, N^μ muons and N^γ photons. This is achieved by firstly "cross-cleaning" the physics objects

supplied by the offline reconstruction, to resolve conflicts between overlapping objects and to avoid the double-counting of energy deposits. As noted in Chapter 4, the CMS offline reconstruction techniques employ a plethora of largely independent mechanisms for the identification of the physics objects present in the final state, i.e. the jets, leptons and photons. It is therefore feasible for a given energy deposit as read from a detector subsystem to be identified as two different objects; for example, a suitably isolated deposit in the electromagnetic calorimeter may be interpreted as both a jet *and* a photon. It is therefore necessary to apply some form of object cleaning to the collections of reconstructed objects to avoid the double-counting of these energy deposits. This is what is known as *cross-cleaning*[1].
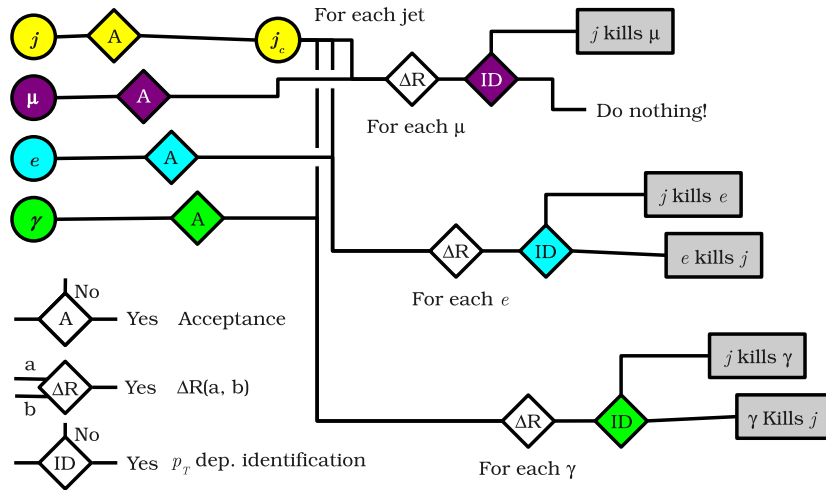
Figure 5.2: A flow diagram representing the cross-cleaning procedure used in the early CMS supersymmetry searches. The "A" decision block represents the acceptance cuts on the candidate p and $|\eta|$. The "ΔR decision block takes two input objects and represents whether or not they are deemed to overlap in $\phi - \eta$ space. The "ID" decision box represents whether the object (of the corresponding colour in the diagram) passes the identification and isolation requirements described in the text.

The cross-cleaning process, illustrated in Figure 5.2, is defined as follows: firstly, objects (jets, photons, electrons and muons) failing a minimum transverse momentum cut ($10\,\text{GeV}$, $25\,\text{GeV}$, $10\,\text{GeV}$, and $10\,\text{GeV}$) and a maximum absolute pseudo-rapidity cut (5.0, 2.5, 2.5, and 2.5) are filtered out and discarded from the event.

---

[1] Physics objects identified using *particle flow* [99, 100] do not require additional cross-cleaning, as a form of cross-cleaning is built into the Particle Flow algorithm itself.

Objects that are found to overlap (i.e. are within $\Delta R = \sqrt{\Delta \phi^2 + \Delta \phi^2} < 0.5$ of each other) are then cleaned using the following prescriptions:

- **Jet-photon cross-cleaning**: a "tight" photon (see § 4.3.1) will remove the overlapping jet; otherwise, the non-isolated or unidentified photon will be removed by the overlapping jet;

- **Jet-electron cross-cleaning**: an electron meeting the WP95 identification criteria (see § 4.3.2) with a combined relative isolation of $I_{\mathrm{comb.}} < 0.15$ will remove the overlapping jet; otherwise, the non-isolated or unidentified electron will be removed by the overlapping jet;

- **Jet-muon cross-cleaning**: if the combined isolation of the candidate (global) muon is $I_{\mathrm{comb.}} < 0.15$, the muon is considered to be isolated. If the muon is deemed not to be isolated and is identified as "tight" (see § 4.3.3), the muon considered to be a part of the jet. The 4-momentum of the muon is added to that of the jet and the muon candidate is removed;

- **Electron-photon cross-cleaning**: electron-photon cleaning was deemed unnecessary for the purposes of the all-hadronic analysis, as the presence of either object would result in the event being discarded.

The standard object definitions described in § 4.2 and § 4.3 are then applied to the cross-cleaned physics object candidates. Jets were required to have $p > 50\,\mathrm{GeV}$, $|\eta| < 3.0$ and meet the loose `JetID` criteria. Photons were required to have $p > 25\,\mathrm{GeV}$, $|\eta| < 2.5$ and meet the "tight" photon criteria. Electrons were required to have $p > 10\,\mathrm{GeV}$, $|\eta| < 2.5$, $I_{\mathrm{comb.}} < 0.15$ and meet the "WP95" criteria. Muons were required to have $p > 10\,\mathrm{GeV}$, $|\eta| < 2.5$ and meet the "tight" (`GlobalPromptTight`) muon identification criteria.

Applying these definitions, a given event may then be said to contain N^j jets, N^e electrons, N^μ muons, and N^γ photons. Each event is then categorised based upon the number of jets, electrons, muons and photons it contains that pass the quality cuts. To be explicit, the analysis presented in [18] and described here only accepts events with

$$N^\gamma = N^e = N^\mu = 0 \quad \text{and} \quad N^j \geq 2. \tag{5.1}$$

In other words, events that do not satisfy Equation 5.1 are vetoed and removed from the analysis chain. (In fact, the physics object vetoes are applied after some intitial "clean-up" event vetoes; see § 5.1.3.)

To ensure that the cross-cleaning and object identification procedures were applied consistently across the gamut of supersymmetry analysis channels, a software framework independent of CMSSW was developed. In order to ensure that the cross-cleaning and physics object-based event veto procedures were consistently applied across the gamut of analysis channels, an independent software framework was developed to run on `ROOT` [121] ntuples made from skims of the CMSSW data sets. Two versions were used in the lifetime of the analysis presented here: the first was a standalone `C++` framework and the second featured `C++` modules (for performance) wrapped in a `Python` interface (for ease of use). The author was heavily involved in the development and maintenance of this framework, which was used by many members of the CMS SUSY group in their respective analyses.

5.1.3   Event pre-selection

Before considering the kinematic characteristics of the jets in the event, the following event vetoes are applied to events passing the `HLH_HT150U` trigger:

- **Vertex selection**: at least one "good" collision vertex is required [122]. These are vertices with more than four degrees of freedom ($N_{\mathrm{dof}} > 4$) and a distance along the beam direction of $< 24\,\mathrm{cm}$ and perpendicular distance to the beam of $< 2\,\mathrm{cm}$. Furthermore, events containing a large number of "fake" tracks compared to the number of `HighPurity` tracks (greater than 25% in events with 10 or more tracks) are rejected;

- **HCAL noise**: events deemed to contain spurious signals from the HCAL detector subsystem even before jet reconstruction is performed are rejected [123];

- **Lepton and photon vetoes**: events containing leptons or photons meeting the p, η and identification requirements specified in § 5.1.2 are rejected. Furthermore, events that have at least one "loose" (global) muon which passes the muon p and η requirements, but is *not* identified as `GlobalPromptTight`, are rejected;

- **Muons in jets**: events that feature a jet that has been modified by a muon in the cross-cleaning procedure, where the muon p is more than 50% of the unmodified jet p, are rejected. This is to protect against jet energy measurement errors caused by bad information from non-calorimeter subsystems;

- **"Odd" jet veto**: events that have a jet with $e > 50\,\mathrm{GeV}$ fails the quality criteria or the $|\eta|$ requirement are rejected to exclude potentially troublesome energy clusters.

The filtered events are then subjected to the same additional kinematic requirements as those in the toy analysis, following the same line of reasoning: the two leading jets (by e) must have $e > 100\,\mathrm{GeV}$ and the leading jet must have $|\eta| < 2.5$ (again, as in the toy analysis). The sum of the jet transverse energies Σh (also known as H_T in the literature) for events meeting all of the above preselection criteria is plotted in Figure 5.3 for the $35.1\,\mathrm{pb}^{-1}$ data sample.
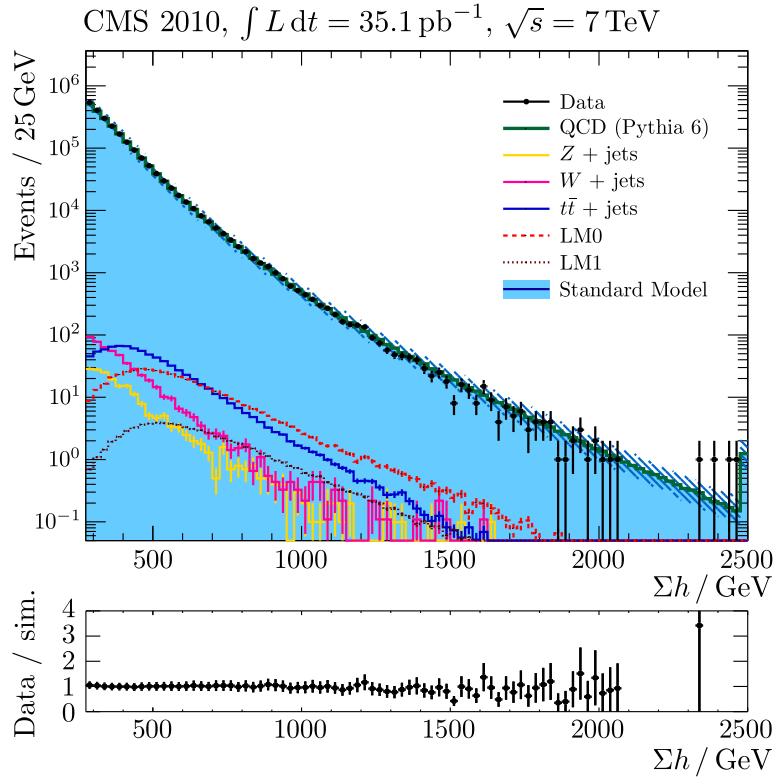
Figure 5.3: Sum of the jet transverse energies for the $35.1\,\mathrm{pb}^{-1}$ data sample. Taken from [120].

The QCD background is estimated using the `PYTHIA 6.4` [77] generator with tune `Z2` [124], electroweak backgrounds from W, $Z \to \nu\bar{\nu}$ and $t\bar{t}$ + jets events are simulated using `MadGraph 4` [81]. In addition, the SM distribution, i.e. the sum of the QCD, W, $Z \to \nu\bar{\nu}$ and $t\bar{t}$ + jets distributions, is shown and the hatched band represents the combined statistical and systematic uncertainty from jet energy scale and resolution. The expected Σh distributions for two low-mass SUSY signal points, LM0 and LM1 are overlaid. With the exception of $t\bar{t}$, the SM processes fall off exponentially with increasing Σh, whereas a broad peak at values of a few hundred GeV is observed for the signal models. An additional preselection requirement of $\Sigma h > 350\,\mathrm{GeV}$ is therefore imposed on the candidate events. As was the case in the toy analysis, this requirement substantially reduces the contributions from SM processes while keeping the majority of supersymmetric topologies considered in this search. The jet multiplicity and missing transverse momentum of the vectorially-summed clusters $\not{h}$ (also known as $\not{H}_T$) are plotted in Figures 5.4 and 5.5 respectively.
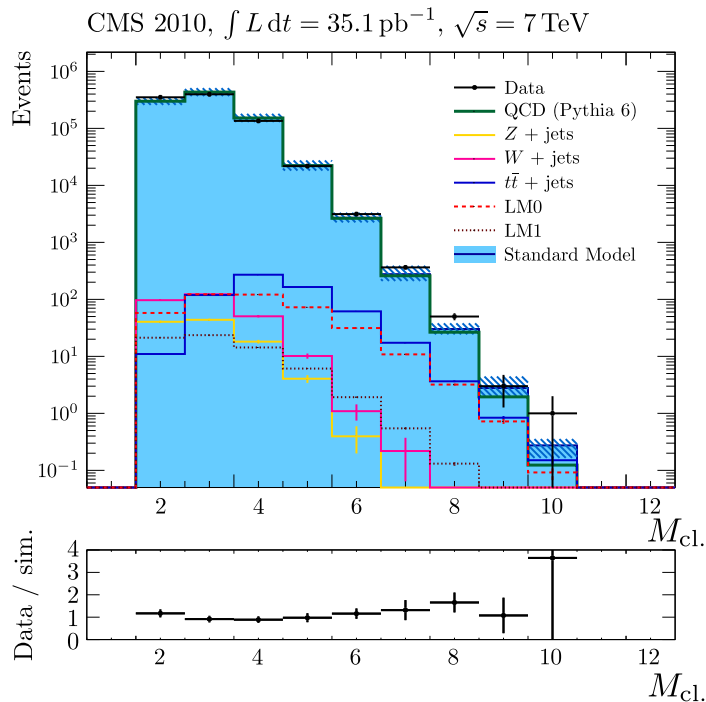
Figure 5.4: Jet multiplicity distribution for the $35.1 \, \text{pb}^{-1}$ data sample. Taken from [120].

The agreement between data and simulation is good for the multiplicity, but a larger discrepancy is observed for the $\not{H}$ distributions. Studies were carried out to investigate the over-estimation of the jet resolution in the simulated samples by smearing reconstructed jets with $e > 100 \, \text{GeV}$ and $|\eta| < 1.4$ using 10% gaussian smearing. While this was found to explain the differences to an extent, it is important to note that the final results presented do not depend on such variations as the background predictions are taken from control samples.

5.1.4 Final event selection

Having identified potentially interesting events from the data sample with the pre-election criteria described above, events could now be selected as signal candidates. α_T was used as the primary discriminating variable and an outcome of $\alpha_T > 0.55$ results in that event counting towards the number of signal events s. The α_T distributions for $N^j = 2$ and $N^j \geq 3$ are plotted in Figures 5.6 and 5.7 respectively.
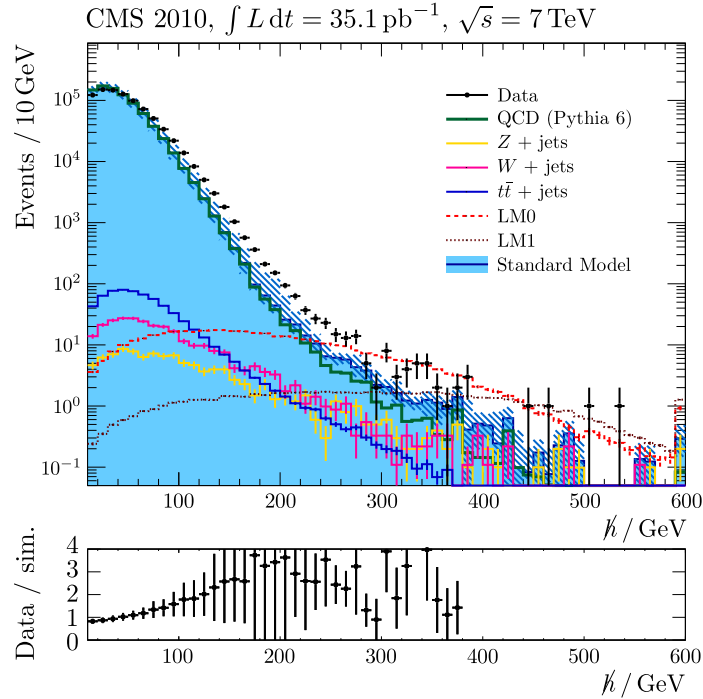
Figure 5.5: Missing transverse momentum as calculated from selected clusters, $\not{h}$, for the $35.1\,\text{pb}^{-1}$ data sample. Taken from [120].

As anticipated, and as demonstrated in the toy analysis, these distributions peak at $\alpha_T = 0.5$ for QCD multijet events and then fall sharply in the range $0.5 < \alpha_T < 0.55$, reaching a level $4 - 5$ orders of magnitude lower than the peak value. Given the requirement $\Sigma h > 350\,\text{GeV}$, the 0.55 cut value on α_T is equivalent to demanding $\not{h}/\Sigma h > 0.42 \sim 0.4$, i.e. $\not{h} > 140\,\text{GeV}$, if and only if the jets conspire to balance in such a way that $\Delta h \to 0\,\text{GeV}$.

Two auxiliary cuts were implemented after the α_T cut. The first of these aimed to account for a known deficiency in the measurement system: masked channels in the ECAL subsystem (about 1% of all channels) were found to cause severe mismeasurements. To reject this kind of event, $\not{h}$ was recomputed using all of the candidate jets bar one. The difference in azimuth between the recomputed $\not{h}$ and the ignored jet is then calculated, and the minimum of these values, $\Delta\phi^*$, is used to identify the jet that is likely to have generated fake $\not{p}$ from a single mismeasurement. Events with $\Delta\phi^* < 0.5$ (i.e. those with a strong chance of fake $\not{p}$ due to a single
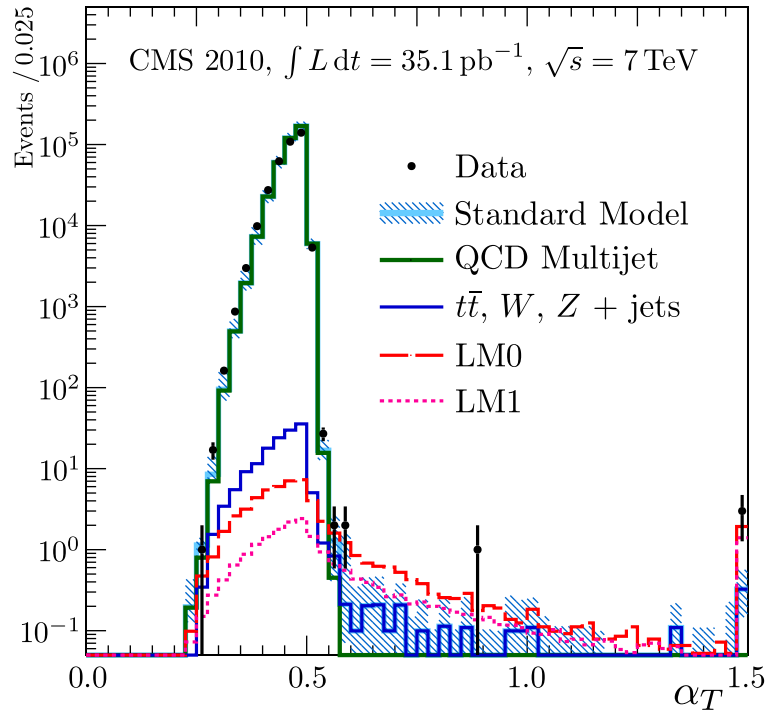
Figure 5.6: α_T distribution for the dijet topology, $35.1\,\text{pb}^{-1}$ of data. Taken from [18].
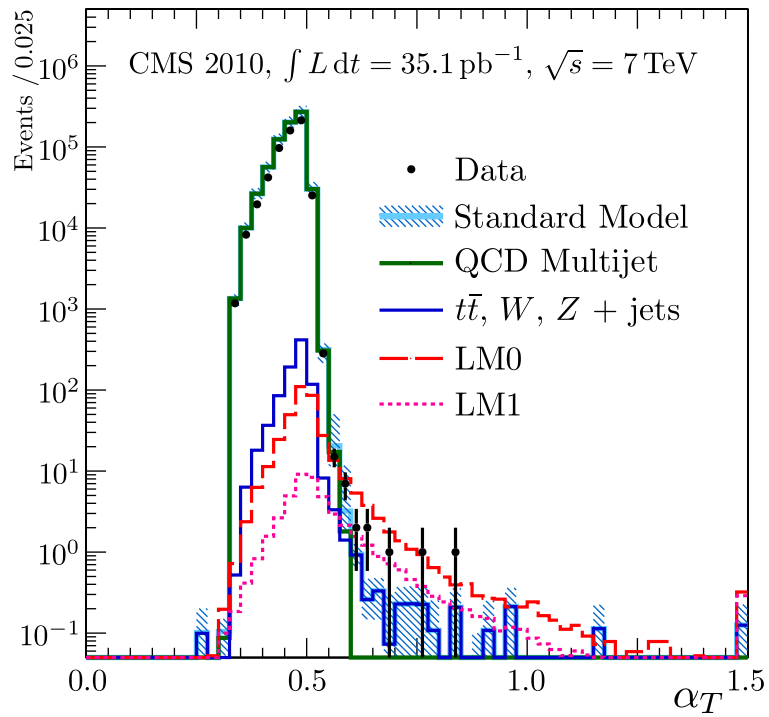
Figure 5.7: α_T distribution for the multijet topology, $35.1\,\text{pb}^{-1}$ of data. Taken from [18].

jet mismeasurement) are rejected if the distance in the $(\eta, \Delta\phi)$ plane between the selected jet and the closest masked ECAL region, ΔR_{ECAL}, is smaller than 0.3.

The second auxiliary cut was mentioned in § 3.2.2. As discussed there, artificially large values of $\not{h}$ can also result in events with multiple jets below the selection requirement of $e > 50\,\mathrm{GeV}$. To protect against these events, $\not{h}$ is compared with $\not{p}$ from all of the calorimeter towers irrespective of secondary clustering and thresholding [125]. Events with $\not{h}/\not{p} > 1.25$ are rejected. The use of the full-calorimeter $\not{p}$ does not fundamentally change the flavour of the analysis; such events may be thought of as suffering from a measurement error due to thresholding. The $\not{p}$ variable is used to confirm this (as noted in § 3.2).

Table 5.1 shows the cutflow for the entire analysis chain, while the individual breakdowns for the QCD backgrounds, W-based electroweak backgrounds, Z-based electroweak backgrounds, and signal event samples can be found in Tables C.1, C.2, C.3 and C.4 in Appendix C respectively[2]. The expectations from simulation are listed only for comparison; the actual expected yields from irreducible SM backgrounds are determined from independent control samples. 13 events in the signal Σh region were found to pass the signal selection criteria in the 2010 data set, corresponding to an integrated luminosity of $35.1\,\mathrm{pb}^{-1}$.

After the α_T, ΔR_{ECAL} and $\not{h}/\not{p}$ cuts, the QCD background predicted by `Pythia 6` is less than one event. This estimate was confirmed with a different parameter set for `Pythia 8` (tune 1) and with the `MadGraph` generator. The only significant remaining background after all cuts stems from electroweak processes with real missing energy in the final state. In the di-jet case, the largest backgrounds with real missing energy are the associated production of W and Z bosons with jets, followed by the weak decays, $Z \rightarrow \nu\bar{\nu}$ and $W \rightarrow \tau\nu$. At higher jet multiplicities, $t\bar{t}$ production with

---

[2] Table 5.1 also includes contributions from the $\gamma + nj$ Monte Carlo samples that are not presented in Appendix C.

semileptonic weak decays of the t and $\bar{t}$ quarks, becomes important. In this case, the three backgrounds, $Z \to \nu\bar{\nu}$ + jets, W + jets and $t\bar{t}$, which will be referred to collectively as the electroweak (EWK) backgrounds in what follows, are of roughly equal size. The largest fraction of the W + jet and $t\bar{t}$ backgrounds stem from $W \to \tau\nu$ decays where in two thirds of the cases the τ decays hadronically and is either identified as a jet, or the electrons and muons from the τ decay are not identified because they fail the acceptance cuts ($p > 10\,\mathrm{GeV}$ and η coverage). The techniques used to predict the yields of these background from independent control samples are briefly described in the following section.

Cut	SM (with Pythia 6 QCD)			SM (with Pythia 8 QCD)			Data		
	a)	b)	c)	a)	b)	c)	a)	b)	c)
Selection	14.99 M	-	-	15.00 M	-	-	9.91 M	-	-
$\Sigma h > 250\,\mathrm{GeV}$	5.82 M	0.0	61.2	5.68 M	0.0	62.1	4.68 M	0.0	52.8
$N^\gamma = 0$	5.81 M	0.2	0.2	5.67 M	0.2	0.2	4.67 M	0.2	0.2
$N^e = 0$	5.80 M	0.3	0.1	5.66 M	0.3	0.1	4.66 M	0.3	0.1
$N^\mu = 0$	5.69 M	2.1	0.0	5.57 M	2.1	0.0	4.52 M	3.3	0.0
Bad μ in j	5.67 M	2.4	0.3	5.55 M	2.4	0.3	4.50 M	3.7	0.4
Odd j veto	5.57 M	4.3	1.9	5.42 M	4.6	2.3	4.44 M	4.9	1.3
$j^1 : |\eta| < 2.5$	5.34 M	8.1	4.1	5.19 M	8.7	4.3	4.30 M	8.0	3.2
$j^2 : e > 100\,\mathrm{GeV}$	3.40 M	41.5	36.3	3.07 M	45.9	40.8	2.89 M	38.2	32.8
$\Sigma h > 350\,\mathrm{GeV}$	1.11 M	80.9	67.4	1.12 M	80.3	63.5	$(908 \pm 1)\,\mathrm{k}$	80.6	68.6
$\alpha_T > 0.55$	30.5 ± 4.7	≥ 99.9	≥ 99.9	35.3 ± 9.3	≥ 99.9	≥ 99.9	37.0 ± 6.1	≥ 99.9	≥ 99.9
$\Delta R_{\mathrm{ECAL}} > 0.3 \wedge \Delta\phi^* > 0.5$	24.5 ± 4.2	≥ 99.9	19.5	26.5 ± 7.9	≥ 99.9	25.1	32.0 ± 5.7	≥ 99.9	13.2
$\not{H}/\not{p} < 1.25$	9.26 ± 0.88	≥ 99.9	62.2	9.24 ± 0.88	≥ 99.9	65.1	13.0 ± 3.6	≥ 99.9	57.6

Table 5.1: Cut flow for $35.1\,\mathrm{pb}^{-1}$, $N^j \geq 2$. Column a) is the number of events passing the cut, column b) is the percentage of events lost of those passing the intial $\Sigma h > 250\,\mathrm{GeV}$ cut (cumulative), and column c) is the percentage lost from the previous cut.

5.2 Data-driven background estimates

The SM background in the signal region is estimated directly from data using two independent methods. The first method makes use of control regions at lower Σh to estimate the total background from all SM processes (Section 5.2.1), while the second method estimates the contribution from electroweak processes using $W \to \mu\nu$ + jets and γ + jets events in the data (Section 5.2.2). It should be noted that the author was not extensively involved in these studies, so the methods employed are briefly summarised and the results are quoted from [18] for the reader's convenience. Full details may be found in [120]. Nevertheless, both methods rely on the fact that α_T may be used to robustly reject backgrounds due to mismeasurement, leaving only candidate signal events that are caused by the real missing momentum due to the production and subsequent escape of an invisible Standard Model particle.

5.2.1 Inclusive background estimate

The "inclusive" method postulates that the total background – i.e. any contribution to n_+ from non-supersymmetric events – can be estimated from two control regions defined in bins of Σh which, in order to keep the available phase space constant, are defined in the all-hadronic channel as follows:

- `HT250`: $250 < \Sigma h < 300\,\mathrm{GeV}$, $e^j_{1,2} > 71\,\mathrm{GeV}$, $e^j_{\mathrm{min.}} > 36\,\mathrm{GeV}$;

- `HT300`: $300 < \Sigma h < 350\,\mathrm{GeV}$, $e^j_{1,2} > 86\,\mathrm{GeV}$, $e^j_{\mathrm{min.}} > 43\,\mathrm{GeV}$.

The method uses the ratio of events passing and failing a requirement on α_T, R_{α_T} (given all other selection criteria, including the auxiliary cuts), to extrapolate the number of events in the signal region `HT350` from the other two regions.

It has been shown [126] that for events with $\alpha_T > 0.51$, where mismeasurement is still an issue, that this ratio R_{α_T} decreases as a function of Σh. This is thought to be due to the fact that mismeasurement becomes less of an issue as the scale of the event gets larger. For a cut of $\alpha_T > 0.55$, however, R_{α_T} as a function of Σh is shown to be flat, as events with a value of α_T larger than 0.55 must contain real $\not{p}$, which is unaffected by detector mismeasurements. This is confirmed by performing the same analysis with the (real $\not{p}$) muon control sample (as defined in § 5.2.2). Given this assumption, the number of events in the signal region is predicted by:

$$N_{\alpha_T>0.55}^{350,\,\text{pred.}} = N_{\alpha_T<0.55}^{350,\,\text{pred.}} \times \frac{R_{\alpha_T}^{300,\,\text{meas.}}}{R_{\alpha_T}^{250,\,\text{meas.}}} \times R_{\alpha_T}^{300,\,\text{meas.}}. \tag{5.2}$$

Using this method, the total number of background events in the `HT350` (signal) region was determined to be $9.4\,^{+4.8}_{-4.0}\,(\text{stat.}) \pm 1.0\,(\text{syst.})$. The dominant systematic error was due to the three electroweak processes, and was estimated by varying the relative contribution of each separately. Two similar inclusive methods that made use of Monte Carlo simulations were also used to make similar but less conservative estimates; consequently, the purely data-driven result is used in what follows.

5.2.2 Electroweak background estimates

A second background estimation method uses an independent selection of $W \to \mu\nu$ + jets and γ + jets events in the data in order to estimate the contribution from SM processes with real missing energy.

The $W \to \mu\nu$ + jet events are selected as described in [127]. A high-p, well-isolated muon is required to be in the final state, and by requiring the transverse mass of the W to be larger than $30\,\text{GeV}$ a pure sample of W + jets events is obtained. Muons are required to be separated from the jets in a given event by a distance larger than 0.5 in the $(\eta,\,\phi)$ plane. Since $\alpha_T > 0.55$ implies $\not{k}/\Sigma h > 0.4$, only events with $\not{k} > 140\,\text{GeV}$ are considered in the signal region `HT350`.

To maximise the chance that a given event will pass the α_T cut, the event is required to have $\displaystyle{\not}h > 140\,\mathrm{GeV}$. Since $\displaystyle{\not}h$ appears in α_T relative to Σh, in the lower Σh regions this requirement is scaled accordingly to $\displaystyle{\not}h > 120$ ($\displaystyle{\not}h > 100$) for `HT300` (`HT250`). In the signal region this selection yields 25 events in agreement with 29.4 ± 1.4 events predicted by the simulation. In the `HT250` (`HT300`) region, 134 (52) W candidates are reconstructed in agreement with the prediction of 135.5 ± 3.2 (56.7 ± 2.2) events. The fraction of EWK events with $\alpha_T > 0.55$ in the data is also in good agreement with the simulation: 7 data events are found in the signal region, compared to 5.9 ± 0.6 events from simulation, whereas 32 (12) events in the data pass the $\alpha_T > 0.55$ requirement in the `HT250` (`HT300`) region, compared to 29.2 ± 1.4 (11.1 ± 1.1) expected events.

The number of W + jet events satisfying the hadronic final state selection of Section 5.1, $n_{\mathrm{data}}^{\mathrm{W;\ had}}$, can be estimated from the number of events in the muon sample, $n_{\mathrm{data}}^{\mathrm{W;\ \mu}}$, and the expected relative ratio of these two types of events. In the results presented in [18], the value of this ratio was taken from the Monte Carlo simulation, yielding

$$n_{\mathrm{data}}^{\mathrm{W;\ had}} = n_{\mathrm{data}}^{\mathrm{W;\ \mu}} \times n_{\mathrm{MC}}^{\mathrm{W;\ had}} / n_{\mathrm{MC}}^{\mathrm{W;\ \mu}} \approx 0.86 \times n_{\mathrm{data}}^{\mathrm{W;\ \mu}}. \tag{5.3}$$

The total background from W + jets and $t\bar{t}$ processes is thus estimated to be $6.1_{-1.9}^{+2.8}$ (stat) $\pm$ 1.8 (syst). Given the reliance on Monte Carlo simulation for the factor $N_{\mathrm{MC}}^{\mathrm{W;\ had}} / N_{\mathrm{MC}}^{\mathrm{W;\mu}}$, conservative uncertainties on all the parameters entering this ratio have been assigned. The systematic uncertainty is estimated to be 30% and is dominated by the uncertainty on the efficiency for vetoing leptons.

The remaining irreducible background stems from $Z \rightarrow \nu\bar{\nu}$ + jet events. An estimate of this background can be obtained from the γ + jets process, which has a larger cross section but kinematic properties similar to those of $Z \rightarrow \nu\bar{\nu}$ events when the photon is ignored [128]. These γ + jets events provide a measurement of the acceptance of the α_T cut directly from data. The γ + jets sample is selected by requiring photons, i.e. localized electromagnetic depositions satisfying very tight isolation criteria, with

p greater than $100\,\mathrm{GeV}$, $|\eta|$ less than 1.45 and $\Delta R(\gamma, \mathrm{jet}) > 1$. Ignoring the photon, the same hadronic final state selection as described in Section 5.1 is applied. As with the W sample, $\not{E}$ is required to exceed $140\,\mathrm{GeV}$. This selection yields 7 events in data compared with 6.5 ± 0.4 expected from simulation.

The relative acceptances, together with the appropriate ratio of cross sections for $\gamma +$ jets and $Z \to \nu\bar{\nu} +$ jets, which is taken from simulation, are then used to estimate the number of $Z \to \nu\bar{\nu}$ events in the signal region, found to be $4.4^{+2.3}_{-1.6}\,(\mathrm{stat}) \pm 1.8\,(\mathrm{syst})$. The main systematic uncertainties arise from the ratio of cross sections for $\gamma +$ jets to $Z \to \nu\bar{\nu} +$ jets in the simulation (30%), the efficiency for photon identification (20%), and the purity of the photon selection (20%), which add to $\approx 40\%$. This uncertainty is confirmed using $\gamma +$ jets events to predict the number of events in the $W \to \mu\nu$ sample, requiring, in both cases, $250 < \Sigma h < 350\mathrm{GeV}$, $N^j = 2$, and $\alpha_T > 0.55$. The prediction of $8.5 \pm 1.5\,(\mathrm{stat}) \pm 2.6\,(\mathrm{syst})$ agrees well with the 10 events observed. This agreement gives confidence in the notion that the size of the assigned systematic uncertainties is adequate.

Combining the W and γ results, the estimate of the SM background arising from EWK processes with real missing energy is $10.5^{+3.6}_{-2.5}$ events, which is in good agreement with the inclusive estimate obtained from the lower Σh control regions. All of the background estimates are used in the exclusion limit calculations, which are the subject of the following section.

5.3   Interpretation of the result

The number of signal events yielded from the $35.1\,\mathrm{pb}^{-1}$ of proton-proton collision data collected in 2010 has been found to be consistent with the data-driven estimates of the number of signal events one would expect from the irreducible, real $\not{p}$ Standard Model backgrounds. At first glance, one may infer that the null hypothesis holds and that Nature is not described by this particular supersymmetric model. A more technical examination of the statistics supporting this conclusion is presented in § 5.3.1.

One can and should go further than this, and use the results reported in [18] to constrain the values of some of the CMSSM parameters. The subsequent exclusion limits on the supersymmetric parameter space are presented in § 5.3.2. A summary of the relevant parts of the limit calculations performed in [120] are quoted for completeness and the convenience of the reader.

5.3.1   Methodology and limit on the signal yield

This analysis is a counting experiment. The search strategy employed counts the number of interesting events (as defined by the preselection criteria) that pass a cut on a property of an event that marks it out as a potential signal of physics beyond the Standard Model. This information is then used to draw conclusions about whether supersymmetry may describe physics beyond the Standard Model.

In what follows, the number of events observed to meet the signal criteria is denoted by n_+^{350}. The "350" denotes that the events are from the signal Σh region, while the "+" denotes that they have passed the signal criteria. This datum, obtained from the experiment, can then be compared to the number of events that an observer with some prior knowledge χ might expect to see.

In the toy analysis, it was assumed that the only events the observer might have expected to see would be from events with a non-SM origin – the signal. The expected number of events in the signal region passing the cut is then denoted by s_+^{350}, and comparing s_+^{350} to n_+^{350} allows the observer to draw conclusions about their original hypotheses. A model described by a point in the CMSSM parameter space might predict $s_+^{350} > 0$, while the null hypothesis $\mathcal{H}(0)$ predicts $s_+^{350} = 0$. As noted earlier, $n_+^{350} > 0$ suggests, in the absence of an expected background, that $\mathcal{H}(0)$ may be rejected.

However, $n_+^{350} = 0$ does not necessarily rule out supersymmetry. Rather, this observation allows the observer to exclude that particular model of Nature to some Confidence Level (CL); after all, the observer may have just been unlucky and not seen any signal events in that particular experiment. In this scenario, the observer may then ask, "*what is the largest value that s_+^{350} could take that is consistent with the datum $n_+^{350} = 0$?*" In principle, of course, s_+^{350} could be infinite and the observer could have been infinitely unlucky. The notion of Confidence Levels is therefore used to describe a range of values for s_+^{350} that should cover some percentage of eventualities.

The upper limit of this interval is of some interest to the sparticle hunter. If a particular supersymmetric model predicts a value of s_+^{350} that is outside of the interval, the model is said to be rejected at this confidence limit. This concept is key to the notion of constraining the supersymmetric parameter space, as shall be seen later.

Continuing with the example of the toy analysis, the probability of n_+^{350} events given an expected value of s_+^{350} is described by a Poisson distribution

$$\Pr(n_+^{350}|\,s_+^{350}) = \frac{\left(s_+^{350}\right)^{n_+^{350}} \exp\left[-s_+^{350}\right]}{n_+^{350}!} \tag{5.4}$$

The confidence interval on s_+^{350} may then be calculated using the Feldman-Cousins method [129] by:

- calculating the confidence interval over n_+^{350} for a given value of s_+^{350} by summing over the probabilities $\Pr(n_+^{350}|\, s_+^{350})$ until the desired coverage is reached. Which n_+^{350} values to include in the interval is decided by a ranking of each n_+^{350} value based on the ratio

$$\frac{\Pr(n_+^{350}|\, s_+^{350})}{\Pr(n_+^{350}|\, s_+^{350}{}_{\text{best}})},\tag{5.5}$$

  where $s_+^{350}{}_{\text{best}}$ is the most probable value of s_+^{350} given n_+^{350}. This ensures meaningful limits are obtained even for small values of n_+^{350} and s_+^{350};

- the desired interval over s_+^{350} is then determined by taking the values of s_+^{350} permitted for a given n_+^{350} value as calculated above. One may think of the n_+^{350} intervals plotted horizontally in the $n_+^{350} - s_+^{350}$ plane. The s_+^{350} intervals are then taken from the vertical bands on the same plot.

So, for example, if $n_+^{350} = 0$ in the toy analysis, one may read from the table in [129] that, for $n = 0$ and $b = 0$, the 95% CL interval for s_+^{350} is $[0, 3.09]$ and the upper limit is 3.09. Thus any supersymmetric model that had predicted more than 3.09 events in the signal region would be excluded at the 95% CL.

In reality, there are irreducible backgrounds from real $\not{p}$ processes that may contribute to the n_+^{350} events observed. Thus the expected number of events in the signal Σh region that meet the signal criteria is

$$s_+^{350} + b_+^{350,\,\text{incl.}} = s_+^{350} + b_+^{350,\,W/tt} + b_+^{350,\,Z\text{inv.}} + b_+^{350,\,\text{QCD}},\tag{5.6}$$

where the inclusive number of background events in the signal Σh region, $b_+^{350,\,\text{incl.}}$, has been split into its component contributions from $W/t\bar{t}$, $Z \to \nu\bar{\nu}$ and QCD processes. The Feldman-Cousins method may again be used to obtain the 95% CL interval for s_+^{350}, given n_+^{350} and the data-driven estimates of the expected backgrounds calculated from the results quoted in § 5.2.

In order that these background estimates are constrained using data from the control regions, the input to the Feldman-Cousins calculation is actually the product of the probability distributions

$$\Pi_{\text{tot.}} = \Pi_{\text{signal}} \times \Pi_{\text{incl.}} \times \Pi_{W/t\bar{t}} \times \Pi_{Z \to \nu\bar{\nu}}, \tag{5.7}$$

where $\Pi_{\text{signal}} = \text{Pois.}(n_+^{350}, s_+^{350} + b_+^{350,\,\text{incl.}})$ provides the handle on s_+^{350} that ultimately determines the limits on the expected number of signal (non-SM) events, and $\Pi_{\text{incl.}}$, $\Pi_{W/t\bar{t}}$ and $\Pi_{Z \to \nu\bar{\nu}}$ constrain the respective background estimates by modelling each control region as its own independent counting experiment. Results from Monte Carlo simulation are used to relate the expected number of background events in the signal Σh region from the control regions; the uncertainties are then treated as nuisance parameters, modelled using a Gaussian distribution [130]. A Poisson distribution is used to model the corresponding counting experiment. For example,

$$\Pi_{W/t\bar{t}} = \text{Pois.}(n_+^{\mu}, \tau^{\mu} \cdot b_+^{350,\,W/tt}) \times \text{Gaus.}(\tau^{\mu}, \sigma^{\mu}), \tag{5.8}$$

where n_+^{μ} is the number of events observed in the muon control region used to estimate the $W/t\bar{t}$ contribution to the expected background, τ^{μ} is a factor taken from Monte Carlo relating n_+^{μ} to $b_+^{350,\,W/tt}$, and σ^{μ} is the uncertainty on τ^{μ}. The same treatment is given to the systematic uncertainties on the efficiency of the supersymmetric signal, which is model-dependent. Further details may be found in [120].

If signal contamination in the background control samples is ignored, an upper limit on the number of signal events, s_+^{350}, compatible with the observed number of events in each signal and control region can be calculated using the method outlined above. For an integrated luminosity of $35.1\,\text{pb}^{-1}$, this number is 13.4 events at the 95 % CL. This may then be compared with the expected number of events expected from the signal processes when interpreting the result, as is done in the following subsection.

5.3.2   Interpretation within the CMSSM

To interpret the consistency of the observed number of events with the background expectation in the context of a model, and also to allow comparisons with other experimental results, the number of expected signal events s_+^{350} is used to set an exclusion limit on models based on various points in the CMSSM parameter space. This limit is obtained by testing whether the number of signal events predicted after all of the selection cuts is compatible with observations at the 95% CL for each of these points. If a given point predicts more than 13.4 events, it is excluded. Signal contamination in the control samples used to determine the data-driven background is taken into account [120]. As the search is designed for robustness and background control, the same selection is applied at each point in the parameter space. The 95%CL limit in the $M_0 - M_{1/2}$ plane for $\tan\beta = 3$ $A_0 = 0$ and sign $|\mu|$ is shown in Figure 5.8. LM0 is excluded at the 99.99% CL, LM1 at the 99.2% CL.

The number of events predicted by each point in the CMSSM parameter space is calculated using a similar methodology to that used in the toy analysis in § 3.2. The SUSY particle spectrum is calculated using `SOFTSUSY` [63], and the signal events are generated at LO with `Pythia 6`. Next to Leading Order (NLO) cross sections, again obtained with the `PROSPINO` cross-section calculation software [80], are used to calculate the measured and expected exclusion contours the latter obtained from using the number of background events from the muon and photon control samples only (as opposed to the actual number of events measured in the signal region, which is 13). Systematic uncertainties on the NLO predictions due to the choice of the renormalization and factorization scale have been taken into account. Additionally, the uncertainties on the PDFs for `CTEQ6.6` have been estimated using the envelope provided by the central values and the PDF $+ \alpha_S$ errors. For reference, the observed limit using LO cross sections is also shown.
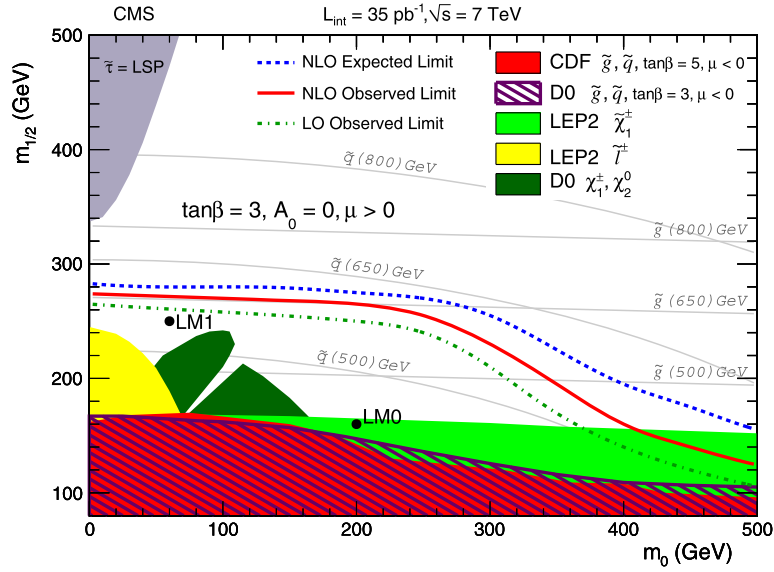
Figure 5.8: Measured (red line) and expected (dashed blue line) 95% CL exclusion contour at NLO in the CMSSM $(M_0, M_{1/2})$ plane ($\tan\beta = 3$, $A_0 = 0$GeV, sign$|\mu| > 0$). The measured LO exclusion contour is also shown as well (dashed green line). The area below the curves is excluded by the measurements presented here. Exclusion limits obtained from previous experiments are presented as filled areas in the plot. Black lines indicate constant squark and gluino masses. For reference, the plot shows the two benchmark points LM0 and LM1 (though it should be noted that for these particular benchmark points, $\tan\beta = 10$).

The expected limit covers a larger part of the $M_0 - M_{1/2}$ plane than the actual measured limit, as the observed number of events in the signal region is slightly larger than the number of background events predicted from the control regions. The excluded regions for the Tevatron's CDF search for jets + missing energy final states [131] have been obtained for $\tan\beta = 5$, while those from D0 [132] have been obtained for $\tan\beta = 3$, each using approximately $2\,\mathrm{fb}^{-1}$ of $p\bar{p}$ collision data. The Large Electron-Positron (LEP) collider excluded regions are based on searches for sleptons and charginos [133]. A comparison of the exclusion limit for $\tan\beta = 3$ to that for $\tan\beta = 10$ for fixed values of $A_0 = 0$ and sign$|\mu| > 0$ indicates that the exclusion reach is only weakly dependent on the value of $\tan\beta$; the limit shifts by $< 20\,\mathrm{GeV}$ in M_0 and $< 10\,\mathrm{GeV}$ in $M_{1/2}$. The D0 exclusion limit obtained from neutralino searches [134] is also included in Fig. 5.8. In contrast to the other limits presented in Figure 5.8, the result of the trilepton search is strongly dependent on the choice of $\tan\beta$ and reaches its highest sensitivity in the CMSSM for $\tan\beta < 10$.

Chapter 6

Summary and conclusions

"The game of science is, in principle, without end."

Karl Popper, *The Logic of Scientific Discovery (1934)*

6.1   Summary

- A methodology for the construction of models – QFT Lagrangians that describe Nature at a given energy scale – has been described in the context of building the Standard Model of particle physics. The motivations for extending this model with the introduction of an additional fundamental symmetry – *supersymmetry* – were put forward, and the construction of the CMSSM, a form of Minimal Supergravity, was presented as such an extension.

- A strategy aimed at reducing the probability of erroneous outcomes due to flaws in the measurement system – and uncertainty in the observer's knowledge of those flaws – by exploiting information in the event kinematics was presented. Taking inspiration from previously defined variables in the dijet topology, the underlying philosophy – the separation of energy and angular

information from the detector output – is expounded and used to extend the approach to the multijet topology, making the search possible with early LHC data. The *a priori* robustness of the approach is demonstrated using the simplified measurement system with varying degrees of mismeasurement.

- The first search for supersymmetry in events collected by the CMS experiment (or indeed any LHC experiment) from proton-proton collisions at $\sqrt{s} = 7\,\mathrm{TeV}$ has been presented in [18] and are reported here for completeness. The all-hadronic channel, with a final state topology of two or more particle jets and large missing transverse momentum, has been analysed in data corresponding to $35.1\,\mathrm{pb}^{-1}$. The robust strategy mentioned above is applied to effectively remove the otherwise overwhelming contribution to the signal region from mismeasured QCD background. The contribution from the irreducible real missing transverse momentum SM processes is estimated from a selection of independent control samples. From these measurements, an estimate on the upper limit of non-SM events in the analysis signal region is made at the 95% Confidence Limit.

6.2   Conclusions

The measurements made using the strategy described here, tailored to be robust to mismeasurement and uncertainty in the degree of mismeasurement in the detector, are consistent with the null hypothesis – that Nature at the electroweak scale is described by the Standard Model. No excess in the number of events passing the α_T cut is observed. This outcome is therefore used to constrain the supersymmetric parameter space by excluding the points that predict more events in the signal region than are compatible with what was observed in the data. The region of CMSSM parameter space excluded is much larger than that of previous experiments.

The search for supersymmetry continues.

Appendix A

Particle kinematics

Invariant mass, transverse energy and transverse mass

The invariant mass of a single particle in Minkowski spacetime is defined as

$$M \equiv \sqrt{E^2 - |\mathbf{P}|^2} \equiv \sqrt{E^2 - \mathbf{p} \cdot \mathbf{p} - q^2} \tag{A.1}$$

Following [65], one may define the *transverse energy* $e \, (= E_T)$ of a single particle as its energy in the rest frame where its longitudinal momentum is zero, i.e. $q (\equiv p_z) = 0$. Thus

$$e^2 \equiv p_x^2 + p_y^2 + M^2 = |\mathbf{p}|^2 + M^2 = E^2 - q^2. \tag{A.2}$$

Defining the *transverse mass* $m \, (\equiv M_T)$ in the same manner as Equation A.1,

$$m = \sqrt{e^2 - |\mathbf{p}|^2} = \sqrt{E^2 - q^2 - |\mathbf{p}|^2} = M, \tag{A.3}$$

i.e. the transverse mass is the same as the invariant mass for a single particle (which is, of course, to be expected by definition).

Rapidity and pseudo-rapidity

Following [65], the *rapidity y* of a single (massive) particle along the z axis is defined as

$$y \equiv \frac{1}{2} \ln \frac{E+q}{E-q} = \frac{1}{2} \ln \frac{1+\beta \cos \theta}{1-\beta \cos \theta}, \tag{A.4}$$

where $\beta = P/E$ and θ is the polar angle relative to the z axis. The *pseudo-rapidity* η is the rapidity in the limit $\beta \to 1$, i.e. for a massless particle.

$$\eta \equiv \frac{1}{2} \ln \frac{1+\cos \theta}{1-\cos \theta} = -\ln \tan \frac{\theta}{2} \tag{A.5}$$

Massless particles in (η, ϕ) space

Consider a massless particle with energy $(E \pm \sigma_E)$ emerging from the origin with direction $((\eta \pm \sigma_\eta), (\phi \pm \sigma_\phi))$. Following [65], the 3-momentum components are

$$p_x(E, \eta, \phi) = E \operatorname{sech} \eta \cos \phi, \tag{A.6}$$

$$p_x(E, \eta, \phi) = E \operatorname{sech} \eta \sin \phi, \tag{A.7}$$

$$p_z(E, \eta, \phi) = E \tanh \eta, \tag{A.8}$$

and the associated uncertainties are

$$\sigma_{p_x}^2 = \left(\frac{\partial p_x}{\partial E}\right)^2 (\sigma_E)^2 + \left(\frac{\partial p_x}{\partial \eta}\right)^2 (\sigma_\eta)^2 + \left(\frac{\partial p_x}{\partial \phi}\right)^2 (\sigma_\phi)^2 \tag{A.9}$$

$$= (\operatorname{sech} \eta \cos \phi)^2 (\sigma_E)^2 + (E \operatorname{sech} \eta \tanh \eta \cos \phi)^2 (\sigma_\eta)^2 +$$

$$(E \operatorname{sech} \eta \sin \phi)^2 (\sigma_\phi)^2 \tag{A.10}$$

$$\sigma_{p_y}^2 = \left(\frac{\partial p_y}{\partial E}\right)^2 (\sigma_E)^2 + \left(\frac{\partial p_y}{\partial \eta}\right)^2 (\sigma_\eta)^2 + \left(\frac{\partial p_y}{\partial \phi}\right)^2 (\sigma_\phi)^2 \tag{A.11}$$

$$= (\operatorname{sech} \eta \sin \phi)^2 (\sigma_E)^2 + (E \operatorname{sech} \eta \tanh \eta \sin \phi)^2 (\sigma_\eta)^2 +$$

$$(E \operatorname{sech} \eta \cos \phi)^2 (\sigma_\phi)^2 \tag{A.12}$$

$$\sigma_{p_z}^2 = \left(\frac{\partial p_z}{\partial E}\right)^2 (\sigma_E)^2 + \left(\frac{\partial p_z}{\partial \eta}\right)^2 (\sigma_\eta)^2 + \left(\frac{\partial p_z}{\partial \phi}\right)^2 (\sigma_\phi)^2 \tag{A.13}$$

$$= (\tanh \eta)^2 (\sigma_E)^2 + \left(E \operatorname{sech} \eta^2\right)^2 (\sigma_\eta)^2. \tag{A.14}$$

Alternatively, if the position associated with an energy deposit is more conveniently expressed in Cartesian coordinates, i.e. x, y, z, σ_x, σ_y, σ_z (defined relative to the origin), then one may use

$$p_x = E\,\frac{x}{R} \tag{A.15}$$

$$p_y = E\,\frac{y}{R} \tag{A.16}$$

$$p_z = E\,\frac{z}{R}, \tag{A.17}$$

where $R = \sqrt{x^2 + y^2 + z^2}$ is the distance of the energy deposit from the origin. The corresponding uncertainties are

$$\sigma_{p_x}^2 = \left(\frac{\partial p_x}{\partial x}\right)^2 (\sigma_x)^2 + \left(\frac{\partial p_x}{\partial y}\right)^2 (\sigma_y)^2 + \left(\frac{\partial p_x}{\partial z}\right)^2 (\sigma_z)^2 \tag{A.18}$$

$$= E^2\left[\left(\frac{y^2+z^2}{R^3}\right)^2 (\sigma_x)^2 + \left(\frac{xy}{R^3}\right)^2 (\sigma_y)^2 + \left(\frac{xz}{R^3}\right)^2 (\sigma_z)^2\right] \tag{A.19}$$

$$\sigma_{p_y}^2 = \left(\frac{\partial p_y}{\partial x}\right)^2 (\sigma_x)^2 + \left(\frac{\partial p_y}{\partial y}\right)^2 (\sigma_y)^2 + \left(\frac{\partial p_y}{\partial z}\right)^2 (\sigma_z)^2 \tag{A.20}$$

$$= E^2\left[\left(\frac{xy}{R^3}\right)^2 (\sigma_x)^2 + \left(\frac{x^2+z^2}{R^3}\right)^2 (\sigma_y)^2 + \left(\frac{yz}{R^3}\right)^2 (\sigma_z)^2\right] \tag{A.21}$$

$$\sigma_{p_z}^2 = \left(\frac{\partial p_z}{\partial x}\right)^2 (\sigma_x)^2 + \left(\frac{\partial p_z}{\partial y}\right)^2 (\sigma_y)^2 + \left(\frac{\partial p_z}{\partial z}\right)^2 (\sigma_z)^2 \tag{A.22}$$

$$= E^2\left[\left(\frac{xz}{R^3}\right)^2 (\sigma_x)^2 + \left(\frac{yz}{R^3}\right)^2 (\sigma_z)^2 + \left(\frac{x^2+y^2}{R^3}\right)^2 (\sigma_y)^2\right]. \tag{A.23}$$

Appendix B

The Silicon Strip Tracker Spy Channel

During high-luminosity running, the tracker Front End Drivers (FEDs) will be running in zero-suppressed mode. This means that only data from clustered tracker hits will be forwarded to the Data AcQuisition (DAQ) for further processing. While this is necessary to reduce the volume of data that needs to be transmitted, it means that when the tracker is running it will not be possible to monitor the raw, unprocessed output of the detector via the global DAQ system.

The SST tracker readout system Delay FPGAs have therefore been designed to make virgin raw data from the tracker available during runtime via a *spy channel*. These data can then be analysed locally to provide online monitoring and analysis capabilities. A tracker SpyDAQ system was used to implement the spy channel, and address the following issues:

- The data received from the tracker electronics are not wrapped in the headers and trailer required by the readout chain;

- A local online monitoring system can not use the same FED Supervisor applications as the global readout chain, as this would require the local monitoring software configuration to be integrated into the global software configuration.

The architecture of the SpyDAQ system is shown in Figure B.1. On receipt of spy trigger signal, generated by the global trigger system, the FED Supervisor will extract the virgin raw data from the tracker electronics via the FED. This is then sent to an area of shared memory in the FED readout crate, managed by the FED Spy Supervisor application. New data found in the shared memory are wrapped in the necessary DAQ header and trailer and tracker header and passed on to the crate Data Sender. Data acquisition then proceeds as in the local DAQ system. The author contributed to the design and implementation of the tracker SpyDAQ system.
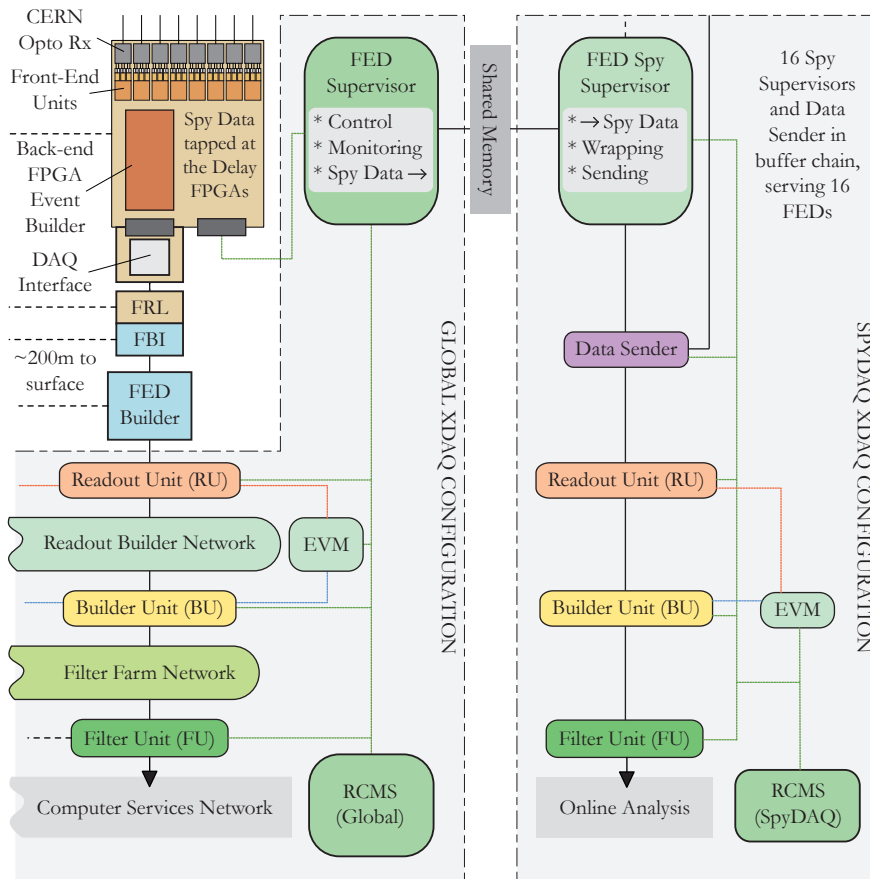
Figure B.1: The architecture for the SpyDAQ data acquisition system, used for online monitoring of the silicon strip tracker virgin raw data. The left-hand side shows the standard tracker DAQ readout column. An adapted local DAQ configuration is used for online monitoring. The key component is the FED Spy Supervisor, a XDAQ application that wraps raw data obtained at the FED Delay FPGAs with the necessary DAQ/Tracker headers and trailer, and manages the shared memory used to transfer data between the two XDAQ configurations.

Appendix C

Monte Carlo Sample Cut Flow Tables

Tables C.1, C.2, and C.3 contain the cut flows for the individual Monte Carlo samples that make up the Standard Model background entries in Table 5.1. Table C.4 lists the corresponding cut flow for the LM0 and LM1 signal points. The tables are reproduced from [120].

Cut	QCD Pythia 6 (38X)			QCD Pythia 8 (38X)			QCD MadGraph (36X)		
	a)	b)	c)	a)	b)	c)	a)	b)	c)
Selection	14.98 M	-	-	14.98 M	-	-	8.83 M	-	-
$\Sigma h > 250\,\text{GeV}$	5.81 M	0.0	61.2	5.68 M	0.0	62.1	3.34 M	0.0	62.1
$N^\gamma = 0$	5.80 M	0.2	0.2	5.66 M	0.2	0.2	3.34 M	0.1	0.1
$N^e = 0$	5.79 M	0.2	0.1	5.66 M	0.3	0.1	3.34 M	0.1	0.1
$N^\mu = 0$	5.69 M	2.1	1.9	5.56 M	2.0	1.7	3.34 M	2.5	2.3
Bad μ in j	5.67 M	2.4	0.3	5.54 M	2.3	0.3	3.25 M	2.9	0.5
Odd j veto	5.56 M	4.2	1.9	5.42 M	4.5	2.3	3.21 M	3.9	1.1
$j^1 : |\eta| < 2.5$	5.34 M	8.1	4.1	5.19 M	8.6	4.3	3.07 M	8.1	4.4
$j^2 : e > 100\,\text{GeV}$	3.40 M	41.5	36.3	3.07 M	45.9	40.8	2.14 M	36.0	30.3
$\Sigma h > 350\,\text{GeV}$	1.11 M	80.9	67.4	1.12 M	80.3	63.6	$(610 \pm 1)\,\text{k}$	81.8	71.5
$\alpha_T > 0.55$	19.5 ± 4.6	≥ 99.9	≥ 99.9	24.4 ± 9.2	≥ 99.9	≥ 99.9	30.1 ± 28.4	≥ 99.9	≥ 99.9
$\Delta R_\text{ECAL} > 0.3 \wedge \Delta\phi^* > 0.5$	14.3 ± 4.1	≥ 99.9	26.7	16.2 ± 7.9	≥ 99.9	33.4	1.01 ± 0.28	≥ 99.9	96.6
$k\!\!\!/p < 1.25$	0.03 ± 0.02	≥ 99.9	99.8	0.01 ± 0.00	≥ 99.9	≥ 99.9	0.23 ± 0.14	≥ 99.9	76.9

Table C.1: Cut flow for the QCD Monte Carlo samples scaled to $\int L\,dt = 35.1\,\text{pb}^{-1}$ for $N^j \geq 2$. Column a) is the number of events passing the cut, column b) is the percentage of events lost of those passing the intial $\Sigma h > 250\,\text{GeV}$ cut (cumulative), and column c) is the percentage lost from the previous cut. The QCD Pythia samples are reconstructed with CMSSW_3_8_X, while the MadGraph sample used CMSSW_3_6_X.

Cut	$W + nj$			$t\bar{t}$		
	a)	b)	c)	a)	b)	c)
Selection	$(4.3 \pm 0.0)\,$k	-	-	$(3.7 \pm 0.0)\,$k	-	-
$\Sigma h > 250\,$GeV	$(2.0 \pm 0.0)\,$k	0.0	54.8	$(2.5 \pm 0.0)\,$k	0.0	32.8
$N^\gamma = 0$	$(1.7 \pm 0.0)\,$k	14.9	14.9	$(2.3 \pm 0.0)\,$k	8.0	8.0
$N^e = 0$	$(1.5 \pm 0.0)\,$k	20.8	6.9	$(2.2 \pm 0.0)\,$k	11.8	4.1
$N^\mu = 0$	$(1.1 \pm 0.0)\,$k	44.9	27.7	$(1.8 \pm 0.0)\,$k	26.7	1.6
Bad μ in j	$(1.1 \pm 0.0)\,$k	46.1	2.2	$(1.8 \pm 0.0)\,$k	26.7	1.6
Odd j veto	$(1.0 \pm 0.0)\,$k	47.1	1.9	$(1.8 \pm 0.0)\,$k	28.2	2.0
$j^1 : |\eta| < 2.5$	998.0 ± 10.4	48.9	3.4	$(1.8 \pm 0.0)\,$k	29.0	1.1
$j^2 : e > 100\,$GeV	610.3 ± 8.2	68.8	38.8	832.4 ± 1.9	66.8	53.2
$\Sigma h > 350\,$GeV	281.6 ± 5.5	85.6	53.9	650.1 ± 1.7	74.1	21.9
$\alpha_T > 0.55$	3.93 ± 0.66	99.8	98.6	2.77 ± 0.11	99.9	99.6
$\Delta R_{\mathrm{ECAL}} > 0.3 \wedge \Delta\phi^* > 0.5$	3.60 ± 0.63	99.8	8.3	2.39 ± 0.10	≥ 99.9	13.5
$\not{H}/\not{p} < 1.25$	3.28 ± 0.63	99.8	9.1	1.82 ± 0.09	≥ 99.9	23.9

Table C.2: Cut flow for the W and $t\bar{t}$ electroweak Monte Carlo samples scaled to $\int L\,\mathrm{d}t = 35.1\,\mathrm{pb}^{-1}$ for $N^j \geq 2$. Column a) is the number of events passing the cut, column b) is the percentage of events lost of those passing the intial $\Sigma h > 250\,$GeV cut (cumulative), and column c) is the percentage lost from the previous cut. Events are reconstructed with CMSSW_3_6_X.

Cut	$Z + nj$			$(Z \to \nu\bar{\nu}) + nj$		
	a)	b)	c)	a)	b)	c)
Selection	758.7 ± 8.6	-	-	491.6 ± 7.0	-	-
$\Sigma h > 250\,\mathrm{GeV}$	279.2 ± 5.2	0.0	63.2	285.3 ± 5.3	0.0	42.0
$N^\gamma = 0$	211.9 ± 4.6	24.1	24.1	285.3 ± 5.3	0.0	0.0
$N^e = 0$	193.5 ± 4.4	30.7	8.7	285.2 ± 5.3	0.0	0.0
$N^\mu = 0$	121.5 ± 3.5	56.5	34.4	275.8 ± 5.2	3.3	0.0
Bad μ in j	119.9 ± 3.4	57.1	1.4	274.0 ± 5.2	4.0	0.6
Odd j veto	116.4 ± 3.4	58.3	2.9	272.1 ± 5.2	4.6	0.7
$j^1 : |\eta| < 2.5$	109.9 ± 3.3	60.6	5.6	266.9 ± 5.2	6.5	1.9
$j^2 : e > 100\mathrm{GeV}$	65.0 ± 2.5	76.7	40.9	160.5 ± 4.0	43.8	39.9
$\Sigma h > 350\,\mathrm{GeV}$	27.7 ± 1.7	90.1	57.3	79.1 ± 2.8	72.3	50.7
$\alpha_T > 0.55$	0.00 ± 0.00	100.0	100.0	4.18 ± 0.64	98.5	94.7
$\Delta R_{\mathrm{ECAL}} > 0.3 \wedge \Delta\phi^* > 0.5$	0.00 ± 0.00	100.0	-	4.18 ± 0.64	98.5	0.0
$\not{k}/\not{p} < 1.25$	0.00 ± 0.00	100.0	-	4.08 ± 0.64	98.6	2.4

Table C.3: Cut flow for the Z electroweak Monte Carlo samples scaled to $\int L\,\mathrm{d}t = 35.1\,\mathrm{pb}^{-1}$ for $N^j \geq 2$. Column a) is the number of events passing the cut, column b) is the percentage of events lost of those passing the intial $\Sigma h > 250\,\mathrm{GeV}$ cut (cumulative), and column c) is the percentage lost from the previous cut.

Cut	LM0			LM1		
	a)	b)	c)	a)	b)	c)
Selection	$(1.0 \pm 0.0)\,\text{k}$	-	-	132.1 ± 0.3	-	-
$\Sigma h > 250\,\text{GeV}$	954.4 ± 2.5	0.0	9.0	128.2 ± 0.3	0.0	2.9
$N^\gamma = 0$	878.6 ± 2.4	7.9	7.9	118.9 ± 0.3	7.2	7.2
$N^e = 0$	825.2 ± 2.3	13.5	6.1	110.4 ± 0.3	13.8	7.2
$N^\mu = 0$	665.2 ± 2.1	30.3	19.4	86.2 ± 0.3	32.7	21.9
Bad μ in j	653.6 ± 2.1	31.5	1.7	85.3 ± 0.3	33.4	1.0
Odd j veto	642.8 ± 2.1	32.7	1.6	84.0 ± 0.3	34.5	1.6
$j^1 : |\eta| < 2.5$	638.8 ± 2.0	33.1	0.6	83.8 ± 0.3	34.6	0.2
$j^2 : e > 100\,\text{GeV}$	464.6 ± 1.7	51.3	27.3	71.6 ± 0.2	44.2	14.6
$\Sigma h > 350\,\text{GeV}$	420.3 ± 1.7	56.0	9.5	67.9 ± 0.2	47.0	5.1
$\alpha_T > 0.55$	55.7 ± 0.6	94.2	86.7	20.8 ± 0.1	83.8	69.3
$\Delta R_{\text{ECAL}} > 0.3 \wedge \Delta\phi^* > 0.5$	51.6 ± 0.6	94.6	7.3	19.9 ± 0.1	84.5	4.6
$\not{h}/\not{p} < 1.25$	47.1 ± 0.6	94.6	7.3	19.5 ± 0.1	84.8	1.8

Table C.4: Cut flow for the signal Monte Carlo samples scaled to $\int L\,\mathrm{d}t = 35.1\,\mathrm{pb}^{-1}$ for $N^j \geq 2$. Column $a)$ is the number of events passing the cut, column $b)$ is the percentage of events lost of those passing the intial $\Sigma h > 250\,\text{GeV}$ cut (cumulative), and column $c)$ is the percentage lost from the previous cut. The samples are reconstructed with `CMSSW_3_6_X`.

Appendix D

List of Acronyms

ATLAS A Toroidal LHC ApparatuS

CDM Cold Dark Matter

CERN European Organization for Nuclear Research

CKM Cabibbo-Kobayashi-Maskawa (matrix)

CL Confidence Level

CMS Compact Muon Solenoid experiment

CMSSM Constrained Minimally Supersymmetric Standard Model

CMSSW CMS SoftWare

CSC Cathode Strip Chamber (c.f. the CMS muon system)

DAQ Data AcQuisition (system)

DT Drift Tube chambers (c.f. the CMS muon system)

dof Degrees of freedom

EBHGHK Englert-Brout-Higgs-Guralnik-Hagen-Kibble mechanism, boson

ECAL Electromagnetic Calorimeter

EDM Event Data Model

FED Front End Driver

FPGA Field-Programmable Gate Array

FSR Final State Radiation

GMSB Gauge-Mediated Supersymmetry Breaking

GUT Grand Unified Theory

HCAL Hadron Calorimeter

HLT High-Level Trigger

HPD Hybrid Photo-Diode

IC Iterative Cone (jet-finding algorithm)

IP Interaction Point (at which two opposing beams of particles collide)

ISR Initial State Radiation

JEC Jet Energy Corrections

JPT Jet-Plus-Track (particle jet reconstruction algorithm)

LEP Large Electron-Positron collider

LHC Large Hadron Collider

LM Low Mass supersymmetry benchmark points

LO Leading Order (cross-section estimate)

LSP Lightest Supersymmetric Particle

MC Monte Carlo (simulation)

MSSM Minimally Supersymmetric Standard Model

MSUGRA Minimal Supergravity

NLO Next-to-Leading Order (cross-section estimate)

QCD Quantum Chromodynamics

QED Quantum Electrodynamics

QFT Quantum Field Theory

PBE Probability of Block Error

PDF Parton Density Function

PF Particle Flow (particle jet reconstruction algorithm)

RGE Renormalisation Group Equation

RPC Resistive Plate Chambers (c.f. the CMS muon system)

SM Standard Model of particle physics

SPS Super Proton Synchrotron

SSB Spontaneous Symmetry Breaking

SST Silicon Strip Tracker (c.f. the CMS experiment)

TOM Transverse Object Merging recombination scheme

VEV Vacuum Expectation Value

VPT Vacuum Phototriode (c.f. the CMS ECAL Endcap)

WMAP Wilson Microwave Anisotropy Probe

Bibliography

[1] The LHC Study Group, "The Large Hadron Collider: Conceptual Design," Tech. Rep. CERN-AC-95-05 LHC, CERN, Geneva, 1995.

[2] P. Higgs, "Broken Symmetries and the Masses of Gauge Bosons," *Phys. Rev. Lett.* **13** (1964), no. 16, 508–509.

[3] P. Higgs, "Spontaneous Symmetry Breakdown without Massless Bosons," *Phys. Rev.* **145** (1966), no. 4, 1156–1163.

[4] F. Englert and R. Brout, "Broken Symmetry and the Mass of Gauge Vector Mesons," *Phys. Rev. Lett.* **13** (1964), no. 9, 321–323.

[5] G. Guralnik, C. Hagen, and T. Kibble, "Global Conservation Laws and Massless Particles," *Phys. Rev. Lett.* **13** (1964), no. 20, 585–587.

[6] N. ArkaniHamed, S. Dimopoulos, and G. Dvalic, "The hierarchy problem and new dimensions at a millimeter," *Phys. Lett. B* **429** (1998), no. 3-4, 263–272.

[7] L. Randall and D. Tucker-Smith, "Dijet searches for supersymmetry at the large hadron collider," *Phys. Rev. Lett.* **101** (2008), no. 22, 221803–221807.

[8] S. Giddings and S. Thomas, "High energy colliders as black hole factories: The end of short distance physics," *Phys. Rev. D* **65** (2002), no. 5, 056010.

[9] S. Dimopoulos and G. Landsberg, "Black Holes at the Large Hadron Collider," *Phys. Rev. Lett.* **87** (2001), no. 16, 161602.

[10] H. P. Nilles, "Supersymmetry, supergravity and particle physics," *Phys. Rep.* **110** (1984), no. 1-2, 1–162.

[11] J. M. Cornwall, D. N. Levin, and G. Tiktopoulos, "Uniqueness of spontaneously broken gauge theories," *Phys. Rev. Lett.* **30** (1973), no. 25, 1268–1270.

[12] J. M. Cornwall, D. N. Levin, and G. Tiktopoulos, "Derivation of gauge invariance from high-energy unitarity bounds on the S matrix," *Phys. Rev. D* **10** (1974), no. 4, 1145–1167.

[13] C. H. Llewellyn Smith, "High energy behaviour and gauge symmetry," *Phys. Lett. B* **46** (1973), no. 2, 233–236.

[14] B. W. Lee, C. Quigg, and H. B. Thacker, "Weak interactions at very high energies: The role of the Higgs-boson mass," *Phys. Rev. D* **16** (1977), no. 5, 1519–1531.

[15] G. Bennett *et al.*, "Measurement of the Positive Muon Anomalous Magnetic Moment to 0.7ppm," *Phys. Rev. Lett.* **89** (2002), no. 10, 101804.

[16] L. L. Everett, G. L. Kane, S. Rigolin, and L. Wang, "Implications of Muon $g - 2$ for Supersymmetry and for Discovering Superpartners Directly," *Phys. Rev. Lett.* **86** (2001), no. 16, 3484–3487.

[17] S. P. Martin and J. D. Wells, "Superconservative interpretation of muon $g - 2$ results applied to supersymmetry," *Phys. Rev. D* **67** (2003), no. 1, 015002.

[18] The CMS Collaboration, "Search for supersymmetry in pp collisions at $7\,\mathrm{TeV}$ in events with jets and missing transverse energy," *Phys. Lett. B* **698** (2011), no. 3, 196–218.

[19] D. Nelson, *The Penguin Dictionary of Mathematics.* Penguin Books, second ed., 1998.

[20] M. E. Peskin and D. V. Schroeder, *An Introduction to Quantum Field Theory.* Westview Press, 1995.

[21] Fermilab, "Fifth CERN-Fermilab Hadron Collider Physics Summer School," in *August 16-27*, D. Glenzinski and A. Kronfeld, eds. Batavia, IL, 2010.

[22] D. J. Gross and F. Wilczek, "Ultraviolet Behavior of Non-Abelian Gauge Theories," *Phys. Rev. Lett.* **30** (1973), no. 26, 1343–1346.

[23] S. Coleman and D. J. Gross, "Price of Asymptotic Freedom," *Phys. Rev. Lett.* **31** (1973), no. 13, 851–854.

[24] S. L. Glashow, "Partial-symmetries of Weak Interactions," *Nucl. Phys.* **22** (1961), no. 4, 579–588.

[25] A. Salam and J. C. Ward, "Electromagnetic and Weak Interactions," *Phys. Lett.* **13** (1964), no. 2, 168–171.

[26] S. Weinberg, "A Model of Leptons," *Phys. Rev. Lett.* **19** (1967), no. 21, 1264–1266.

[27] C. Quigg, "The Electroweak Theory," in *Flavor Physics for the Millennium - Tasi 2000 - Proceedings of the Theoretical Advanced Study Institute in Elementary Particle Physics*, pp. 3–67. World Scientific Publishing Co. Pte. Ltd., Singapore, 2001.

[28] M. Goldhaber, L. Grodzins, and A. W. Sunyar, "Helicity of Neutrinos," *Phys. Rev.* **109** (1958), no. 3, 1015–1017.

[29] R. Davis, D. S. Harmer, and K. C. Hoffman, "Search for Neutrinos from the Sun," *Phys. Rev. Lett.* **20** (1968), no. 21, 1205–1209.

[30] The Super-Kamiokande Collaboration, "Evidence for Oscillation of Atmospheric Neutrinos," *Phys. Rev. Lett.* **81** (1998), no. 8, 1562–1567.

[31] E. Majorana, "Teoria simmetrica dell 'elettrone e del positrone (Symmetrical theory of the electron and positron)," *Nuovo Cimento* **14** (1937) 171–184.

[32] N. Cabibbo, "Unitary Symmetry and Leptonic Decays," *Phys. Rev. Lett.* **10** (1963), no. 12, 531–533.

[33] M. Kobayashi and T. Maskawa, "CP-Violation in the Renormalizable Theory of Weak Interaction," *Prog. Theor. Phys.* **49** (1973), no. 2, 652–657.

[34] S. Weinberg, "The $U(1)$ problem," *Phys. Rev. D* **11** (1975), no. 12, 3583–3593.

[35] G. 't Hooft, "Symmetry Breaking through Bell-Jackiw Anomalies," *Phys. Rev. Lett.* **37** (1976), no. 1, 8–11.

[36] G. 't Hooft, "Computation of the quantum effects due to a four-dimensional pseudoparticle," *Phys. Rev. D* **14** (1976), no. 12, 3432–3450.

[37] The LEP Electroweak Working Group, "Precision electroweak measurements on the Z resonance," *Phys. Rep.* **427** (2006), no. 5-6, 257–454.

[38] P. Sikivie, L. Susskind, M. B. Voloshin, and V. Zakharov, "Isospin breaking in technicolor models," *Nucl. Phys. B* **173** (1980), no. 2, 189–207.

[39] S. Coleman and J. Mandula, "All Possible Symmetries of the S Matrix," *Phys. Rev.* **159** (1967), no. 5, 1251–1256.

[40] R. Haag, J. T. Łopuszański, and M. Sohnius, "All possible generators of supersymmetries of the S-matrix," *Nucl. Phys. B* **88** (1975), no. 2, 257–274.

[41] P. van Nieuwenhuizen, "Supergravity," *Phys. Rep.* **68** (1981), no. 4, 189–398.

[42] S. Deser and B. Zumino, "Broken Supersymmetry and Supergravity," *Phys. Rev. Lett.* **38** (1977), no. 25, 1433–1436.

[43] E. Cremmer *et al.*, "Super-higgs effect in supergravity with general scalar interactions," *Phys. Lett. B* **79** (1978), no. 3, 231–234.

[44] P. Binétruy, *Supersymmetry: Theory, Experiment and Cosmology.* Oxford University Press, Oxford, 1st ed., 2006.

[45] S. Dimopoulos, S. Raby, and F. Wilczek, "Supersymmetry and the scale of unification," *Phys. Rev. D* **24** (1981), no. 6, 1681–1683.

[46] H. Georgi, H. Quinn, and S. Weinberg, "Hierarchy of Interactions in Unified Gauge Theories," *Phys. Rev. Lett.* **33** (1974), no. 7, 451–454.

[47] S. Dimopoulos and H. Georgi, "Softly broken supersymmetry and SU(5)," *Nucl. Phys. B* **193** (1981), no. 1, 150–162.

[48] J. Dunkley *et al.*, "Five-year Wilkinson Microwave Anisotropy Probe Observations: Likelihoods and Parameters from the WMAP Data," *Astrophys. J. Supp.* **180** (2009), no. 2, 306–329.

[49] E. Komatsu *et al.*, "Five-year Wilkinson Microwave Anisotropy Probe Observations: Cosmological Interpretation," *Astrophys. J. Supp.* **180** (2009), no. 2, 330–376.

[50] K. Nakamura *et al.*, "Review of Particle Physics," *JPG* **37** (2010), no. 7A, 075021.

[51] S. P. Martin, "A Supersymmetry Primer," *e-print* (6th ed. accessed September, 2011) 1–128, `hep-ph/9709356`.

[52] P. Fayet, "Spontaneously broken supersymmetric theories of weak, electromagnetic and strong interactions," *Phys. Lett. B* **69** (1977), no. 4, 489–494.

[53] G. R. Farrar and P. Fayet, "Phenomenology of the production, decay, and detection of new hadronic states associated with supersymmetry," *Phys. Lett. B* **76** (1978), no. 5, 575–579.

[54] M. Dine and A. E. Nelson, "Dynamical supersymmetry breaking at low energies," *Phys. Rev. D* **48** (1993), no. 3, 1277–1287.

[55] M. Dine, A. E. Nelson, and Y. Shirman, "Low energy dynamical supersymmetry breaking simplified," *Phys. Rev. D* **51** (1995), no. 3, 1362–1370.

[56] M. Dine, A. E. Nelson, Y. Nir, and Y. Shirman, "New tools for low energy dynamical supersymmetry breaking," *Phys. Rev. D* **53** (1996), no. 5, 2658–2669.

[57] G. F. Giudice and R. Rattazzi, "Theories with gauge-mediated supersymmetry breaking," *Phys. Rep.* **322** (1999), no. 6, 419–499.

[58] L. Girardello and M. T. Grisaru, "Soft breaking of supersymmetry," *Nucl. Phys. B* **194** (1982), no. 1, 65–76.

[59] L. E. Ibáñez and G. G. Ross, "$SU(2)_L \times U(1)$ symmetry breaking as a radiative effect of supersymmetry breaking in GUTs," *Phys. Lett. B* **110** (1982), no. 3-4, 215–220.

[60] J. Derendinger and C. A. Savoy, "Quantum effects and $SU(2) \times U(1)$ breaking in supergravity gauge theories," *Nucl. Phys. B* **237** (1984), no. 2, 307–328.

[61] The Snowmass Collaboration, "The Snowmass Points and Slopes: benchmarks for SUSY searches," *EPJC* **25** (2002), no. 1, 113–123.

[62] The CMS Collaboration, "CMS Physics Technical Design Report, Volume II: Physics Performance," *JPG* **34** (2007), no. 6, 995–1579.

[63] B. Allanach, "SOFTSUSY: A program for calculating supersymmetric spectra," *Comp. Phys. Comm.* **143** (2002), no. 3, 305–331.

[64] The CMS Collaboration, "Search for supersymmetry in events with b jets and missing transverse momentum at the LHC," *JHEP* **7** (2011), no. 7, 113.

[65] A. R. Baden, "Jets and Kinematics in Hadronic Collisions," *IJMPA* **13** (1997), no. 11, 1817–1845.

[66] G. P. Salam, "Towards jetography," *EPJC* **67** (2010), no. 3-4, 637–686.

[67] A. J. Barr, B. M. Gripaios, and C. G. Lester, "Weighing Wimps with Kinks at Colliders: Invisible Particle Mass Measurements from Endpoints," *JHEP* **02** (2007) 014.

[68] G. Arnison, "Experimental observation of events with large missing transverse energy accompanied by a jet or a photon (S) in $p\bar{p}$ collisions at $\sqrt{s} = 540\,\text{GeV}$," *Phys. Lett. B* **139** (1984), no. 1-2, 115–125.

[69] V. Barger, A. D. Martin, and R. J. N. Phillips, "Perpendicular $e\nu$ mass from W decay," *Z. Phys. C* **21** (1983), no. 1-2, 99–101.

[70] The GEANT 4 Collaboration, "G4–a simulation toolkit," *Nucl. Instrum. Meth. A* **506** (2003), no. 3, 250–303.

[71] The CMS Collaboration, "The CMS experiment at the CERN LHC," *JINST* **3** (2008) S08004.

[72] H. Flächer, M. Stoye, T. Rommerskirchen, *et al.*, "SUSY search with dijet events," Tech. Rep. CMS AN-2008/071, CERN, 2008.

[73] The CMS Collaboration, "SUSY search with dijet events," Tech. Rep. CMS PAS SUS-08-005, CERN, 2008.

[74] T. Whyntie *et al.*, "Extending the early SUSY search with all-hadronic dijet events to n-jet topologies," Tech. Rep. CMS AN-2008/114, CERN, 2008.

[75] B. Allanach, "Impact of CMS Multi-jets and Missing Energy Search on CMSSM Fits," *Phys. Rev. D* **83** (2011), no. 9, 095019–095028.

[76] J. Pumplin *et al.*, "New Generation of Parton Distributions with Uncertainties from Global QCD Analysis," *JHEP* **2002** (2002), no. 7, 012.

[77] T. Sjöstrand, S. Mrenna, and P. Skands, "PYTHIA 6.4 physics and manual," *Journal of High Energy Physics* **2006** (2006), no. 5, 026–026.

[78] R. Corke and T. Sjöstrand, "Interleaved parton showers and tuning prospects," *JHEP* **2011** (2011), no. 3, 1–52.

[79] A. Buckley *et al.*, "General-purpose event generators for LHC physics," *Phys. Rep.* **504** (2011), no. 5, 145–233.

[80] W. Beenaker, R. Höpker, M. Spria, and P. Zerwas, "Squark and gluino production at hadron colliders," *Nucl. Phys. B* **492** (1997), no. 1-2, 51–103.

[81] J. Alwall *et al.*, "MadGraph/MadEvent v4: the new web generation," *JHEP* **2007** (2007), no. 9, 028–028.

[82] J. Alwall, S. de Visscher, and F. Maltoni, "QCD radiation in the production of heavy colored particles at the LHC," *JHEP* **2009** (2009), no. 2, 017–017.

[83] The JADE Collaboration, "Experimental studies on multijet production in e^+e^- annihilation at PETRA energies," *Z. Phys. C* **33** (1986), no. 1, 23–31.

[84] The JADE Collaboration, "Experimental investigation of the energy dependence of the strong coupling strength," *Phys. Lett. B* **213** (1988), no. 2, 235–241.

[85] S. Catani, Y. L. Dokshitzer, M. Olsson, G. Turnock, and B. R. Webber, "New clustering algorithm for multijet cross sections in e^+e annihilation," *Phys. Lett. B* **269** (1991), no. 3-4, 432–438.

[86] S. Catani, Y. L. Dokshitzer, M. H. Seymour, and B. R. Webber, "Longitudinally-invariant $K_\perp$-clustering algorithms for hadron-hadron collisions," *Nucl. Phys. B* **406** (1993), no. 1-2, 187–224.

[87] S. D. Ellis and D. E. Soper, "Successive combination jet algorithm for hadron collisions," *Phys. Rev. D* **48** (1993), no. 7, 3160–3166.

[88] Y. L. Dokshitzer, G. D. Leder, S. Moretti, and B. R. Webber, "Better jet clustering algorithms," *JHEP* **9708** (1997), no. 8, 001.

[89] M. Wobisch, *Measurement and QCD analysis of jet cross sections in deep-inelastic positron proton collisions at $\sqrt{s} = 300\,GeV$.* PhD thesis, Aachen, Tech. Hochsch., 2000.

[90] M. Cacciari, G. P. Salam, and G. Soyez, "The anti-k_t jet clustering algorithm," *JHEP* **0804** (2008) 063.

[91] D. J. C. MacKay, *Information Theory, Inference, and Learning Algorithms.* Cambridge University Press, 7.2 ed., 2003.

[92] The ATLAS Collaboration, "The ATLAS Experiment at the CERN LHC," *JINST* **3** (2008), no. 08, S08003.

[93] The CMS Collaboration, "CMS Physics Technical Design Report Volume I: Detector Performance and Software," Tech. Rep. CERN/LHCC-2006-001, CERN, 2006.

[94] The CMS Collaboration, "The TriDAS Project Technical Design Report, Vol. I: The Trigger Systems," Tech. Rep. CERN/LHCC-2000-38, CERN, 2000.

[95] The CMS Collaboration, "The TriDAS Project Technical Design Report, Vol. II: Data Acquisition and High-Level Trigger," Tech. Rep. CERN/LHCC-2002-326, CERN, 2000.

[96] The CMS Collaboration, "Computing Technical Proposal," Tech. Rep. CERN/LHCC-1996-45, CERN, 1996.

[97] The CMS Collaboration, "Jet performance in pp collisions at $\sqrt{s} = 7\,\text{TeV}$," Tech. Rep. CMS PAS JME-10-003, CERN, 2010.

[98] The CMS Collaboration, "Jet Plus Tracks Algorithm for Calorimeter Jet Energy Corrections in CMS," Tech. Rep. CMS PAS JME-09-002, CERN, 2009.

[99] The CMS Collaboration, "Particle-Flow Event Reconstruction in CMS and Performance for Jets, Taus, and $E_T^{\text{miss.}}$," Tech. Rep. CMS PAS PFT-09-001, CERN, 2009.

[100] The CMS Collaboration, "Commissioning of the Particle-Flow Reconstruction in Minimum-Bias and Jet Events from pp Collisions at $7\,\text{TeV}$," Tech. Rep. CMS PAS PFT-10-002, CERN, 2010.

[101] The CMS Collaboration, "Calorimeter Jet Quality Criteria for the First CMS Collision Data," Tech. Rep. CMS PAS JME-09-008, CERN, 2010.

[102] The CMS Collaboration, "Determination of the Jet Energy Scale in CMS with pp Collisions at $\sqrt{s} = 7\,\text{TeV}$," Tech. Rep. CMS PAS JME-10-010, CERN, 2010.

[103] The CMS Collaboration, "Determination of jet energy calibration and transverse momentum resolution in CMS," *JINST* **6** (2011), no. 11, 11002.

[104] The UA2 Collaboration, "Measurement of production and properties of jets at the CERN $p\bar{p}$ collider," *Z. Phys. C* **20** (1983), no. 2, 117–134.

[105] The D0 Collaboration, "Determination of the absolute jet energy scale in the DØ calorimeters," *Nucl. Instrum. Meth. A* **424** (1999), no. 2-3, 352–394.

[106] The CDF Collaboration, "Determination of the jet energy scale at the Collider Detector at Fermilab," *Nucl. Instrum. Meth. A* **566** (2006), no. 2, 375–412.

[107] The CMS Collaboration, "Determination of the Relative Jet Energy Scale at CMS from Dijet Balance," Tech. Rep. CMS PAS JME-08-003, CERN, 2009.

[108] The D0 Collaboration, "Determination of the absolute jet energy scale in the DØ calorimeters," *Nucl. Intrum. Meth. A* **424** (1999), no. 2-3, 352–394.

[109] The CMS Collaboration, "Jet energy calibration with photon + jet events," Tech. Rep. CMS PAS JME-09-004, CERN, 2009.

[110] The CMS Collaboration, "Jet Resolution Determination at $\sqrt{s} = 7\,\text{TeV}$," Tech. Rep. CMS PAS JME-10-014, CERN, 2010.

[111] The CMS Collaboration, "A Search for Supersymmetry in Proton-Proton Collisions at $\sqrt{s} = 7\,\text{TeV}$ using Events with Two Photons and Large Missing Transverse Energy," Tech. Rep. CMS PAS SUS-10-002, CERN, 2010.

[112] The CMS Collaboration, "Search for Supersymmetry in *pp* Collisions at $\sqrt{s} = 7\,\text{TeV}$ in Events with Two Photons and Missing Transverse Energy," *Phys. Rev. Lett.* **106** (2011), no. 21, 211802.

[113] The CMS Collaboration, "Photon reconstruction and identification at $\sqrt{s} = 7\,\text{TeV}$," Tech. Rep. CMS PAS EGM-10-005, CERN, 2010.

[114] The CMS Collaboration, "Study of *W* and *Z* Boson Production at 7 TeV," Tech. Rep. CMS PAS EWK-10-005, CERN, 2010.

[115] The CMS Collaboration, "Measurement of the inclusive *W* and *Z* production cross sections in *pp* collisions at $\sqrt{s} = 7\,\text{TeV}$ with the CMS experiment," *JHEP* (2011), no. 10, 132.

[116] The CMS Collaboration, "Electron reconstruction and identification at $\sqrt{s} = 7\,\text{TeV}$," Tech. Rep. CMS PAS EGM-10-004, CERN, 2010.

[117] The CMS Collaboration, "Performance of CMS muon reconstruction in cosmic-ray events," *JINST* **5** (2010), no. 03, T03022.

[118] The CMS Collaboration, "Performance of muon identification in pp collisions at $\sqrt{s} = 7\,\text{TeV}$," Tech. Rep. CMS PAS MUO-10-002, CERN, 2010.

[119] The CMS Collaboration, "Search for a missing energy signature from new physics in di-jet and multi-jet events," Tech. Rep. CMS PAS SUS-10-003, CERN, 2010.

[120] The CMS SUSY RA1 analysis group, "Search for a missing energy signature from new physics in di-jet and multi-jet events," Tech. Rep. CMS AN-2010/242, CERN, 2010.

[121] R. Brun *et al.*, "Root a c++ framework for petabyte data storage, statistical analysis and visualization," *Comput. Phys. Commun.* **180** (2009), no. 12, 2499–2512.

[122] The CMS Collaboration, "Tracking and Primary Vertex Results in First 7 TeV Collisions," Tech. Rep. CMS PAS TRK-10-005, CERN, 2010.

[123] The CMS Collaboration, "HCAL performance from first collisions data," Tech. Rep. CMS DPS-2010/025, CERN, 2010.

[124] R. Field, "Early LHC Underlying Event Data - Findings and Surprises," in *Proceedings of the Hadron Collider Physics Symposium 2010*, no. C10-08-23.3. Aug., 2010. `hep-ph/1010.3558`.

[125] The CMS Collaboration, "CMS MET performance in events containing electroweak bosons from pp collisions at $\sqrt{s} = 7\,\text{TeV}$," tech. rep., CERN, 2010.

[126] The CMS Collaboration, "Performance of Methods for Data-Driven Background Estimation in SUSY Searches," Tech. Rep. CMS-PAS-SUS-10-001, CERN, 2010.

[127] The CMS Collaboration, "First measurement of the cross section for top-quark pair production in pp collisions at $\sqrt{s} = 7\,\text{TeV}$," *Phys. Lett. B* **695** (2011), no. 5, 424–443.

[128] The CMS Collaboration, "Data-driven estimate of the invisible Z background to the SUSY MET plus jets search," Tech. Rep. CMS PAS-SUS-08-002, CERN, 2008.

[129] G. J. Feldman and R. D. Cousins, "Unified approach to the classical statistical analysis of small signals," *Phys. Rev. D* **57** (1998), no. 7, 3873–3889.

[130] T. A. Severini, *Likelihood methods in statistics.* Oxford University Press, 2000.

[131] T. Aaltonen *et al.*, "Inclusive Search for Squark and Gluino Production in $p\bar{p}$ Collisions at $\sqrt{s} = 1.96\,\text{TeV}$," *Phys. Rev. Lett.* **102** (2009), no. 12, 121801.

[132] V. M. Abazov *et al.*, "Search for squarks and gluinos in events with jets and missing transverse energy using $2.1\,\text{fb}^1$ of $p\bar{p}$ collision data at $\sqrt{s} = 1.96\,\text{TeV}$," *Phys. Lett. B* **660** (2008), no. 5, 449–457.

[133] The LEP-SUSY Working Group, "Interpretation of the results in Minimal SUGRA," Tech. Rep. LEPSUSYWG/02-06.2, CERN, 2002.

[134] V. M. Abazov *et al.*, "Search for associated production of charginos and neutralinos in the trilepton final state using $2.3\,\text{fb}^1$ of data," *Phys. Lett. B* **680** (2009), no. 1, 34–43.